Nanosystems out of Equilibrium: Persistent Currents and Quantum Dots

Im Fachbereich Physik der
Freien Universität Berlin
eingereichte

Dissertation

von

Friedrich Carl Gethmann

Berlin, im Mai 2012

Contents

Chapter 1

Introduction

The observation of quantum mechanical effects in controllable devices and under manipulable experimental conditions has been one of the most appealing fields of activity in physics over the last century. The progress in experimental techniques made it possible to scale down the parameters of macroscopic systems to mesoscopic scales where systems start to reveal quantum mechanical properties, while keeping control over the properties of the systems under consideration. Early examples of the observation of such quantum mechanical effects are superconductivity and the quantum Hall effect - two of the most important subareas in modern-day physics. The field of mesoscopic physics in general deals with objects on those mesoscopic scales, which are defined as the scales where a system starts to exhibit the first quantum mechanical effects. The boundaries between a macroscopic and a mesoscopic object are hereby not sharp, but rather depend on the specific system under consideration. A lower lengthscale can be definded as the size of an individual atom, where the system exhibits purely quantum mechanical properties.

Possible mechanisms leading to manifestations of quantum mechanics in mesoscopic devices can be categorized into effects of interference, charging and quantum confinement. Effects arising from interference of the electronic wave function can lead to reproducible fluctuations in physical quantities, e.g. universal fluctuations of the conductance (cf. [1, 2]). These interferences are possible if the electrons do not lose their phase coherence due to inelastic scattering events. The thus defined *dephasing length*, which will crucially depend on the frequency of occurrence of inelastic scattering events and thus also on the temperature of the system, serves as a definition of the lengthscale below which which a system can be called mesoscopic. A common example for the manifestation of quantum mechanics due to charging effects are quantum dots, i.e. systems which are so small that charging with one additional charge quantum becomes visible. Finally, quantum confinement describes the discretization of the energy levels when the lengthscales of a system become of the order of the wavelength of the electrons' wave function.

While most of the systems considered above are well understood in thermal equilibrium, in general out-of-equilibrium situations new effects can arise. Driving a mesoscopic system out of equilibrium by means of an additional perturbation is thus a suitable method to achieve access to new mesoscopic phenomena. While basic physical effects as the linear conductance arise from first order perturbation theory, in this thesis we will treat systems perturbed in a way that one has to go explicitly beyond the first order to describe their

essential properties.

In this thesis we study two distinct mesoscopic systems which are driven out of equilibrium by different mechanisms. We begin with the examination of mesoscopic normal (i.e. non-superconducting) metal rings. These rings are known to exhibit a so-called persistent current, i.e. a perpetual current flowing around the ring even without applied voltage. This is possible when time reversal symmetry is broken by a magnetic flux piercing the ring [3, 4, 5]. Remarkably, this persistent current exists even in the absence of an applied voltage and is thus an equilibrium property of the system. We analyze a generalized situation where the system is driven out of equilibrium artificially by applying an additional microwave field perpendicular to the ring. This investigation is motivated by several previous findings of the influence of microwave fields on mesoscopic systems such as a photovoltaic effect in mesoscopic junctions [6] or the microwave-induced magneto-oscillations in the photoconductivity of a two-dimensional electron gas [7, 8].

While persistent currents are an effect arising from the coherence of the electronic wave function in the rings, in the second system under consideration quantum mechanical properties are caused by charging and quantum confinement effects. We analyze consequences of coupling quantum dots, i.e. nanometer-sized confinements, to a vibrational mode. To leading order in this vibrational perturbation one commonly assumes that the vibrational energy is harmonic and the mode is coupled linearly to the electronic degrees of freedom. While the considered system is already widely studied in the literature, we specialize on a particularly interesting regime where the coupling between the vibrational mode and the electronic degrees of freedom is so strong that the system becomes unstable within these common assumptions. More precisely the coupling between electronic degrees of freedom and a vibrational mode causes a renormalization of the charging energy, which is the energy needed to add another electron to the quantum dot. Recent investigations on vibrational modes of carbon nanotubes [9] suggest that it might be possible to reach regimes where the coupling is so strong that the charging energy becomes not only negative, but even overcomes the finite level spacing which regularized the instability in previous considerations [10]. We show that in this case the instability can be regularized by the anharmonic contribution to the vibron energy. The resulting effective charging energy as a function of the electron number has a double-well structure causing a variety of novel features in the Coulomb-blockade properties of the system.

Part I

Persistent current under microwave irradiation

The perpetual current flowing in small non superconducting rings without applied voltage under breaking of time reversal symmetry has been of great interest in theoretical and experimental physics over the last three decades. Since the effect crucially depends on the coherence of the electron wave function over the whole ring it is a manifestation of a quantum mechanical effect in a mesoscopic system.

The basic effect which can cause a persistent current in a resistive metal ring is physically closely related to the perpetual motion of an electron around the nucleus. Thus its existence was already stated in 1938 by Hund [3] and calculated for the case of a clean system by Bloch [11] and Kulik [12]. However, the observation of the effect of a perpetual current flowing in a realistic normal metal ring containing elastic disorder stayed somewhat counterintuitive until Büttiker *et. al* [4] proposed in 1983 the existence of the effect even in those realistic mesoscopic systems.

Experimentally the observation of persistent currents has been a huge challenge for several reasons. The currents are extremely small[1] and applying e.g. an ammeter would cause the electrons to lose phase coherence and destroy the effect. Therefore one has to measure the small change in the magnetic moment produced by the currents instead. In addition, the rings have to be mesoscopically small, which means that the time it takes an electron to move around the ring - the so called diffusion time τ_D - has to be smaller than the inelastic scattering time τ_{in}. And third, the effect is rapidly destroyed if the temperature goes up, which means that experiments have to be performed at one Kelvin and below. For these reasons, in the first experiments in the field [15, 16, 17] one was not able to see persistent currents of the order theory predicted. However, in two recent experiments

Figure 1.1: Sketch of an electron circulating in a mesoscopic ring threaded by a magnetic flux scattered from static impurities. (Figure taken from [13])

Bluhm *et al.* [18] and Bleszynski-Jayich *et al.* [14], using different experimental approaches, where able to measure persistent current in great precision and in good accordance to the theoretical prediction, which revitalized the field.

In the first part of the thesis we want to study the influence of an additional microwave electric field on the persistent current in a normal metal ring pierced by a magnetic flux. In the Section 2, we give an introduction to the problem by deriving basic properties. We begin with a clean, one dimensional sample and introducing piecewise the effects of higher dimensionality, disorder, finite temperature and electron electron interactions. After this, we describe the recent experiments in the field in the Section 3. Section 4 is dedicated to the calculation of the influence of a microwave field on the persistent current. Since the persistent current itself is an equilibrium property and the microwave field will drive the

---

[1]A ring with a micrometer-diameter supports persistent currents of $i \sim 1\,nA$ at temperatures $T \lesssim 1\,K$ [14].

system out of equilibrium, we have to introduce the so-called Keldysh formalism [19, 20] to attack the problem. We summarize the results and conclude in Section 5.

Chapter 2

Introduction to the field

We start the presentation of our work on persistent currents by introducing basic concepts and considerations in the unperturbed system, i.e. the system without applied additional microwave field. The approach we choose is logical in the sense that we start by presenting basic calculations leading to persistent currents in a clean one dimensional system (Section 2.1) and introduce, in a piecewise manner, more realistic properties, but by chance also approximately reproduces the historical progress of the theoretical treatment of the field.

The section develops as follows. We start - as mentioned - with the most abstract case of a one dimensional clean system in the absence of interactions, as it was already examined by Hund [3] in 1938. The enhancement of the calculation to two or more dimensions in Section 2.2 is straightforward, but gives already valuable insights in the characteristics of physical properties such as the average current introduced in Section 2.3. However the system is assumed to be clean and at zero temperature at this point. This assumption is dropped in Section 2.4, first by looking at the effect of finite temperatures (Section 2.4.1) and then by allowing for an elastic disorder potential in the rings (Section 2.4.2). An even more realistic picture is provided by assuming diffusive motion of the electrons in the ring in Section 2.4.3. Finally we discuss the effect of electron-electron interactions on the physical quantities in Section 2.5.

2.1   Clean one dimensional system

We start by calculating the persistent current in a clean ring of circumference L. As a first step we consider a purely one dimensional system. We assume, that the ring is threaded by a magnetic flux $\phi = \varphi\, h/e \equiv \varphi\, \phi_0$, where $\phi_0 = h/e$ is the flux quantum, as it can be seen in Figure 2.1. This flux can be represented by a vector potential $\boldsymbol{A} = \phi/L\, \hat{e}_x$, where $\hat{e}_x$ denotes the unit vector in the longitudinal direction. We can assume the ring to be a current-carrying loop of area $S = \pi R^2$, R the radius of the ring, and define the persistent current of the ring as as its magnetization per unit area [2, 5, 11, 21]. Assuming a constant chemical potential μ we get

$$I(\phi) = -\frac{1}{S}\left(\frac{\partial \Phi}{\partial B}\right)_{\mu,T} = -\left(\frac{\partial \Phi}{\partial \phi}\right)_{\mu,T}, \tag{2.1}$$
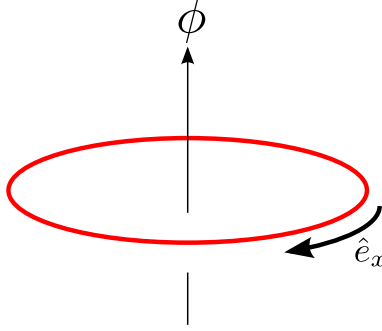
Figure 2.1: One dimensional ring threaded by a magnetic flux ϕ

where $\phi = S\,B$ is the flux through the ring and $\Phi(T, \mu, B) = -k_B T \ln \mathcal{Z}_g$ the thermodynamic grand potential

$$\Phi(T, B) = -2k_B T \sum_n \ln \left(1 + e^{\beta(\epsilon_F - \epsilon_n)} \right) . \tag{2.2}$$

Introducing the density of states $\nu(\epsilon, B) = \sum_n \delta(\epsilon - \epsilon_n(B))$ we obtain after integrating by parts twice

$$\Phi(T, B) = -2k_B T \int_0^\infty d\epsilon\, \nu(\epsilon, B) \ln \left(1 + e^{\beta(\epsilon_F - \epsilon)} \right)$$
$$= 2 \int_0^\infty d\epsilon\, \underbrace{\left(\int^\epsilon d\epsilon' N(\epsilon', B) \right)}_{\mathcal{N}(\epsilon, B)} \frac{\partial f}{\partial \epsilon} , \tag{2.3}$$

where we introduced the counting function $N(\epsilon, B)$ (which is nothing but the integrated density of states) and the Fermi function $f(\epsilon) = \left(1 + e^{\beta(\epsilon - \epsilon_F)} \right)^{-1}$. Inserting this in the expression for the persistent current (2.1) we obtain

$$I(\phi) = 2 \frac{\partial}{\partial \phi} \int_0^\infty d\epsilon\, \mathcal{N}(\epsilon, \phi) \left(-\frac{\partial f}{\partial \epsilon} \right) , \tag{2.4}$$

including a factor of two accounting for spin degeneracy. At zero temperature, the negative derivative of the Fermi function is a delta function and we get

$$I_{T=0} = 2 \frac{\partial \mathcal{N}(\epsilon_F, \phi)}{\partial \phi} . \tag{2.5}$$

Thus we are left with calculating the eigenenergies of the system. The time-independent Schrödinger equation for the ring takes the form

$$-\frac{1}{2m} \left(\partial_x + 2\pi i \phi / L \right)^2 \psi_n(x) = E_n\, \psi_n(x) , \tag{2.6}$$

where $\psi_n(x)$ fulfills the boundary condition $\psi_n(x) = \psi_n(x + L)$. Further we assume that the curvature of the ring does not affect the spectrum. A gauge transformation [21]

$$\psi_n'(x) = \psi_n(x) e^{-ie \int_0^x A dl} = \psi_n(x) e^{-2\pi i \varphi x / L} \tag{2.7}$$

transforms the Schrödinger equation into

$$-\frac{1}{2m}\frac{\partial^2}{\partial_x^2}\psi'_n(x) = \epsilon_n \psi'_n(x) \tag{2.8}$$

and pushes the flux dependence into the boundary conditions

$$\psi'_n(x+L) = \psi'_n(x)\, e^{-2\pi i \phi}\,. \tag{2.9}$$

Thus the eigenenergies turn out to be

$$\epsilon_n = \frac{1}{2m}\left(\frac{2\pi}{L}\right)^2 (n-\phi)^2\,, \tag{2.10}$$

and the density of states thus looks like[1]

$$
\begin{aligned}
\nu(\epsilon,\phi) &= \sum_n \delta(\epsilon - \epsilon_n) = \sum_n \delta\left[\epsilon - \frac{1}{2m}\left(\frac{2\pi}{L}\right)^2 (n-\phi)^2\right] \\
&= \sum_{p=-\infty}^{\infty} e^{2\pi i p \phi}\int dn\, e^{2\pi i p n}\delta\left[\epsilon - \frac{1}{2m}\left(\frac{2\pi}{L}\right)^2 n^2\right] \\
&\overset{k=\frac{2\pi n}{L}}{=} \sum_{p=-\infty}^{\infty}\cos\left(2\pi p\phi\right)\int dk\, e^{iLpk}\,\delta(\epsilon - \epsilon(k))\,,
\end{aligned}
\tag{2.11}
$$

where $\epsilon(k) = \frac{k^2}{2m}$. The counting function can be expressed as

$$N(\epsilon,\phi) = \frac{L\sqrt{2m\epsilon}}{\pi} + \frac{2}{\pi}\sum_{p=1}^{\infty}\frac{\sin\left(pL\sqrt{2m\epsilon}\right)}{p}\cos\left(2\pi p\phi\right)\,. \tag{2.12}$$

We obtain the persistent current at zero temperature by inserting this into Eq. (2.5)

$$
\begin{aligned}
I(\phi) &= -2\frac{\partial}{\partial\phi}\int_0^{\epsilon_F} d\epsilon'\, N(\epsilon',\phi) \\
&= \frac{2}{\pi}\frac{ev_F}{L}\sum_{p=1}^{\infty}\left[\frac{\cos\left(pk_F L\right)}{p} - \frac{\sin\left(pk_F L\right)}{p^2 k_F L}\right]\sin\left(2\pi p\phi\right)\,,
\end{aligned}
\tag{2.13}
$$

---

[1]Here we use for the first time an equality called *Poisson Summation*

$$\sum_n f(n+\phi) = \sum_k e^{2\pi i k \phi}\int dn\, f(n)\, e^{2\pi i k n}\,, \text{or, if f(n) = f(-n)}$$

$$= \int dn\, f(n) + 2\sum_{k=1}^{\infty}\cos\left(2\pi k\phi\right)\int dn\, f(n)\, e^{2\pi i k n}$$

which can be easily proven by Fourier transformation.
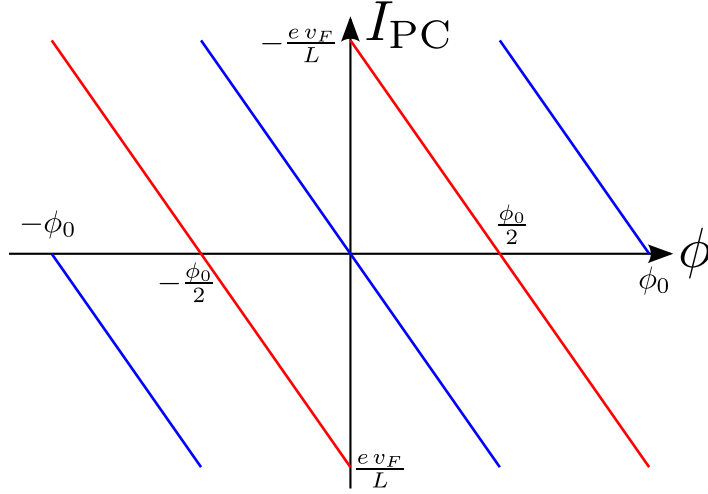
Figure 2.2: Persistent current in a clean ring at $T = 0$ for an even (red) and odd (blue) number of electrons.

where k_F is the Fermi momentum and $v_F = k_F/m$ the Fermi velocity. In a realistic sample the number of electrons will be large, which means that $k_F L \gg 1$, leading to

$$I(\phi) = \frac{2}{\pi} \frac{ev_F}{L} \sum_{p=1}^{\infty} \frac{\cos(pk_F L)}{p} \sin(2\pi p \phi) . \qquad (2.14)$$

If we assume, that not the chemical potential, but the number of electrons in the ring is fixed, which means that the Fermi momentum becomes $k_F = N\pi/L$, we obtain

$$I(\phi) = \frac{2}{\pi} \frac{ev_F}{L} \sum_{p=1}^{\infty} \frac{(-1)^{pN}}{p} \sin(2\pi p \phi) . \qquad (2.15)$$

This function can be seen in Figure 2.2. We see, that the sign of the persistent current at fixed flux depends on the parity of the number of electrons, and that the persistent current is periodic in the flux with period ϕ_0.

2.2 Two or more dimensions

The next step is to turn to a somehow more realistic description and allow for electronic dispersion in the transverse direction, i.e. we look at an effectively two dimensional cylinder. The eigenenergies turn into

$$\epsilon_n = \frac{1}{2m} \left(\frac{2\pi}{L} \right)^2 (n - \phi)^2 + \frac{k_z^2}{2m} , \qquad (2.16)$$

where $k_z = m\pi/L_z$, m an integer. Assuming that the electrons contributing to the current are at the Fermi surface, i.e. $k_F^2 = k^2 + q^2$, where k and q are the longitudinal and transverse components, the quantization of the transverse components depends on the

typical lengthscale of the cross-sectional area (here: L_z), and the number of transverse channels [22] is

$$M = \frac{2k_F}{2\pi/L_z} = \frac{k_F L_z}{\pi} \,. \tag{2.17}$$

Since the eigenenergies are the sum of the longitudinal and the transverse energies, the total current which we obtain following the steps leading to Eq. (2.14) is the sum over the contributions from the transverse channels contributing to the current. With $k_x^2 = k_F^2 - k_z^2$ we get

$$I(\phi) = \frac{2}{\pi} \frac{ev_F}{L} \sum_{m=1}^{M} \sum_{p=1}^{\infty} \frac{k_x}{k_F} \frac{\cos(pk_x L)}{p} \sin(2\pi p\phi) \,. \tag{2.18}$$

2.3 Average current

As we will illustrate later (chapter 3), in many experiments the effect is measured for a large number of rings instead of a single ring. Thus it is important to calculate characteristics of the persistent current averaged over a large number of samples. We can define the average current by dividing the total magnetization of an ensemble of many rings by the total number of rings. Since we do not take disorder effects into account yet, this means that we have to average Eq. (2.15) over the number of electrons N.

Splitting the sum in Eq. (2.15) into contributions from even and odd p, we see, that the odd part vanishes, since it changes sign depending on N, while the even part is N-independent. So we are left with

$$I(\phi) = \frac{1}{\pi} \frac{ev_F}{L} \sum_{p=1}^{\infty} \frac{1}{p} \sin(4\pi p\phi) \,. \tag{2.19}$$

Thus the average current seems to be $\phi/2$-periodic. However, if we turn towards the more realistic description of a two-dimensional sample, Eq. (2.18), we can see that the average current vanishes as expected, since for $L_z \ll L$ the cosine varies rapidly as a function of k_z.

2.4 Temperature and disorder effects

Before allowing for disorder and turning towards describing the diffusive motion of electrons in the ring [4], we calculate the effect of finite temperatures and elastic disorder on the undisturbed model.

2.4.1 Finite temperature

Finite temperature is included by dropping the assumption of a step like Fermi distribution and use the expression for the current in Eq. (2.4). Linearizing the dispersion relation around the Fermi energy,

$$\epsilon = \epsilon_F + v_F(k - k_F) \,, \tag{2.20}$$

we get, including the expression (2.12) for the integrated density of states,

$$
\begin{aligned}
I(\phi, T) &= 2\frac{\partial}{\partial \phi} \int_0^\infty d\epsilon \left(-\frac{\partial f}{\partial \epsilon} \right) \int^\epsilon d\epsilon' N(\epsilon', B) \\
&= 2\frac{\partial}{\partial \phi} \int_0^\infty d\epsilon \left(-\frac{\partial f}{\partial \epsilon} \right) \int^\epsilon d\epsilon' \left[\frac{L}{\pi} k(\epsilon') + \frac{2}{\pi} \sum_{p=1}^\infty \frac{\sin\left(pL\, k(\epsilon')\right)}{p} \cos(2\pi p\phi) \right] \\
&= 2\frac{\partial}{\partial \phi} \int_0^\infty d\epsilon \left(-\frac{\partial f}{\partial \epsilon} \right) \left[\frac{L}{\pi} \frac{\epsilon(\epsilon - 2\epsilon_F + 2k_F v_F)}{2v_F} \right. \\
&\quad \left. + \frac{2}{\pi} \sum_{p=1}^\infty \frac{\cos\left(pL\frac{(\epsilon-\epsilon_F)}{v_F}\right)}{p} \cos(2\pi p\phi) \right] .
\end{aligned}
$$

(2.21)

Since the derivative of the Fermi function is peaked at $\epsilon = \epsilon_F$ we can shift the lower bound of integration to minus infinity. Using the result

$$
\int_{-\infty}^\infty d\epsilon \left(-\frac{\partial f}{\partial \epsilon} \right) \cos(pkL) = \frac{\pi pL}{\beta v_F} \frac{1}{\sinh\left(\frac{\pi pL}{\beta v_F}\right)} \cos(pk_F L)
$$

(2.22)

we get

$$
I(\phi, T) = \frac{2}{\pi} \frac{ev_F}{L} \sum_{p=1}^\infty I_p(T) \sin(2\pi p\phi) ,
$$

(2.23)

where $I_p(T)$ are the harmonics of the current,

$$
I_p(T) = R(T/T_p) \cos(pk_F L) ,
$$

(2.24)

which are damped by the function

$$
R(T/T_p) = \frac{\pi pL}{\beta v_F} \frac{1}{\sinh\left(\frac{\pi pL}{\beta v_F}\right)} = \frac{T/T_p}{\sinh(T/T_p)} ,
$$

(2.25)

where we introduced the characteristic temperature $T_p = v_F/Lp\pi$. Since the temperature T_p is proportional to the mean level spacing $\Delta = \pi v_F/L$, we can conclude, that the persistent current in clean tings is exponentially damped once the temperature becomes of the order of Δ. In the diffusive regime it turns out, that the characteristic temperature is of order of the Thouless energy [5, 14].

2.4.2   Elastic disorder

Realistic mesoscopic samples always contain a certain density of impurities which are essential for the electric attributes of the system. For calculational convenience we assume a so called Gaussian white noise impurity potential [2]. This means that we assume both,

the positions and the potentials of the impurities to be random. The total impurity potential $U(\boldsymbol{r})$ is assumed to be a random function following a Gaussian distribution with zero average and a delta-correlated second moment,

$$\langle U(\boldsymbol{r}) \rangle = 0$$
$$\langle U(\boldsymbol{r}) U(\boldsymbol{r}') \rangle = \gamma_e \, \delta(\boldsymbol{r} - \boldsymbol{r}') \,, \tag{2.26}$$

where we defined $\gamma_e = 1/(2\pi\nu\tau_e)$, ν the density of states per unit volume at the Fermi level.

We thus introduced a disorder potential which is solely characterized by its elastic mean free time τ_e. Disorder averaged retarded and advanced Green functions take the form ([2], chapter 3)

$$\bar{G}^{R/A}(\boldsymbol{k}, \epsilon) = \frac{1}{\epsilon - \epsilon(\boldsymbol{k}) \pm \frac{\hbar i}{2\tau_e}} \tag{2.27}$$

and the average density of states can be expressed as the trace over the imaginary part of the retarded Greens function, yielding

$$\bar{\nu}(\epsilon) = \frac{1}{2\pi} \operatorname{tr}\left[\operatorname{Im} G^R(\boldsymbol{k}, \epsilon)\right] = \frac{1}{V} \sum_{\boldsymbol{k}} \frac{1}{2\pi\tau_e} \frac{1}{(\epsilon - \epsilon_{\boldsymbol{k}})^2 + (\hbar/2\tau_e)^2}$$

$$= \frac{1}{2\pi\tau_e} \int_0^\infty d\epsilon' \frac{\nu_0(\epsilon')}{(\epsilon - \epsilon')^2 + (\hbar/2\tau_e)^2} = \int_0^\infty d\epsilon' g(\epsilon - \epsilon') \, \nu_0(\epsilon') \,, \tag{2.28}$$

where $\nu_0(\epsilon)$ is the density of states without disorder potential introduced in Eq. (2.11), and we introduced the Lorentzian

$$g(\epsilon) = \frac{1}{2\pi\tau_e} \frac{1}{\epsilon^2 + (\hbar/2\tau_e)^2} \,. \tag{2.29}$$

The expression for the persistent current in a disordered ring can now be calculated in the same way as above. Linearizing the dispersion relation as in Eq. (2.20) again we get

$$\int_{-\infty}^\infty d\epsilon \, \frac{\cos(pkL)}{p} \, g(\epsilon - \epsilon_F) = e^{-pL/2l_e} \, \frac{\cos(pk_F L)}{p} \,, \tag{2.30}$$

where l_e is the elastic mean free path, i.e. the length of the path an electron can travel on average before being scattered by an impurity. Using this yields for the persistent current in a disordered system

$$I(\phi) = \frac{2}{\pi} \frac{e v_F}{L} \sum_{p=1}^\infty \frac{\cos(p k_F L)}{p} e^{-pL/2l_e} \sin(2\pi p \phi) \,, \quad \text{or, for fixed N,}$$

$$I(\phi) = \frac{2}{\pi} \frac{e v_F}{L} \sum_{p=1}^\infty \frac{(-1)^{pN}}{p} e^{-pL/2l_e} \sin(2\pi p \phi) \,. \tag{2.31}$$

We see, that all harmonics of the average current are exponentially damped if the elastic mean free path becomes small compared to the perimeter of the ring. Since the diffusive regime discussed in the following chapter assumes that the elastic mean free path and time are the smallest quantities in the system, we expect the average current to vanish in this case.

2.4.3 Diffusive regime

The motion of the electron in the ring is called diffusive if the elastic mean free path is small compared to the perimeter of the ring, $l_e \ll L$. This means that many scattering events are assumed when an electron travels once around the ring, and the mean free path l_e and time τ_e are the smallest quantities in the system. In metals the diffusive regime has been proven and tested on many occasions, which is why we assume to be in this regime for the remaining part of this chapter.

As we have shown in the previous chapter (Eq. (2.31)), the average current will vanish exponentially, if the perimeter of the ring is larger than the mean free path. Thus we will have to go beyond this and will show in a first step, that the variance of the current distribution will remain finite.

In a second step we will include electron-electron interactions and show, that they will lead to a finite average current even in the diffusive regime.

Typical current

We define the typical current as the square root of the variance of the current. Since the variance is $\overline{\delta I^2} = \overline{I^2} - \overline{I}^2$, the typical current is defined as

$$I_{\text{typ}} \equiv \overline{\delta I^2}^{1/2} . \tag{2.32}$$

Thus we start by calculating the variance of the current.

We consider an ensemble of mesoscopic rings with a finite cross section which is small compared to the perimeter of the ring, $L_{y,z} \ll L$. Thus the rings are quasi one-dimensional in the sense that we can evaluate the disorder average by considering a one-dimensional electronic motion. Starting from Eq. (2.4) and performing two partial integrations we get for the current at zero temperature

$$
\begin{aligned}
I(T = 0, \phi) &= -2 \int_0^{\epsilon_F} d\epsilon \left(\frac{\partial \nu(\epsilon, \phi)}{\partial \phi} \right) (\epsilon - \epsilon_F) \\
&= -2 \int_{-\epsilon_F}^0 d\epsilon \left(\frac{\partial \nu(\epsilon, \phi)}{\partial \phi} \right) \epsilon .
\end{aligned} \tag{2.33}
$$

The current-current correlation function becomes

$$\left\langle I(\phi) I(\phi') \right\rangle = 4 \partial_\phi \partial_{\phi'} \int_{-\epsilon_F}^0 d\epsilon' \int_{-\epsilon_F}^0 d\epsilon \left\langle \nu(\epsilon, \phi) \nu(\epsilon', \phi') \right\rangle , \tag{2.34}$$

while the variance of the current is equal to the current current correlation function at equal magnetic flux, $\overline{\delta I^2} = \langle I(\phi) I(\phi) \rangle$.

Density of states correlation function   We can see from Eq. (2.34) that the variance of the current depends crucially on the density of states-density of states (DOS-DOS) correlation function $\langle \nu(\epsilon, \phi) \nu(\epsilon', \phi') \rangle$. Calculating this function is a nontrivial task which
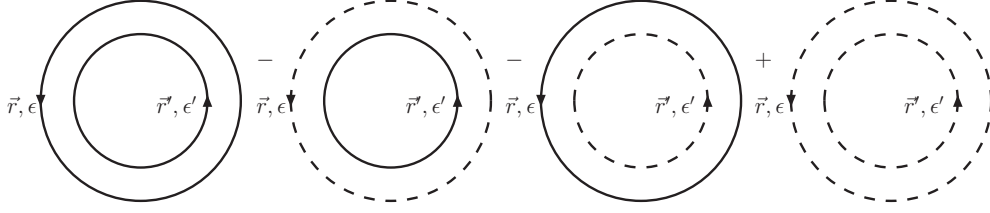
Figure 2.3: Diagram corresponding to Eq. (2.36). One dashed (solid) line from r to r' indexed with ϵ stands for the advanced (retarded) Green function $G^{A(R)}(r, r', \epsilon)$. Here the spatial arguments of the Green functions are identical for which reason the lines become circles. To read off the diagrams one has to include integrations over all spatial variables, each coming with a factor $\frac{1}{2\pi i}$.
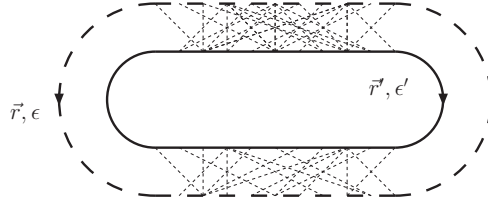
Figure 2.4: Diagram corresponding to the disorder average of the second term in Eq. (2.36). The dashed (solid) lines now stand for disorder averaged advanced (retarded) Green functions, and the dotted lines represent disorder lines

we will reproduce here[2], since it is a good framework to introduce several concepts for later purposes. The starting point is the expression for the density of states without disorder

$$\nu(\epsilon, \phi) = \frac{1}{2\pi} \operatorname{tr}\left[\operatorname{Im} G^A(\epsilon, \boldsymbol{k})\right] = \frac{1}{2\pi i} \operatorname{tr}\left[G^A(\epsilon, \boldsymbol{k}) - G^R(\epsilon, \boldsymbol{k})\right]$$

$$= \frac{1}{2\pi i} \int dr \left[G^A(r, r, \epsilon) - G^R(r, r, \epsilon)\right] . \tag{2.35}$$

The disorder averaged DOS-DOS correlation function thus takes the form

$$\langle \nu(\epsilon)\nu(\epsilon') \rangle = \frac{-1}{4\pi^2} \int dr \int dr' \left\langle G^A(r, r, \epsilon) G^A(r', r', \epsilon') - G^A(r, r, \epsilon) G^R(r', r', \epsilon') \right.$$

$$\left. - G^R(r, r, \epsilon) G^A(r', r', \epsilon') + G^R(r, r, \epsilon) G^R(r', r', \epsilon') \right\rangle . \tag{2.36}$$

Equations like (2.36) can be conveniently expressed in terms of diagrams. To introduce this concept, the diagrammatic representation of (2.36) is shown in Figure 2.3.

Performing the disorder average now means that we have to replace the advanced and retarded Green functions by disorder averaged ones (Eq. (2.27)) and draw disorder lines between the Green functions in all possible ways as indicated for the second term in Eq. (2.36) in Figure 2.4.

Two rather standard observations are introduced at this point. First, the largest contributions to disorder averages of two Green functions in the diffusive limit, $k_F l_e \gg 1$, come

---

[2]We follow roughly the presentations in [2, 5].
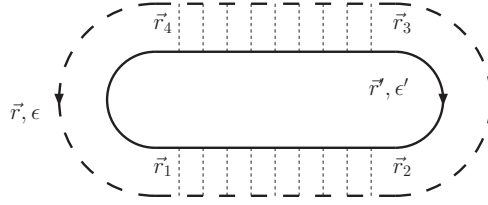
Figure 2.5: Diagram for the diffusion-like contribution to the density of states correlation function
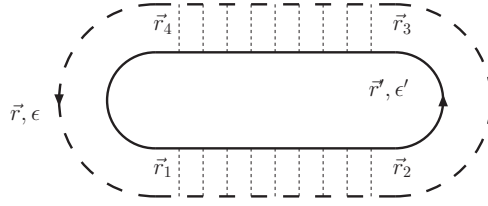
Figure 2.6: Diagram for the cooperon-like contribution to the density of states correlation function

from diagrams in which the disorder lines are not or maximally crossed (called diffusion and cooperon contributions). Second, the diagrams where two retarded or two advanced Green functions are connected are small compared to the mixed ones as well. Thus, using the fact, that G^R is the complex conjugate of G^A, Eq. (2.36) simplifies to

$$\langle \nu(\epsilon)\nu(\epsilon') \rangle = \frac{1}{2\pi^2} \mathrm{Re} \int dr \int dr' \left\langle G^A(r,r,\epsilon) G^R(r',r',\epsilon') \right\rangle . \qquad (2.37)$$

Figures 2.5 and 2.6 have to be understood in such a way, that they include summation over all possible numbers of impurity lines. This sums can be merged into the so called diffuson defined in Figure 2.7. From this equation we can deduce a Dyson-like equation whose diagrammatic representation is also shown in Figure 2.7. This equation for the
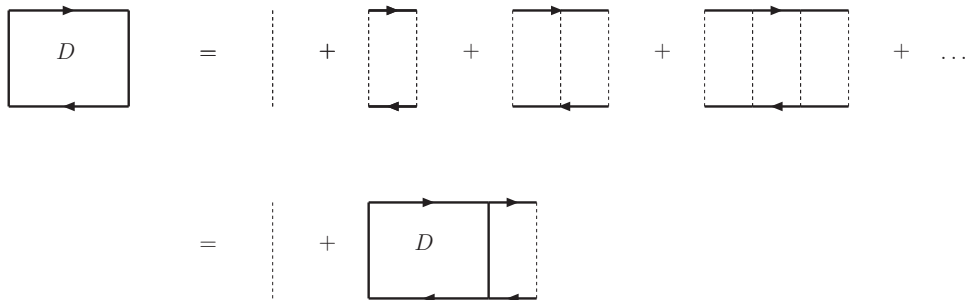
Figure 2.7: Definition of the diffuson as the sum over all impurity-ladder diagrams (first line) and the corresponding Dyson equation for the diffuson (second line).

diffuson is solved in Appendix A.1 in momentum and energy space and yields

$$D(\boldsymbol{q}, \omega) = \frac{(2\pi\nu\tau_e^2)^{-1}}{D\boldsymbol{q}^2 - i\omega/\hbar}, \tag{2.38}$$

where we introduced the diffusion constant $D = v_F^2 \tau_e/d$.

Splitting Eq. (2.37) into the diffuson and cooperon part shown in Figs. 2.5 and 2.6 yields

$$\langle \nu(\epsilon)\nu(\epsilon') \rangle_{\text{diff}} = \frac{1}{2\pi^2} \text{Re} \int dr \int dr' \int dr_1 \ldots dr_4 \Big[G^A(r, r_1, \epsilon) G^A(r_2, r_3, \epsilon) G^A(r_4, r, \epsilon)$$

$$G^R(r', r_2, \epsilon') G^R(r_1, r_4, \epsilon') G^R(r_3, r', \epsilon') \, D(r_1 - r_2, \epsilon - \epsilon') D(r_3 - r_4, \epsilon - \epsilon') \Big] \tag{2.39}$$

for the diffuson part. The cooperon part looks very similar to this one as can be seen in Figure 2.6 and will be included later.

The diffusons are slowly varying in space compared to the Green functions, and thus we can replace $r_2 \approx r_4 \approx r$ and $r_3 \approx r_2 \approx r'$ in the arguments of the diffusions. The integrals over r_1 and r_4 thus contain only disorder averaged retarded and advanced Green functions which just depend on the difference of their spatial arguments. Performing a Fourier transformation yields

$$\int dr_1 \int dr_4 G^A(r - r_1, \epsilon) G^R(r_1 - r_4, \epsilon') G^A(r_4 - r, \epsilon) = \frac{1}{V} \sum_{\boldsymbol{k}} G^A(\boldsymbol{k}, \epsilon) G^R(\boldsymbol{k}, \epsilon') G^A(\boldsymbol{k}, \epsilon). \tag{2.40}$$

We can solve this sum ([2], chapter 3) using $\epsilon - \epsilon' \ll \hbar/\tau_e$

$$\frac{1}{V} \sum_{\boldsymbol{k}} G^R(\boldsymbol{k}, \epsilon) \left(G^A(\boldsymbol{k}, \epsilon) \right)^2 = \nu \int \frac{d\xi}{\hbar} \left(\frac{\hbar}{\epsilon - \xi + i\hbar/2\tau_e} \right) \left(\frac{\hbar}{\epsilon - \xi - i\hbar/2\tau_e} \right)^2 \approx 2\pi i \nu \tau_e^2, \tag{2.41}$$

where we integrated around the pole at $\xi = \epsilon + i\hbar/2\tau_e$ in the last step. All sums over advanced and retarded Green functions will be evaluated this way in the remainder of the thesis. The integrals over r_2 and r_3 give the same result up to a minus sign, and we get

$$\langle \nu(\epsilon)\nu(\epsilon') \rangle_{\text{diff}} = \frac{1}{2\pi^2} \text{Re} \, (2\pi\nu\tau_e)^2 \int dr \int dr' \, D(r - r', \epsilon - \epsilon') \, D(r' - r, \epsilon - \epsilon')$$

$$= \frac{1}{2\pi} \text{Re} \sum_{\boldsymbol{q}} \left(\frac{1}{D\boldsymbol{q}^2 - i(\epsilon - \epsilon')/\hbar} \right)^2. \tag{2.42}$$

Up to this point the derivation for the cooperon-part of the correlation function is completely analogous. The difference occurs when we introduce a vector potential $\boldsymbol{A}$ which can lead to a flux through the ring and thus break the time reversal invariance. This is accounted for by replacing $D\boldsymbol{q}^2$ with the eigenvalues of the operator $D(\boldsymbol{\nabla}/i - \boldsymbol{A}\, 2e/\hbar)$, i.e.

by introducing the magnetic flux. Writing $\varphi_\pm = (\phi \pm \phi')/\phi_0$ we get assuming a quasi one dimensional motion ($L \gg L_{z,y}$)

$$\boldsymbol{q} = q_x = \frac{2\pi}{L}\left(n - \varphi_\pm\right) \tag{2.43}$$

where φ_+ (φ_-) stands for the cooperon (diffuson) contribution and n is an integer. The relevant energy scale for the diffusive motion is the Thouless energy $E_C = 4\hbar\pi^2 D/L^2 = \frac{\hbar}{\tau_D}$, τ_D the diffusion time which is the time an electron needs to travel around the ring. We can pull this energy out of the sums making the variables under the integral dimensionless. Performing a Poisson summation yields with $\tilde{\epsilon} = (\epsilon' - \epsilon)/E_C$

$$\langle \nu(\epsilon)\nu(\epsilon')\rangle_{\text{diff}} = \frac{1}{\pi^2}\text{Re}\sum_k \cos(2\pi k\varphi_-)\int dn \frac{e^{2\pi ikn}}{(E_C n^2/\hbar - i(\epsilon - \epsilon')/\hbar)^2}$$

$$= \frac{-\hbar^2}{\pi^2 E_C^2}\frac{\partial}{\partial\tilde{\epsilon}}\text{Im}\sum_k \cos(2\pi k\varphi_-)\int dn \frac{e^{2\pi ikn}}{n^2 + i\tilde{\epsilon}}. \tag{2.44}$$

The n-integral can be solved by means of the residue theorem and we get defining the branch cut of the complex square root on the negative real axis (i.e. $\sqrt{i} = e^{i\pi/4} = \frac{1+i}{\sqrt{2}}$)

$$\langle \nu(\epsilon)\nu(\epsilon')\rangle_{\text{diff}} = \frac{-1}{\pi^2 E_C^2}\frac{\partial}{\partial\tilde{\epsilon}}\sum_k \cos(2\pi k\varphi_-)\,\text{Im}\,\frac{e^{-2\pi k\sqrt{i\tilde{\epsilon}}}}{\sqrt{i\tilde{\epsilon}}}. \tag{2.45}$$

To get the cooperon contribution we just have to replace $varphi_-$ by φ_+.

Inserting Eq. (2.45) in the expression for the current fluctuations, Eq. (2.34) gives

$$\langle I(\phi)I(\phi')\rangle = 4\,\partial_\phi\partial_{\phi'}\int_{-\epsilon_F}^0 d\epsilon'\int_{-\epsilon_F}^0 d\epsilon\,\epsilon\,\epsilon'\left(\langle \nu(\epsilon,\phi)\nu(\epsilon',\phi')\rangle_{\text{diff}} + \langle \nu(\epsilon,\phi)\nu(\epsilon',\phi')\rangle_{\text{coop}}\right). \tag{2.46}$$

Shifting the lower integration bounds to minus infinity and introducing dimensionless sum- and difference variables

$$\sigma = \frac{1}{2}\frac{\epsilon + \epsilon'}{E_C}\,,\,\tau = \frac{\epsilon - \epsilon'}{E_C} \tag{2.47}$$

turns the ϵ and ϵ' integrals into

$$\int_{-\infty}^0 d\epsilon'\int_{-\infty}^0 d\epsilon\,\epsilon\,\epsilon'\left(\langle \nu(\epsilon,\phi)\nu(\epsilon',\phi')\rangle_{\text{diff}} + \langle \nu(\epsilon,\phi)\nu(\epsilon',\phi')\rangle_{\text{coop}}\right)$$

$$= -\frac{E_C^2}{\pi^2}\int_{-\infty}^0 d\sigma\int_{-2|\sigma|}^{2|\sigma|} d\tau\left(\sigma^2 - \frac{\tau^2}{4}\right)\sum_{k=1}^\infty [\cos(2\pi k\varphi_+) + \cos(2\pi k\varphi_-)]\,\partial_\tau\text{Im}\,\frac{e^{-2\pi k\sqrt{i\tau}}}{\sqrt{i\tau}} \tag{2.48}$$

This integral can be solved by integrating by parts. We get

$$\langle I(\phi)I(\phi')\rangle = 4\partial_\phi\partial_{\phi'}\frac{3E_C^2}{4\pi^6}\sum_{k=1}^\infty \frac{1}{k^5}[\cos(2\pi k\varphi_+) + \cos(2\pi k\varphi_-)]$$

$$= 4\frac{6E_C^2}{\pi^2\phi_0^2}\sum_{k=1}^\infty \frac{\sin\left(2\pi k\phi/\phi_0\right)\sin\left(2\pi k\phi'/\phi_0\right)}{k^3}. \tag{2.49}$$
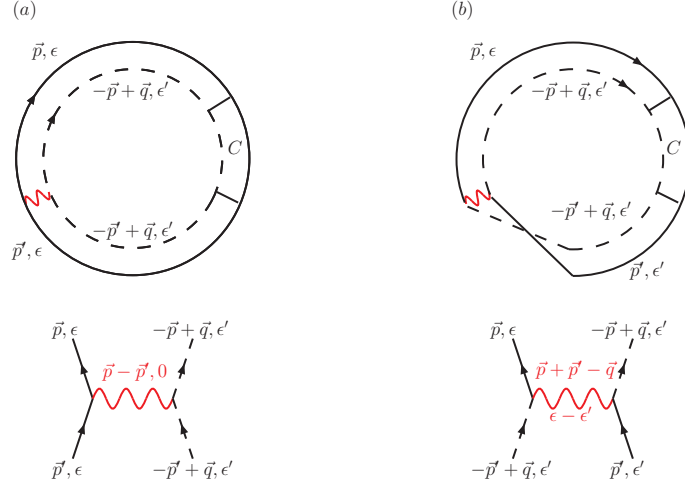
Figure 2.8: Diagrams for the grand potential corresponding to (a) the Hartree, and (b) the Fock term. The wavy lines represent Coulomb interactions (the figure resembles Fig. 1 in [24]).

This result agrees with the one found in Ref. [5]. Noting that $E_C/\phi_0 = e/(2\pi\tau_D)$ we see that we expect the typical current to be of order e/τ_D [5, 14, 23].

2.5 Electron electron interaction

In contradiction to the results of Section 2.3 first experimental results showed a finite average current. In order to explain this, Ambegaokar and Eckern [24] calculated the effect of electron-electron interaction on the average current, and found out that indeed a fluctuation produced by those interactions could trigger the coherent backscattering which in turn leads to a finite average current. It is important to emphasize, that this effect differs from the cases where the positive interference of an electron-hole pair at low energies leads to backscattering (as it is e.g. the case in the calculation of the weak-localization correction to the conductivity [2]), since the persistent current is an equilibrium property of the system. In this section we will briefly present the results of Ref. [24], limiting ourselves to the zero temperature case.

The diagrams for the grand potential in Hartree-Fock approximation are shown in Figure 2.8[3]. Reading off this diagrams we get for the Hartree term

$$\Omega_H = \frac{2}{V^3} \sum_{\boldsymbol{p},\boldsymbol{p}',\boldsymbol{q}} \int_{-\infty}^{0} \frac{d\epsilon\, d\epsilon'}{(2\pi)^2}\, G^R(\boldsymbol{p},\epsilon)\, G^R(\boldsymbol{p}',\epsilon)\, G^A(-\boldsymbol{p}+\boldsymbol{q},\epsilon')\, G^A(-\boldsymbol{p}'+\boldsymbol{q},\epsilon')$$
$$\times D(\boldsymbol{q},\epsilon-\epsilon')\, V(\boldsymbol{p}-\boldsymbol{p}')\,, \tag{2.50}$$

---

[3]Since this is the only part of the thesis dealing with interactions, we do not give a detailed introduction to the theory of interacting electrons, which can be found in [2] and [25].

while the Fock term reads

$$\Omega_F = -\frac{1}{V^3} \sum_{\boldsymbol{p},\boldsymbol{p}',\boldsymbol{q}} \int_{-\infty}^{0} \frac{d\epsilon\, d\epsilon'}{(2\pi)^2}\, G^R(\boldsymbol{p},\epsilon)\, G^R(\boldsymbol{p}',\epsilon)\, G^A(-\boldsymbol{p}+\boldsymbol{q},\epsilon')\, G^A(-\boldsymbol{p}'+\boldsymbol{q},\epsilon')$$
$$\times D(\boldsymbol{q},\epsilon-\epsilon')\, V(\boldsymbol{p}+\boldsymbol{p}'-\boldsymbol{q},\epsilon-\epsilon')\,, \tag{2.51}$$

where V is the volume of the system. The relative factor of two between the two terms results from the fact that we have to avoid double counting of the energy in the Fock term. Since the diffuson emphasizes small $\boldsymbol{q}$, we can again integrate out the Green functions, expanding around $\boldsymbol{q} \approx 0$ to first nontrivial order. We get[4]

$$\Omega_H + \Omega_F = \frac{(2\pi\nu\tau_e)^2}{2\pi\nu\tau_e^2} \int_{-\infty}^{0} \frac{d\epsilon\, d\epsilon'}{(2\pi)^2} \left\langle 2V(\boldsymbol{p}-\boldsymbol{p}',0) - V(\boldsymbol{p}+\boldsymbol{p}',\epsilon-\epsilon') \right\rangle \sum_{\boldsymbol{q}} \frac{1}{D\boldsymbol{q}^2 - i(\epsilon-\epsilon')}\,, \tag{2.52}$$

where the brackets denote an angular average. In the diffusive regime we can assume $\epsilon - \epsilon', \hbar D\boldsymbol{q}^2 \ll \hbar/\tau_e$ and the interaction $V(\boldsymbol{q},\epsilon)$ can be taken to be the screened Coulomb potential [25]

$$V(\boldsymbol{q},\epsilon) = \frac{4\pi e^2}{q^2} \frac{\epsilon + Dq^2}{Dq_{\mathrm{TF}}^2 + Dq^2 + \epsilon}\,, \tag{2.53}$$

where q_{TF} is the Thomas-Fermi wave number, $q_{\mathrm{TF}} = 8\pi\nu e^2$. The angular average yields a result which is in this regime independent of $\epsilon - \epsilon'$, so that we can replace the average of the potentials by $\bar{V} = \langle V(\boldsymbol{p}-\boldsymbol{p}',0) \rangle$, leading to the expression

$$\Omega_H + \Omega_F = 2\pi\nu\,\bar{V} \int_{-\infty}^{0} \frac{d\epsilon\, d\epsilon'}{(2\pi)^2} \sum_{\boldsymbol{q}} \frac{1}{D\boldsymbol{q}^2 - i(\epsilon-\epsilon')}\,. \tag{2.54}$$

The next step is to introduce the magnetic flux $\varphi \equiv \phi/\phi_0$. We follow the same steps as in Section 2.4.3, but take into account that we expect the average current to be $\phi_0/2$-periodic as it has been shown in Section 2.3[5]. Further we assume a quasi-one-dimensional motion again. After performing a Poisson summation we are left with

$$\Omega_H + \Omega_F = 4\pi\nu\,\bar{V}\, E_C \int_{-\infty}^{0} \frac{d\epsilon}{2\pi} \int_{-\infty}^{0} \frac{d\epsilon'}{2\pi} \sum_{p=1}^{\infty} \cos(4\pi p\varphi) \int_{-\infty}^{\infty} dn\, \frac{e^{2\pi i p n}}{n^2 - i(\epsilon-\epsilon')}\,, \tag{2.55}$$

where the variables which are integrated over are now dimensionless, E_C is the Thouless energy and we already left out the $p = 0$-term which will vanish when we take the ϕ-derivatives in Eq. (2.1), which still defines the average persistent current. The n-integral can be performed by residue calculus. With

$$\int_{-\infty}^{\infty} dn\, \frac{e^{2\pi i p n}}{n^2 - i(\epsilon-\epsilon')} = \pi\, e^{2\pi i p \sqrt{i(\epsilon-\epsilon')}} \sqrt{\frac{i}{\epsilon-\epsilon'}} \tag{2.56}$$

---

[4]We set $\hbar = 1$ in this section

[5]Note the definition $\phi_0 = h/2e$ in Ref. [24].

for $p > 0$, we are left with

$$\Omega_H + \Omega_F = \nu \, \bar{V} \, E_C \int_{-\infty}^{0} d\epsilon \int_{-\infty}^{0} d\epsilon' \sum_{p=0}^{\infty} \cos(4\pi p\varphi) e^{2\pi i p\sqrt{i(\epsilon-\epsilon')}} \sqrt{\frac{i}{\epsilon-\epsilon'}} . \qquad (2.57)$$

Introducing sum and difference variables $\sigma = \frac{1}{2}(\epsilon + \epsilon')$, $\tau = \epsilon - \epsilon'$ yields

$$\begin{aligned}
\Omega_H + \Omega_F &= \nu \, \bar{V} \, E_C \sum_{p=1}^{\infty} \cos(4\pi p\varphi) \int_{-\infty}^{0} d\sigma \int_{-2|\sigma|}^{2|\sigma|} d\tau \, e^{2\pi i p\sqrt{i\tau}} \sqrt{\frac{i}{\tau}} \\
&= \nu \, \bar{V} \, E_C \sum_{p=1}^{\infty} \cos(4\pi p\varphi) \int_{0}^{\infty} d\sigma \int_{0}^{2\sigma} d\tau \, e^{2\pi i p\sqrt{i\tau}} \sqrt{\frac{i}{\tau}} + c.c. \\
&= \nu \, \bar{V} \, E_C \sum_{p=1}^{\infty} \cos(4\pi p\varphi) \int_{0}^{\infty} d\sigma \, \frac{2 \, e^{-2\pi p\sqrt{\sigma}} \, \sin(2\pi p\sqrt{\sigma})}{\pi p} \\
&= 2\nu \, \bar{V} \, E_C \sum_{p=1}^{\infty} \frac{\cos(4\pi p\varphi)}{4p^3 \pi^3} . \qquad (2.58)
\end{aligned}$$

The average persistent current is still defined by Eq. (2.1), which yields

$$I = -\frac{1}{\phi_0} \frac{\partial(\Omega_H + \Omega_F)}{\partial\varphi} = \frac{4\nu \, \bar{V} \, E_C}{\phi_0} \sum_{p=1}^{\infty} \frac{\sin(4\pi p\phi/\phi_0)}{2p^2 \pi^2} , \qquad (2.59)$$

which is equal to the result in [24] at zero temperatures.

2.6 Summary

In this section we introduced the basic physical quantities which are available for an experimental examination of persistent currents in normal metal rings. Since most experiments examine the effect for a large number of rings, those quantities are essentially the average current introduced in Section 2.3 and the typical current introduced in Section 2.4.3. We argue that the diffusive regime at which we looked in Section 2.4.3 exhibits a good description of the metallic systems under consideration in experiments. In the noninteracting case we expect the average current to vanish, while the typical current is of order e/τ_D. We exploit the introduction to the field to introduce some basic concepts of theoretical condensed matter physics, like the calculation of the correlation function in Section 2.4.3, which will be required in our analysis.

Chapter 3

Experiments

As mentioned above, measurements of persistent currents in normal metal rings have been a challenging task in the past. The main reasons for this are the smallness of the effect[1], and the fact, that the sign of the persistent current varies randomly from ring to ring, depending on the detailed form of the disorder potential.

Since the magnitude of the effect is proportional to e/τ_D, where e is the charge of an electron and τ_D the diffusion time, i.e. the time it takes an electron to diffuse around the ring, experimentalists try to keep this time as small as possible e.g. by using rings with a small diameter. As we have shown above (Section 2.4.1) the persistent current vanishes exponentially when the temperature is raised. Thus the experiments have to be performed at low temperatures, too (typically below one Kelvin).

Another important aspect which makes the observation of persistent currents more complicated is, that since the effect crucially depends on the coherence of the electron wave function around the ring, the signal is destroyed if a device like an ammeter is put into the circuit. Thus one has to measure secondary effects of the persistent current, like the magnetic moment of the ring generated by the current, instead.

Most experiments to date measure the persistent current of a single, few or many rings via measuring the magnetization of the system using SQUID techniques. This strategy usually led to problems concerning the background magnetization of the substrate which possibly could explain why first experiments obtained results which were orders of magnitude larger than theoretical predictions[2]. Bluhm *et al.* [18] managed finally to get results in agreement to theory by measuring and subtracting also the background magnetization. However, recently an experiment by Bleszynski-Jayich *et al.* [14] used a different approach, measuring the frequency shift of a cantilever on which the rings are located due to the persistent current through the rings. This technique led to results which are in good agreement with the theoretical predictions (see also [23]).

In the following we will introduce this two recent experiments, by Bluhm *et al.* [18] and by Bleszynski-Jayich *et al.* [14]. After this we will comment on older experiments to depict the historical progress.

---

[1]We expect e.g. a persistent current of the order $I \sim 1nA$ for a ring with diameter one micrometer at $T \stackrel{<}{\sim} 1K$ [14]

[2]Other possible explanations include the role of a small amount of magnetic impurities [26].
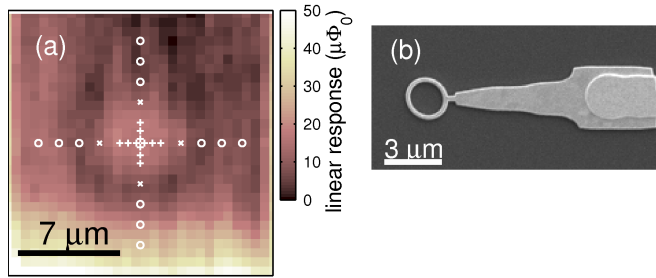
Figure 3.1: Experiment in Ref. [18]. (a) Susceptibility scan of a ring. The + labels the positions where the ring is located and its susceptibility is measured, while the circles indicate background measurements around the ring. (b) Scanning electron picture of a ring which is connected to a heat bath. Picture taken from [18].

3.1   Bluhm *et al.* – measuring one ring at a time

The first of the two recent experiment on persistent current in normal metal ring was performed by Bluhm *et al.* [18] in 2009. The group measured the magnetic response of gold rings, one at a time, using a scanning SQUID microscope [27]. This enabled them to perform in situ measurements [28, 29] on the rings. They measured heat isolated rings as well as heat sunk rings (Figure 3.1 (b)).

Measuring the background magnetization symmetrically close around the ring as it is shown in Figure 3.1 enabled them to eliminate variations of the sensor background and thus to deduct the persistent current part of the signal. A careful analysis of the achieved data lead to results for the current current fluctuations which are close to the theoretical predictions in magnitude and periodicity (Figure 3.2). They also measured the predicted temperature dependence.

Another result which will be interesting for our considerations (see Section 4.4.2) is, that comparing the data obtained for the linear susceptibility of the isolated and heat sunk rings showed, the electron temperature rather than the phonon temperature in the ring to be crucial for their measurements.

3.2   Bleszynski-Jayich *et al.* - rings on a cantilever

This group used a quite different approach to determine the persistent current in mesoscopic rings. Instead of measuring the magnetization of the rings by means of a SQUID device, they used a micro-mechanical detector, i.e., they located the rings on a single-crystal Si cantilever (see Figure 3.3) and measured the shift of the cantilevers resonance frequency due to the persistent currents in the rings.

A ring with radius R carrying a current I and exhibits a magnetic moment $\boldsymbol{\mu} = \pi R^2 I \hat{n}$, where $\hat{n}$ is the unit vector perpendicular to the ring. In presence of a magnetic field B the ring causes not only a torque $\boldsymbol{\tau} = \boldsymbol{\nu} \times \boldsymbol{B}$ on the cantilever, but also a shift $\delta\nu$ of its resonance frequency. The idea of the experiment of Bleszynski-Jayich *et al.* is to measure this shift in the resonance frequency and to backtrack it on the persistent current carried
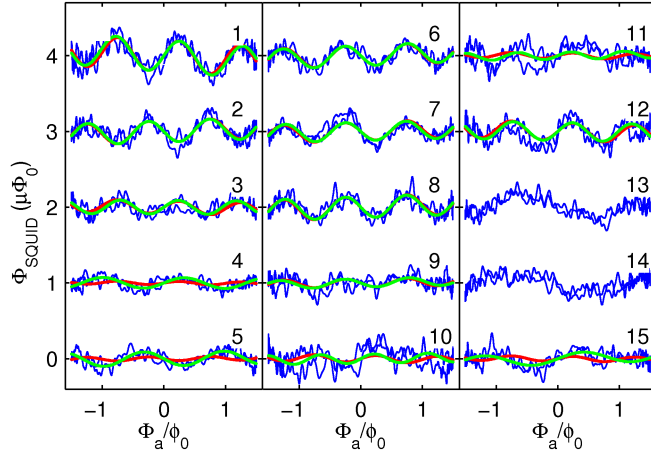
Figure 3.2: Response of 15 rings after subtracting the linear response components and an average background attributed to the spin signal. The red sinusoidal fits have a fixed, while the green ones have a fitted period. Picture taken from [18].

by the rings on the cantilever[3].

This technique enabled them to measure the persistent current of an array of many rings (Figure 3.4) as well as single rings (Figure 3.5) over a large range of magnetic field strength with much higher sensitivity and lower backaction than in the SQUID-based experiments. Not only the results on average and typical current, but also the measured temperature dependencies matched the theoretical predictions for non-interacting diffusive electrons.

3.3 Other experiments

For the sake of completeness and to illustrate the historic progress, we will comment on some older experiments performed on persistent currents in this section.

Lévy *et al.*, 1990   In 1990 Lévy *et al.* measured the magnetization response of 10^7 copper rings using a SQUID magnetometer [15]. Although they managed to reproduce the theoretically predicted period of ϕ_0 for the average current, which was calculated in Section 2.5, the measured amplitude was more than five times larger than theoretical predictions suggest.

Chandrasekhar *et al.*, 1991   Here, in contrast to Lévy *et al.*, the magnetic response of a single ring was measured. The group also used a SQUID device and managed to measure the theoretically predicted period of ϕ_0 [16].

As in the preliminary experiment by Lévy, also here results for the average persistent current where two orders of magnitude higher than the theoretical predictions.

---

[3]The exact correlation between frequency shift and persistent current is calculated in chapter two of the supporting online material [30]
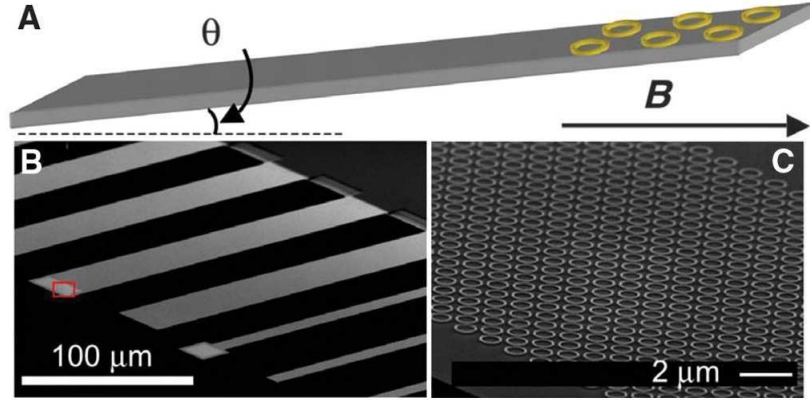
Figure 3.3: Experiment of Bleszynski-Jayich *et al.* [14].(A) Schematic picture of the cantilever populated with Al rings and the magnetic field $\boldsymbol{B}$. The magnetic flux through the rings is accomplished by the out-of-plane component of $\boldsymbol{B}$. (B) Scanning electron micrograph of several cantilevers. (C) Enhanced view of the red square in (B). Picture taken from [14].

Mailly *et al.*, 1993 The first measurements of the persistent current in semiconducting rings was performed by Mailly *et al.* in 1993 [31]. They used a special technique to measure the magnetization, where the ring and the SQUID device are located on the same chip.

The results coincided with the theoretical predictions both in magnitude and periodicity of the persistent currents, but where performed in a regime with weak disorder and a small number of channels.

Jariwala *et al.*, 2001 The last experiment we want to mention here was performed by Jariwala *et al.* in 2001 [17]. They measured the magnetic response of thirty diffusive gold rings using a SQUID gradiometer design.

The group measured persistent currents with flux periodicities of h/e and $h/2e$ of a magnitude comparable to the Thouless energy, i.e., orders of magnitudes larger than theoretical predictions. They tried to explain their results with an ac noise induced diamagnetic DC current in the ring [6, 32].
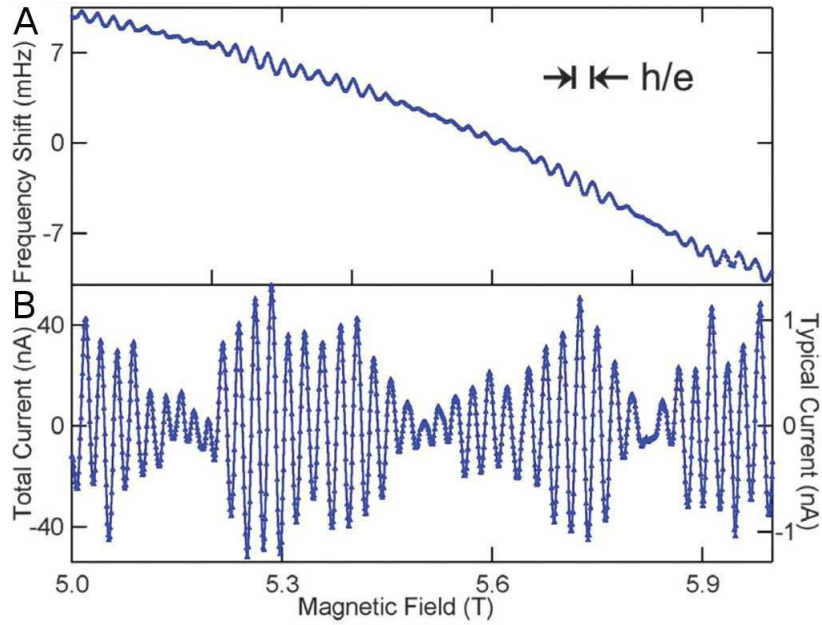
Figure 3.4: Shift of the resonant frequency in the experiment on 1680 rings with a radius of 308 nm at T =365 mK. In (A) the raw data and in (B) the data after subtraction of a smooth background are shown. Picture taken from [14].
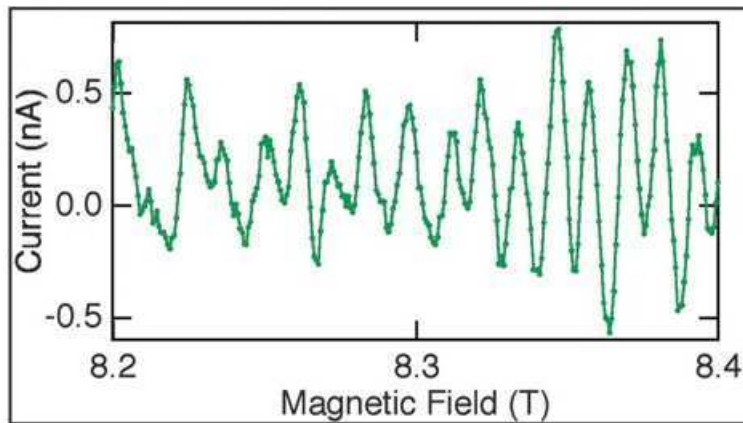
Figure 3.5: Shift of the resonant frequency in the experiment by Bleszynski-Jayich *et al.* on one ring with radius 418 nm at T =365 mK after subtraction of a smooth background. Picture taken from [14].

Chapter 4

Influence of an additional microwave field on persistent currents

In this third section of the first part of the thesis we will derive the results from our work on persistent currents under the irradiation of a microwave field. Since the microwave field will drive the electronic distribution function out of equilibrium we will treat the problem in the Keldysh formalism [20, 19] which is briefly introduced in Section 4.1.

The detailed formalism which we will use for our calculation is demonstrated with the help of the derivation of the equilibrium results in the Keldysh formalism in Section 4.2. After this we turn to the derivation of the central results of the first part of the thesis, i.e. the persistent current in normal metal rings under the influence of an additional microwave field, Section 4.3. The validity of the assumptions we made in our calculation as well as the magnitude of the effect is discussed in Section 4.4, before we show the calculation and present the results in Section 4.5. We conclude in Section 5.

4.1   Introduction to Keldysh formalism

Since the objective of this chapter is to calculate the consequences of an additional microwave field on the persistent currents in metal rings, which will drive the electronic distributions out of their equilibrium form, we have to use a formalism which is able to treat out-of-equilibrium processes inherently. This is accomplished by the so called Keldysh formalism [20] which we will introduce in this section.

The Kelsysh formalism uses real-time Green functions to derive transport properties of metals. An exhaustive introduction can be found in Ref. [19], which we will follow in the remainder of this section.

Green functions

As we have already seen in the calculations of Section 2, Green functions exhibit a useful connection between calculable and experimentally relevant quantities in statistical physics. To put the formalisms used so far on a firm footing we begin this section by introducing the Green functions which will be utilized in the following calculations. The greater and

lesser Green functions are defined as

$$G^>(1,1') = -i \left\langle \hat{\psi}(1)\hat{\psi}^\dagger(1') \right\rangle$$

$$G^<(1,1') = \pm i \left\langle \psi^\dagger(1')\hat{\psi}(1) \right\rangle , \qquad (4.1)$$

where $\hat{\psi}$ and $\hat{\psi}^\dagger$ are electronic annihilation and creation operators, the upper sign stands for fermions and the lower sign for bosons and 1 and 1' denote appropriate variables, e.g. $1 \hat{=} (x_1, t_1)$. In addition the retarded and advanced Green functions are defined as expectation values of the commutators of annihilation and creation operators,

$$G^R(1,1') = -i\theta(t_1 - t_1') \left\langle \left[\hat{\psi}(1), \hat{\psi}^\dagger(1') \right]_\pm \right\rangle$$

$$G^A(1,1') = i\theta(t_1' - t_1) \left\langle \left[\hat{\psi}(1), \hat{\psi}^\dagger(1') \right]_\pm \right\rangle , \qquad (4.2)$$

where $\theta(t)$ is the Heaviside function. The connection between retarded, advanced, greater and lesser Green function can readily be seen,

$$G^R(1,1') = \theta(t_1 - t_1') \left[G^>(1,1') - G^<(1,1') \right]$$

$$G^A(1,1') = \theta(t_1' - t_1) \left[G^<(1,1') - G^>(1,1') \right] . \qquad (4.3)$$

Finally we also introduce time ordered Green functions

$$G(1,1') = -i \left\langle T_t \hat{\psi}(1)\hat{\psi}^\dagger(1') \right\rangle$$

$$= -i\theta(t_1 - t_1') \left\langle \hat{\psi}(1)\hat{\psi}^\dagger(1') \right\rangle \pm \theta(t_1' - t_1) \left\langle \psi^\dagger(1')\hat{\psi}(1) \right\rangle$$

$$= \theta(t_1 - t_1')G^>(1,1') + \theta(t_1' - t_1)G^<(1,1') , \qquad (4.4)$$

where the time ordering operator is implicitly defined in the second line of the equation. In the same way one can also define a contour ordered Green function, where the operators are not ordered along the time axis, but by their location on some contour.

Time evolution

In order to deal with a system out of equilibrium we assume that the system is in equilibrium prior to some reference time t_0, long before the times we are interested in. At time t_0 a known perturbation is switched on slowly. The Hamiltonian of the system takes the form

$$\hat{H} = \hat{H}_0 + \hat{U}(t) , \qquad (4.5)$$

where $\hat{U}(t) = 0$ for $t < t_0$. To derive an equation for the time evolution of the Green functions we switch to interaction and Heisenberg pictures. Any observable $A_H(t)$ in the Heisenberg picture satisfies the equation

$$\hat{A}_H(t) = T_c \, e^{-\frac{i}{\hbar} \int_c dt' \hat{U}(t')} \hat{A}(t) , \qquad (4.6)$$
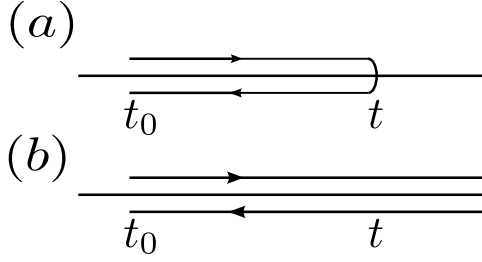
Figure 4.1: Contour used in equation (4.6). (a) The originally used contour starts at time t_0, goes to time t and back. This contour can be deformed to the so called Keldysh contour (b), since the additional integration areas simply cancel.
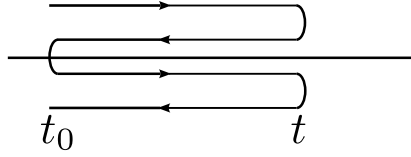
Figure 4.2: Contour used in equation (4.7). The contour now goes twice from t_0 to t - one time for each time evolution of ψ and $\psi^\dagger$.

where $A(t)$ is supposed to be in the interaction picture. The contour c used in equation (4.6) is depicted in Figure 4.1

Using this expression for the time evolution of operators, we can now deduce the time evolution of the Green functions defined in Section 4.1. The greater Green function takes the form

$$G^>(1,1') = -i \left\langle T_c \, e^{-\frac{i}{\hbar} \int_c d\tau U(\tau)} \psi(1)\psi^\dagger(1') \right\rangle_0 , \qquad (4.7)$$

where the integration contour is depicted in Figure 4.2. The main advantage of equation (4.7) is that the average can be taken at time t_0 when the interaction is absent, i.e. the system can be assumed to be in equilibrium. However the integration contour (Figure 4.2) becomes quite complicated. Fortunately also this problem is simplified when calculating the time evolution of a contour ordered Green function. The time evolution still reads

$$G(1,1') = -i \left\langle T_c \, e^{-\frac{i}{\hbar} \int_c d\tau U(\tau)} \psi(1)\psi^\dagger(1') \right\rangle_0 , \qquad (4.8)$$

but we can deform the contour in Figure 4.2 to the Keldysh contour in Figure 4.1(b), since the time that appears on the left in the Green function is always later on the contour anyway. Using this we can define a two by two matrix Green function

$$\underline{\tilde{G}}(1,1') = \begin{pmatrix} G_{11}(1,1') & G_{12}(1,1') \\ G_{21}(1,1') & G_{22}(1,1') \end{pmatrix} , \qquad (4.9)$$

where first index of $G_{ij}(1,1')$ indicates if the left time is on the upper (1) or lower (2) branch of the Keldysh contour and the second index indicates the right time in the same

way. Exploiting the above definitions of the respective Green functions we see, that this matrix Green function can be written as

$$
\underline{\tilde{G}}(1,1') = \begin{pmatrix} -i\left\langle T_t\psi_H(1)\psi_H^\dagger(1')\right\rangle & G^<(1,1') \\ G^>(1,1') & -i\left\langle \tilde{T}_t\psi_H(1)\psi_H^\dagger(1')\right\rangle \end{pmatrix}, \tag{4.10}
$$

where $\tilde{T}_t$ denotes "anti time ordering"

$$
-i\left\langle \tilde{T}_t\psi_H(1)\psi_H^\dagger(1')\right\rangle = -i\theta(t_1'-t_1)\left\langle \psi_H(1)\psi_H^\dagger(1')\right\rangle \pm i\theta(t_1-t_1')\left\langle \psi_H^\dagger(1')\psi_H(1)\right\rangle. \tag{4.11}
$$

For calculational purposes one usually chooses a more convenient representation of the matrix Green function introduced by Larkin and Ovchinnikov [33]. Performing an invertible transformation in Keldysh space,

$$
\underline{G}(1,1') = \frac{1}{2}\begin{pmatrix} 1 & 1 \\ 1 & -1 \end{pmatrix} \underline{\tilde{G}}(1,1') \begin{pmatrix} 1 & 1 \\ -1 & 1 \end{pmatrix}, \tag{4.12}
$$

one obtains

$$
\underline{G}(1,1') = \begin{pmatrix} G^R(1,1') & G^K(1,1') \\ 0 & G^A(1,1') \end{pmatrix}, \tag{4.13}
$$

where we defined the Keldysh Green function

$$
G^K(1,1') = G^>(1,1') + G^<(1,1'). \tag{4.14}
$$

In equilibrium the matrix Green function will just depend on the difference of the variables, $\underline{G}(1,1') = \underline{G}(1-1')$ and it turns out that the Fourier transform of the Keldysh Green function satisfies

$$
G^K(\boldsymbol{k},\omega) = \left(G^R(\boldsymbol{k},\omega) - G^A(\boldsymbol{k},\omega)\right)\frac{e^{\beta\hbar\omega}-(\pm1)}{e^{\beta\hbar\omega}+(\pm1)} = \left(G^R(\boldsymbol{k},\omega) - G^A(\boldsymbol{k},\omega)\right)(1-2n(\omega)), \tag{4.15}
$$

where $n(\omega) = \frac{1}{e^{\beta\hbar\omega}\pm1}$ is the distribution function.

Perturbation expansion

Aiming at an expression for the current involving the matrix Green function in Eq. (4.13), we will derive a perturbation expansion for the matrix Green function. We choose an electric field expressed by a vector potential, $\boldsymbol{A} = \frac{E}{i\omega}e^{-i\omega t}$ as the perturbation, which contributes a term $\boldsymbol{j}\cdot\boldsymbol{A}$ to the Hamiltonian. The impurity potential can be included in the unperturbed Hamiltonian H_0. Thus we can choose $U(t) = \boldsymbol{j}\cdot\boldsymbol{A}$ as the perturbation. The perturbation expansion for the contour ordered Green function can be derived from equation (4.4) by expanding the exponential and apply Wick's theorem [34, 35]

$$
\left\langle T_c\psi(1)\dots\psi(n)\psi^\dagger(n')\dots\psi^\dagger(1')\right\rangle = i^n\sum_{\mathcal{P}}(-1)^{\mathcal{P}}G^0(1,\mathcal{P}(1))\dots G^0(n,\mathcal{P}(n)), \tag{4.16}
$$

where $\mathcal{P}$ denotes a permutation and the sum goes over all possible permutations. The contour ordered Green function takes to first order in the perturbation the form

$$G^{(1)}(1,1') = \int d\boldsymbol{x}_2 \int_c dt_2 G^{(0)}(1,2) \, U(2) \, G^{(0)}(2,1') \,, \tag{4.17}$$

where the time t_2 is integrated over the Keldysh contour from Figure 4.1(b) and thus $\int_c d\tau \ldots \hat{=} \int_{-\infty}^{\infty} dt \, [\text{upper branch}] - \int_{-\infty}^{\infty} dt \, [\text{lower branch}]$. Using this we can write down a perturbation expansion of the matrix Green function. Defining $\hat{U} = U\tau_3$, where τ_3 is the third Pauli matrix, we get

$$\underline{G}_{ij}^{(1)}(1,1') = \int d\boldsymbol{x}_2 \int_{-\infty}^{\infty} dt_2 \, \underline{G}_{ik}^{(0)}(1,2) \, \hat{U}_{kk'}(2) \, \underline{G}_{k'j}^{(0)}(2,1') \,, \tag{4.18}$$

where the Einstein sum convention is assumed. Plugging in the chosen form of the perturbation, we get in real space and time

$$\underline{G}^{(1)}(1,1') = \frac{ie}{2m} \int d2 \, \boldsymbol{A}(2) \left[\left(\nabla_{x_2} - \nabla_{x_2'} \right) \underline{G}(1,2') \underline{G}(2,1') \right]_{2'=2} \,, \tag{4.19}$$

which can serve as a starting point for calculations of the current. We will truncate the discussion of the Keldysh formalism and derive further expressions like the second correction to the matrix Green function in the following text where they are needed. Closing this introductive section we note, that we can deduce from the matrix Green function to the Green functions directly related to physical properties by multiplying with proper Pauli matrices and taking the trace. The lesser Green function which we will need to calculate the current is for example given by

$$G^<(1,1') = \text{tr} \, \frac{1}{2} \, (\tau_1 - \tau_3) \, \underline{G}(1,1') \,, \tag{4.20}$$

as one can see directly by plugging in the definitions.

4.2 Derivation of equilibrium persistent current in Keldysh formalism

In this section we rederive the results from Section 2.4.3 in the Keldysh formalism. The calculations will be in the end very much the same as before, but we will gain important insights on how to handle the problem in the presence of an additional microwave field.

We start by deriving an expression for the current in zeroth order in the microwave field. The current can be expressed as [19]

$$j(1) = -\frac{e\hbar}{2m} \left[\nabla_1 - \nabla_{1'}\right] G^<(1,1')\big|_{1=1'} , \tag{4.21}$$

where 1 (1') abbreviates $\boldsymbol{x}_1, t_1$ ($\boldsymbol{x}_1', t_1'$). Using the definitions from Section 4.1 we can rewrite the current as

$$j(1) = -\frac{e\hbar}{4m} \operatorname{tr} (\tau_1 - \tau_3) \left[\nabla_1 - \nabla_{1'}\right] \underline{G}(1,1')\big|_{1=1'} , \tag{4.22}$$

where τ_i are the Pauli matrices. Fourier transforming this expression to $(\boldsymbol{k}, \omega)$ space turns the expression for the current into

$$
\begin{aligned}
j(1) &= -\frac{e\hbar}{4m} \operatorname{tr} (\tau_1 - \tau_3) \left[\nabla_1 - \nabla_{1'}\right] \frac{1}{V} \sum_{k_1, k_1'} e^{ik_1 x_1} e^{ik_1' x_1'} \underline{G}(k_1, t_1, k_1', t_1')\bigg|_{1=1'} \\
&= -\frac{e\hbar}{4m} \frac{1}{V} \sum_{k_1, k_1'} (ik_1 + ik_1') \operatorname{tr} (\tau_1 - \tau_3) e^{ik_1 x_1} e^{ik_1' x_1'} \int \frac{d\omega}{2\pi} e^{-i\omega(t_1 - t_1')} \underline{G}(k_1, k_2, \omega)\bigg|_{1=1'} \\
&= -\frac{e\hbar}{4m} \frac{1}{V} \sum_{k_1, k_1'} (ik_1 + ik_1') \operatorname{tr} (\tau_1 - \tau_3) e^{i(k_1 - k_1')x_1} \int \frac{d\omega}{2\pi} \underline{G}(k_1, k_2, \omega) .
\end{aligned} \tag{4.23}
$$

Averaging over the volume yields

$$j(1) = -\frac{e\hbar}{4m} \frac{1}{V} \sum_k 2ik \int \frac{d\omega}{2\pi} \operatorname{tr} (\tau_1 - \tau_3) \underline{G}(k, \omega) . \tag{4.24}$$

In the presence of an external field we can start to expand the matrix Green function at this point. Since we assume that there is no additional field yet, we can use the zeroth order matrix Green function. Inserting the equilibrium form of the Keldysh Green function, Eq. (4.15), Eq. (4.22) turns into

$$j(1) = -i\frac{e\hbar}{m} \frac{1}{V} \sum_k k \int \frac{d\omega}{2\pi} n(\omega) \left[G^A(k, \omega) - G^R(k, \omega)\right] . \tag{4.25}$$

This expression is illustrated in Figure 4.3.

In order to calculate current-current fluctuations we have to combine two of the loops shown in Figure 4.3 in all possible topologically distinct ways. As argued above the diagrams where two retarded or two advanced Green functions are combined are small in the
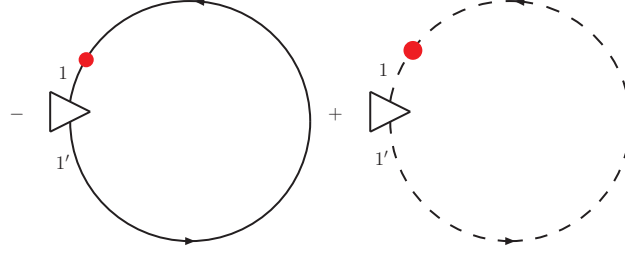
Figure 4.3: The equilibrium current in Keldysh formalism. Solid lines stand for retarded and dashed lines for advanced Green functions. The red dot stands for the distribution function, and the triangles for current vertices $-i\frac{e\hbar}{m}k$.

diffusive limit. We are left with the diagrams in Figure 4.4 [5]. Reading off the diagrams in Figure 4.4 gives for the current-current fluctuations in x-direction, i.e. in the direction along the ring, the expression

$$\langle j_x j_x \rangle = \left(\frac{\hbar^2 e^2}{m^2 V^2} \right) \sum_{\boldsymbol{k},\boldsymbol{k}'} k_\alpha \, k'_\beta \int \frac{d\epsilon d\epsilon'}{(2\pi)^2} \, n(\epsilon) \, n(\epsilon') \, G^R(\boldsymbol{k},\epsilon)^2 \, G^A(\boldsymbol{k}',\epsilon')^2$$

$$\left[D(\boldsymbol{k}-\boldsymbol{k}',\epsilon-\epsilon') + C(\boldsymbol{k}+\boldsymbol{k}',\epsilon-\epsilon') \right.$$

$$+ \frac{1}{V} \sum_{\boldsymbol{p}} G^R(\boldsymbol{k}-\boldsymbol{p},\epsilon) \, G^A(\boldsymbol{k}'+\boldsymbol{p},\epsilon') \, D(\boldsymbol{k}-\boldsymbol{k}'-\boldsymbol{p},\epsilon-\epsilon')^2$$

$$\left. + \frac{1}{V} \sum_{\boldsymbol{p}} G^R(\boldsymbol{k}-\boldsymbol{p},\epsilon) \, G^A(\boldsymbol{k}'-\boldsymbol{p},\epsilon') \, C(\boldsymbol{k}+\boldsymbol{k}'-\boldsymbol{p},\epsilon-\epsilon')^2 \right], \qquad (4.26)$$

where we used

$$D(\boldsymbol{k}-\boldsymbol{k}',\omega) = \frac{\gamma_e}{V\tau_e} \frac{1}{D(\boldsymbol{k}-\boldsymbol{k}')^2 - i\omega/\hbar}, \quad \text{and}$$

$$C(\boldsymbol{k}+\boldsymbol{k}',\omega) = \frac{\gamma_e}{V\tau_e} \frac{1}{D(\boldsymbol{k}+\boldsymbol{k}')^2 - i\omega/\hbar}. \qquad (4.27)$$

We can eliminate the $\boldsymbol{p}$-dependence of the cooperons and diffusons by substituting $\boldsymbol{k}' \to \boldsymbol{k}' \mp \boldsymbol{p}$ in the last two lines, leading to

$$\langle j_x j_x \rangle = \left(\frac{\hbar^2 e^2}{m^2 V^2} \right) \sum_{\boldsymbol{k},\boldsymbol{k}'} k_\alpha \, k'_\beta \int \frac{d\epsilon d\epsilon'}{(2\pi)^2} \, n(\epsilon) \, n(\epsilon') \, G^R(\boldsymbol{k},\epsilon)^2 \, G^A(\boldsymbol{k}',\epsilon')$$

$$\left[G^A(\boldsymbol{k}',\epsilon') \, D(\boldsymbol{k}-\boldsymbol{k}',\epsilon-\epsilon') + G^A(\boldsymbol{k}',\epsilon') \, C(\boldsymbol{k}+\boldsymbol{k}',\epsilon-\epsilon') \right.$$

$$+ \frac{1}{V} \sum_{\boldsymbol{p}} G^R(\boldsymbol{k}-\boldsymbol{p},\epsilon) \, G^A(\boldsymbol{k}'-\boldsymbol{p},\epsilon')^2 \, D(\boldsymbol{k}-\boldsymbol{k}',\epsilon-\epsilon')^2$$

$$\left. + \frac{1}{V} \sum_{\boldsymbol{p}} G^R(\boldsymbol{k}-\boldsymbol{p},\epsilon) \, G^A(\boldsymbol{k}'+\boldsymbol{p},\epsilon')^2 \, C(\boldsymbol{k}+\boldsymbol{k}',\epsilon-\epsilon')^2 \right]. \qquad (4.28)$$
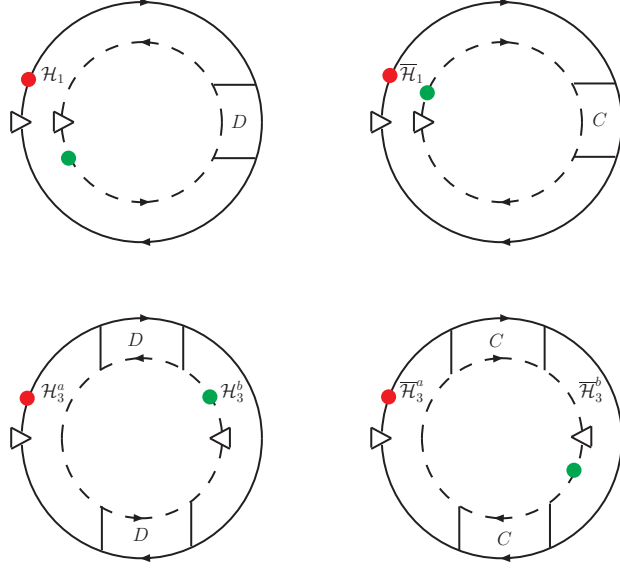
Figure 4.4: The diagrams needed for the calculation of the current-current fluctuations. The triangles stand for current vertices, straight (dashed) lines for retarded (advanced) Green functions and the red and green dots for distribution functions, where green dots come with an additional minus sign.

Since the cooperons and diffusons can be assumed to be long ranged in real space, we can expand in small $\boldsymbol{k} \mp \boldsymbol{k}'$ in the diffuson/cooperon terms respectively. The so called Hikami boxes consist of those Greens functions which are short ranged in momentum space and can be expanded. They are indicated in Figure 4.4 by calligraphic $\mathcal{H}$'s, are the same as those we need later in presence of an AC field and are calculated in Appendix A.3. Using the result

$$
\begin{aligned}
\mathcal{H}_1 &= -\left(\frac{e\hbar}{\pi}\right)^2 \frac{v_F^2}{d}\, \delta_{\alpha,\beta}\, \frac{2\tau_e^2}{\gamma_e}\,, \\
\mathcal{H}_3^a &= i\,\frac{e\hbar}{\pi}\,\frac{v_F^2}{d}\,\frac{2\tau_e^2}{\gamma_e}\,(\boldsymbol{k}-\boldsymbol{k}')\,, \\
\mathcal{H}_3^b &= -i\,\frac{e\hbar}{\pi}\,\frac{v_F^2}{d}\,\frac{2\tau_e^2}{\gamma_e}\,(\boldsymbol{k}-\boldsymbol{k}')
\end{aligned}
\tag{4.29}
$$

for the diffuson Hikami boxes, and

$$
\begin{aligned}
\overline{\mathcal{H}}_1 &= \left(\frac{e\hbar}{\pi}\right)^2 \frac{1}{V}\sum_{\boldsymbol{k}} v_\alpha\, v_\beta\, G^R(\boldsymbol{k},\epsilon)^2\, G^A(\boldsymbol{k}',\epsilon')^2 = \left(\frac{e\hbar}{\pi}\right)^2 \frac{v_F^2}{d}\, \delta_{\alpha,\beta}\, \frac{2\tau_e^2}{\gamma_e}\,, \\
\overline{\mathcal{H}}_3^a &= \overline{\mathcal{H}}_3^b = i\,\frac{e\hbar}{\pi}\,\frac{v_F^2}{d}\,\frac{2\tau_e^2}{\gamma_e}\,(\boldsymbol{k}+\boldsymbol{k}')
\end{aligned}
\tag{4.30}
$$

for the cooperon Hikami boxes, we arrive at the expression

$$\langle j_x j_x \rangle = 2 \left(\frac{e\hbar}{\pi m} \right)^2 \frac{1}{V^2} \int d\omega \int d\omega' \, n(\omega) \, n(\omega') \, D \, V \frac{2\tau_e}{\gamma_e}$$

$$\sum_q \left\{ D(\boldsymbol{q}_-, \omega - \omega') - C(\boldsymbol{q}_+, \omega - \omega') \right.$$

$$\left. - D \, V \frac{2\tau_e}{\gamma_e} \left[\boldsymbol{q}_-^2 \, D^2(\boldsymbol{q}_-, \omega - \omega') - \boldsymbol{q}_+^2 \, C^2(\boldsymbol{q}_+, \omega - \omega') \right] \right\}, \qquad (4.31)$$

where we introduced $\boldsymbol{q}_\pm = \boldsymbol{k} \pm \boldsymbol{k}'$. If the ring is essentially one dimensional, i.e. $L_x \gg L_{y,z}$, we can replace the momentum vectors $\boldsymbol{q}_\pm$ by their x-components, since the zero-modes in y and z will give the largest contribution when summing over $\boldsymbol{q}_\pm$.

The magnetic flux through the ring can be introduced as in Section 2.4.3 by shifting

$$(\boldsymbol{k})_x = \frac{2\pi}{L} n \longrightarrow \frac{2\pi}{L} (n - \varphi) \,,$$

$$(\boldsymbol{k}')_x = \frac{2\pi}{L} n \longrightarrow \frac{2\pi}{L} (n - \varphi') \,, \qquad (4.32)$$

where n is an integer. We get for diffuson and cooperon

$$D(q_-, \omega - \omega') = \frac{\gamma_e}{V\tau_e} \frac{1}{D \frac{4\pi^2}{L^2} (n - \varphi_-)^2 - i(\omega - \omega')/\hbar} = \frac{\gamma_e}{V} \frac{\hbar}{E_C \tau_e} \frac{1}{(n - \varphi_-)^2 - i(\epsilon - \epsilon')} \,,$$

$$C(q_+, \omega - \omega') = \frac{\gamma_e}{V\tau_e} \frac{1}{D \frac{4\pi^2}{L^2} (n - \varphi_+)^2 - i(\omega - \omega')/\hbar} = \frac{\gamma_e}{V} \frac{\hbar}{E_C \tau_e} \frac{1}{(n - \varphi_+)^2 - i(\epsilon - \epsilon')} \,,$$

$$(4.33)$$

where $E_C = \hbar D \frac{4\pi^2}{L^2}$ is the Thouless energy, and we introduced $\varphi_\pm = \varphi \pm \varphi'$ as well as the dimensionless energies $\epsilon = \frac{\omega}{E_C}$. Introducing the Area $A = L^2/4\pi$ of the ring, we get for the current correlation function

$$\langle j_x j_x \rangle = \left(\frac{e E_C}{A\hbar\pi} \right)^2 \int d\epsilon \int d\epsilon' \, n(\epsilon) \, n(\epsilon') \sum_n \left\{ \frac{1}{(n - \varphi_-)^2 - i(\epsilon - \epsilon')} - \frac{1}{(n - \varphi_+)^2 - i(\epsilon - \epsilon')} \right.$$

$$\left. - 2 \left[\frac{(n - \varphi_-)^2}{((n - \varphi_-)^2 - i(\epsilon - \epsilon'))^2} - \frac{(n - \varphi_+)^2}{((n - \varphi_+)^2 - i(\epsilon - \epsilon'))^2} \right] \right\} \qquad (4.34)$$

37

Performing a Poisson summation yields

$$\langle j_x j_x \rangle = \left(\frac{eE_C}{A\hbar\pi}\right)^2 \int d\epsilon \int d\epsilon'\, n(\epsilon)\, n(\epsilon') \sum_p \int dx\, e^{-2\pi i p x}$$

$$\left\{\frac{1}{x^2 - i(\epsilon - \epsilon')} - \frac{2x^2}{(x^2 - i(\epsilon - \epsilon'))^2}\right\} \left(e^{-2\pi i p \varphi_-} - e^{-2\pi i p \varphi_+}\right)$$

$$= \left(\frac{eE_C}{A\hbar\pi}\right)^2 \int d\epsilon \int d\epsilon'\, n(\epsilon)\, n(\epsilon') \sum_p 4\, \sin(2\pi p \varphi)\, \sin(2\pi p \varphi')$$

$$\int dx\, e^{-2\pi i p x}\, \partial_x \left\{\frac{x}{x^2 - i(\epsilon - \epsilon')}\right\}$$

$$= \left(\frac{2eE_C}{A\hbar\pi}\right)^2 \int d\epsilon \int d\epsilon'\, n(\epsilon)\, n(\epsilon') \sum_p 2\pi i p\, \sin(2\pi p \varphi)\, \sin(2\pi p \varphi')$$

$$\int dx\, e^{-2\pi i p x}\, \frac{x}{x^2 - i(\epsilon - \epsilon')}\,, \tag{4.35}$$

where we integrated by parts in the last step. The x integral yields

$$\int dx\, e^{-2\pi i p x}\, \frac{x}{x^2 - i(\epsilon - \epsilon')} = -\pi i\, e^{2\pi i^{3/2} p \sqrt{\epsilon - \epsilon'}}\,, \tag{4.36}$$

leading to

$$\langle j_x j_x \rangle = 8 \left(\frac{eE_C}{A\hbar\pi}\right)^2 \sum_p p\, \sin(2\pi p \varphi)\, \sin(2\pi p \varphi') \int d\epsilon \int d\epsilon'\, n(\epsilon)\, n(\epsilon')\, e^{2\pi i^{3/2} p \sqrt{\epsilon - \epsilon'}}\,. \tag{4.37}$$

For zero temperature, we can assume the distribution functions to be step-like, $n(\omega, T = 0) = \Theta(-\omega)$, where $\Theta(\omega)$ is the Heaviside function. This turns the expression for the current correlator into

$$\langle j_x j_x \rangle = 8 \left(\frac{eE_C}{A\hbar\pi}\right)^2 \sum_p p\, \sin(2\pi p \varphi)\, \sin(2\pi p \varphi') \int_{-\infty}^0 d\epsilon \int_{-\infty}^0 d\epsilon'\, e^{2\pi i^{3/2} p \sqrt{\epsilon - \epsilon'}}\,. \tag{4.38}$$

Since we have to deal with many integrals of this kind, the integrations over x and the energies are performed in Appendix A.2. Inserting the result given there, we get

$$\langle j_x j_x \rangle = \frac{6E_C^2 e^2}{\hbar^2 \pi^6 A^2} \sum_{p>0} \frac{\sin(2\pi p \varphi)\sin(2\pi p \varphi')}{p^3} = 4\,\frac{6E_C^2}{\pi^4 \phi_0^2 A^2} \sum_{p>0} \frac{\sin(2\pi p \varphi)\sin(2\pi p \varphi')}{p^3}\,, \tag{4.39}$$

where we introduced the flux quantum. So far we calculated the current density fluctuations. To get the current fluctuations we have to multiply with the area squared. We get

$$\langle I_x I_x \rangle = 4\,\frac{6E_C^2}{\pi^4 \phi_0^2} \sum_{p>0} \frac{\sin(2\pi p \varphi)\sin(2\pi p \varphi')}{p^3}\,. \tag{4.40}$$

This result coincides with the one calculated in Section 2.4.3 and reference [5].

4.3 Current fluctuations in fourth order in the field

In this section we want to calculate the current-current correlation function to lowest order in the field. It turns out that under the assumption that the microwave field stands perpendicular to the ring, the lowest order corrections to the equilibrium persistent current correlation function will be of fourth order in the field. Anticipating this result we will begin with the derivation of the current in second order in the field in Section 4.3.1 which provides the lowest order correction to the DC current and derive expressions for the fourth-order corrections to the correlation function in Section 4.3.2. The extinction of the second order terms as well as other possible contributions like the diamagnetic term (cf. [35]) will be discussed in Section 4.3.3.

Throughout this section we will assume the system to be in the diffusive limit, which means that we assume the mean free path and time to be the smallest quantities in the system, implying $\nu\tau_e \ll 1$, ν the frequency of the microwave field. Further we assume that an electron interacts at most once with the field between two scattering events. This can be accounted for by assuming the the classical potential drop eEl_e between two scattering centers is much smaller than the energy $\hbar\nu$ transferred by a quantum mechanical electron-field interaction.

4.3.1 Current in second order in the field

The current in second order in the field can be written in real space as [19]

$$j_2(1) = -\frac{e\hbar}{2m} \left(\nabla_1 - \nabla_{1'} \right) G_2^<(1,1') \big|_{1=1'} \,, \tag{4.41}$$

where the variable 1 stands for $(\boldsymbol{r}_1, t_1)$, and $G_2^<$ is the lesser Green function expanded to second order in the field. Again we can write the lesser Green function as a trace over the matrix Green function

$$\underline{G} = \begin{pmatrix} G^R & G^K \\ 0 & G^A \end{pmatrix} . \tag{4.42}$$

We get by expanding Eq. (4.19) one order further

$$G_2^<(1,1') = \left(\frac{ie}{2m} \right)^2 \mathrm{tr} \bigg\{ (\tau_1 - \tau_3) \int d2\, \boldsymbol{A}(2) \cdot (\nabla_2 - \nabla_{2'}) \int d3\, \boldsymbol{A}(3) \cdot (\nabla_3 - \nabla_{3'})$$
$$\underline{G}_0(1,2')\, \underline{G}_0(2,3')\, \underline{G}_0(3,1') \bigg|_{2=2',3=3'} \bigg\}, \tag{4.43}$$

which turns the current into

$$j_2(1) = \frac{e^3\hbar}{8m^3} \left(\nabla_1 - \nabla_{1'} \right) \mathrm{tr} \bigg\{ (\tau_1 - \tau_3) \int d2\, \boldsymbol{A}(2) \cdot (\nabla_2 - \nabla_{2'}) \int d3\, \boldsymbol{A}(3) \cdot (\nabla_3 - \nabla_{3'})$$
$$\underline{G}_0(1,2')\, \underline{G}_0(2,3')\, \underline{G}_0(3,1') \bigg|_{2=2',3=3'} \bigg\} \bigg|_{1=1'} . \tag{4.44}$$

39

Before performing the trace, we Fourier transform to $(\boldsymbol{k}, \omega)$-space. We assume the vector potential to have the form

$$\boldsymbol{A}(t) = \boldsymbol{A}(e^{i\nu t} + e^{-i\nu t}), \qquad (4.45)$$

where $\boldsymbol{A}$ is a constant vector perpendicular to the ring, i.e. $\boldsymbol{A} = A\,\hat{e}_z$. We get for the current in second order in the field

$$
\begin{aligned}
j_2(1) = \frac{e^3\hbar}{8m^3}\,(\nabla_1 - \nabla_{1'})\mathrm{tr}\bigg\{ &(\tau_1 - \tau_3)\int dx_2 dt_2\,\boldsymbol{A}(e^{i\nu t_2} + e^{-i\nu t_2})\cdot(\nabla_{x_2} - \nabla_{x_2'}) \\
&\int dx_3 dt_3\,\boldsymbol{A}(e^{i\nu t_3} + e^{-i\nu t_3})\cdot(\nabla_{x_3} - \nabla_{x_3'})\frac{1}{V^3}\sum_{k_i,k_i'} e^{i(k_1 x_1 - k_2' x_2' + k_2 x_2 - k_3' x_3' + k_3 x_3 - k_1' x_1')} \\
&\int \frac{d\omega_1}{2\pi}\int\frac{d\omega_2}{2\pi}\int\frac{d\omega_3}{2\pi}\,e^{-i\omega_1(t_1 - t_2') - i\omega_2(t_2 - t_3') - i\omega_3(t_3 - t_1')} \\
&\underline{G}_0(k_1, k_2', \omega_1)\,\underline{G}_0(k_2, k_3', \omega_2)\,\underline{G}_0(k_3, k_1', \omega_3)\bigg\}_{2=2',3=3',}\bigg|_{1=1'}.
\end{aligned}
\qquad (4.46)
$$

Performing the spatial derivatives gives

$$
\begin{aligned}
j_2(1) = \frac{e^3\hbar}{8m^3}\frac{1}{V^3}\sum_{k_i,k_i'} i(\boldsymbol{k}_1 + \boldsymbol{k}_1')\,\mathrm{tr}\bigg\{ &(\tau_1 - \tau_3)\int dx_2 dt_2\,\boldsymbol{A}(e^{i\nu t_2} + e^{-i\nu t_2})\cdot i(\boldsymbol{k}_2 + \boldsymbol{k}_2') \\
&\int dx_3 dt_3\,\boldsymbol{A}(e^{i\nu t_3} + e^{-i\nu t_3})\cdot i(\boldsymbol{k}_3 + \boldsymbol{k}_3')\,e^{i(k_1 x_1 - k_2' x_2' + k_2 x_2 - k_3' x_3' + k_3 x_3 - k_1' x_1')} \\
&\int\frac{d\omega_1}{2\pi}\int\frac{d\omega_2}{2\pi}\int\frac{d\omega_3}{2\pi}\,e^{-i\omega_1(t_1 - t_2') - i\omega_2(t_2 - t_3') - i\omega_3(t_3 - t_1')} \\
&\underline{G}_0(k_1, k_2', \omega_1)\,\underline{G}_0(k_2, k_3', \omega_2)\,\underline{G}_0(k_3, k_1', \omega_3)\bigg\}_{2=2',3=3',}\bigg|_{1=1'}.
\end{aligned}
\qquad (4.47)
$$

Now we can perform the integrals over $\boldsymbol{x}_2, t_2, \boldsymbol{x}_3, t_3$

$$
\begin{aligned}
j_2(1) = \frac{e^3\hbar}{8m^3}\frac{1}{V}\sum_{k_i,k_i'} i(\boldsymbol{k}_1 + \boldsymbol{k}_1')\,\mathrm{tr}\bigg\{ &(\tau_1 - \tau_3)\,\boldsymbol{A}\cdot i(\boldsymbol{k}_2 + \boldsymbol{k}_2)\,\boldsymbol{A}\cdot i(\boldsymbol{k}_3 + \boldsymbol{k}_3)\,e^{ix_1(k_1 - k_1')} \\
&\int\frac{d\omega_1}{2\pi}\int d\omega_2\int d\omega_3\,\delta(\omega_1 - \omega_2 \pm \nu)\,\delta(\omega_2 - \omega_3 \pm \nu)\,e^{it_1(\omega_3 - \omega_1)} \\
&\underline{G}_0(k_1, k_2, \omega_1)\,\underline{G}_0(k_2, k_3, \omega_2)\,\underline{G}_0(k_3, k_1', \omega_3)\bigg\}\bigg|_{1=1'}
\end{aligned}
\qquad (4.48)
$$

and integrate over ω_2 and ω_3, leading to

$$
\begin{aligned}
j_2(1) = \frac{e^3\hbar}{8m^3}\frac{1}{V}\sum_{k_i,k_i'} i(\boldsymbol{k}_1 + \boldsymbol{k}_1')\,\mathrm{tr}\bigg\{ &(\tau_1 - \tau_3)\,\boldsymbol{A}\cdot 2i\boldsymbol{k}_2\,\boldsymbol{A}\cdot 2i\boldsymbol{k}_3\,e^{ix_1(k_1 - k_1')} \\
&\int\frac{d\omega_1}{2\pi}\,e^{it_1(\pm\nu\pm\nu)}\,\underline{G}_0(k_1, k_2, \omega_1)\,\underline{G}_0(k_2, k_3, \omega_2)\,\underline{G}_0(k_3, k_1', \omega_3)\bigg\}\bigg|_{1=1'}.
\end{aligned}
\qquad (4.49)
$$

Since we are interested in the time-independent components of the current only, we can select those terms, where $e^{it_1(\pm\nu\pm\nu)} \equiv 1$, and arrive at

$$j_2(1) = \frac{e^3\hbar}{8m^3}\frac{1}{V}\sum_{\pm}\sum_{k_i,k_i'} i(\boldsymbol{k}_1 + \boldsymbol{k}_1')\,\text{tr}\bigg\{(\tau_1 - \tau_3)\,\boldsymbol{A}\cdot 2i\boldsymbol{k}_2\,\boldsymbol{A}\cdot 2i\boldsymbol{k}_3\,e^{ix_1(k_1-k_1'))}$$

$$\int \frac{d\omega_1}{2\pi}\,\underline{G}_0(k_1,k_2,\omega_1)\,\underline{G}_0(k_2,k_3,\omega_1 \pm \nu)\,\underline{G}_0(k_3,k_1',\omega_1)\bigg\}\bigg|_{1=1'}. \tag{4.50}$$

The next step is to expand the trace over the third power of the matrix Green functions. We get

$$\text{tr}(\tau_1 - \tau_3)\underline{G}_0(k_1,k_2,\omega_1)\,\underline{G}_0(k_2,k_3,\omega_2)\,\underline{G}_0(k_3,k_1',\omega_3)$$

$$= \text{tr}(\tau_1 - \tau_3)\begin{pmatrix} R_1R_2R_3 & R_1R_2K_3 + R_1K_2A_3 + K_1A_2A_3 \\ 0 & A_1A_2A_3 \end{pmatrix}$$

$$= -R_1R_2R_3 + R_1R_2K_3 + R_1K_2A_3 + K_1A_2A_3 + A_1A_2A_3\,, \tag{4.51}$$

where we used the abbreviations

$$(R/K/A)_1 \equiv G^{R/K/A}(k_1,k_2,\omega_1)$$
$$(R/K/A)_2 \equiv G^{R/K/A}(k_2,k_3,\omega_1 \pm \nu)$$
$$(R/K/A)_3 \equiv G^{R/K/A}(k_3,k_1',\omega_1)\,. \tag{4.52}$$

The main assumption in the calculation, which will be discussed intensively in Section 4.4, is that the Keldysh Green functions will stay in their equilibrium form

$$G^K(\boldsymbol{k}_1,\boldsymbol{k}_2,\omega) = ((1 - 2n(\omega))\left((G^R(\boldsymbol{k}_1,\boldsymbol{k}_2,\omega) - G^A(\boldsymbol{k}_1,\boldsymbol{k}_2,\omega)\right)\,, \tag{4.53}$$

where $n(\omega)$ is the distribution function. Inserting this in Eq. (4.51) turns the expression for the current in second order in the field (Eq. (4.50)) into

$$j_2(1) = -2i\frac{e^2\hbar}{m^3}\sum_{\pm}\sum_{k_i,k_1'}\boldsymbol{k}_1\,(\boldsymbol{A}\cdot\boldsymbol{k}_2)\,(\boldsymbol{A}\cdot\boldsymbol{k}_3)\int\frac{d\omega}{2\pi}$$

$$\bigg\{G^A(\boldsymbol{k}_1,\boldsymbol{k}_2,\omega)\,G^A(\boldsymbol{k}_2,\boldsymbol{k}_3,\omega\pm\nu)\,G^A(\boldsymbol{k}_3,\boldsymbol{k}_1,\omega)\,n(\omega)$$

$$- G^R(\boldsymbol{k}_1,\boldsymbol{k}_2,\omega)\,G^R(\boldsymbol{k}_2,\boldsymbol{k}_3,\omega\pm\nu)\,G^R(\boldsymbol{k}_3,\boldsymbol{k}_1,\omega)\,n(\omega)$$

$$G^R(\boldsymbol{k}_1,\boldsymbol{k}_2,\omega)\,G^R(\boldsymbol{k}_2,\boldsymbol{k}_3,\omega\pm\nu)\,G^A(\boldsymbol{k}_3,\boldsymbol{k}_1,\omega)\,[n(\omega) - n(\omega\pm\nu)]$$

$$+ G^R(\boldsymbol{k}_1,\boldsymbol{k}_2,\omega)\,G^A(\boldsymbol{k}_2,\boldsymbol{k}_3,\omega\pm\nu)\,G^A(\boldsymbol{k}_3,\boldsymbol{k}_1,\omega)\,[n(\omega\pm\nu) - n(\omega)]\bigg\}. \tag{4.54}$$

These four different contributions to the current can be represented by diagrams which are shown in Figure 4.5.
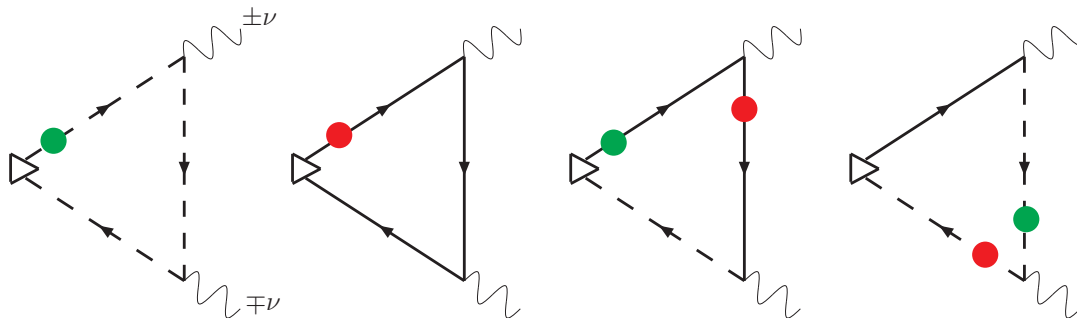
Figure 4.5: Diagrams for the current in second order in the field. The solid (dashed) lines stand for retarded (advanced) Green functions, the little triangles for current vertices, the wiggles for interactions with the field and the dots indicate distribution functions. The red dots indicate, that the distribution function comes with a minus sign.

4.3.2 Current fluctuations

The diagrams for the current fluctuations can be constructed by drawing impurity lines in all possible topologically distinct ways between two of the diagrams in Figure 4.5. Again (as in chapter 2.4.3) those diagrams account for the largest contributions in which one retarded and one advanced Green function are respectively connected by non- or maximally crossed diagrams. Since we want to calculate the current fluctuations along the ring, i.e. $\langle j_x j_x \rangle$, and the field is assumed to be perpendicular to the ring, we only have to account for those diagrams in which the interactions with the field come in pairs in the inner and outer triangle[1].

One can see, that there are two different types of diagrams: Either one can pair diagrams of the first and second kind in Figure 4.5, where one has two distribution functions and can draw diffuson and cooperon diagrams, or one can connect diagrams of the third and fourth kind in figure 4.5. Here we can only draw diffuson contributions, and the resulting diagrams are similar to those in Ref. [6]. We start by calculating the first kind of diagrams.

RRR/AAA diagrams

This diagrams look similar to those calculated in Section 4.2, but now containing two pairs of field-interactions, and are shown in Figure 4.6. On top of the diagrams in Figure 4.6 we also have to consider those diagrams where the current vertices are not at the same point. They correspond to the lower ones in Figure 4.4 for the equilibrium case and are shown in Figure 4.7. The first step in the calculation of these diagrams is to calculate the so called Hikami boxes [36] which are indicated by calligraphic $\mathcal{H}_i$ in the figures. Since the diffusons and cooperons can be assumed to be long ranged in real space, the momenta on the retarded or advanced path should be equal (diffuson) or equal up to the sign (cooperon).

---

[1]This point is manifested in Appendix A.3 where we calculate the Hikami boxes. The vanishing of the Hikami boxes containing only one field-interaction is also the reason for the extinction of the second order diagrams, see Section 4.3.3.
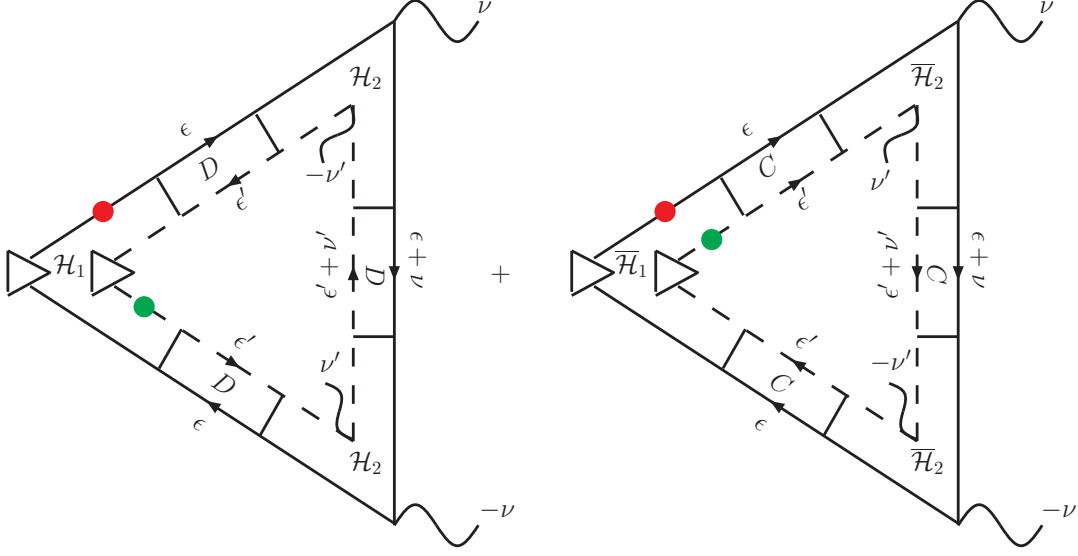
Figure 4.6: Diagrams for RRR/AAA-like terms of the current fluctuations. The nomenclature is the same as in Figure 4.5. The boxes connecting the two current triangles are diffusons (D) or cooperons (C). $\mathcal{H}_i$ stands for a Hikami box.

Thus we can expand the remaining Green functions at one point in the diagrams (the Hikami boxes) up to lowest order in the momenta which is equivalent to assuming that the Hikami boxes are short ranged in momentum space. This expansion is performed in Appendix A.3, yielding

$$
\begin{aligned}
\mathcal{H}_1 &= -\left(\frac{e\hbar}{\pi}\right)^2 \frac{v_F^2}{d}\, \delta_{\alpha,\beta}\, \frac{2\tau_e^2}{\gamma_e}\,, \\
\mathcal{H}_2 &= -\left(\frac{e\hbar}{\pi}\right)^2 \left(\frac{E}{\hbar\nu}\right)^2 \frac{v_F^2}{d}\, \frac{2\tau_e^2}{\gamma_e}\,, \\
\mathcal{H}_3^a &= i\,\frac{e\hbar}{\pi}\, \frac{v_F^2}{d}\, \frac{2\tau_e^2}{\gamma_e}\, (\boldsymbol{k} - \boldsymbol{k}')\,, \\
\mathcal{H}_3^b &= -i\,\frac{e\hbar}{\pi}\, \frac{v_F^2}{d}\, \frac{2\tau_e^2}{\gamma_e}\, (\boldsymbol{k} - \boldsymbol{k}')
\end{aligned}
\tag{4.55}
$$

for the diffuson Hikami boxes, and

$$
\begin{aligned}
\overline{\mathcal{H}}_1 &= \left(\frac{e\hbar}{\pi}\right)^2 \frac{1}{V} \sum_{\boldsymbol{k}} v_\alpha\, v_\beta\, G^R(\boldsymbol{k},\epsilon)^2\, G^A(\boldsymbol{k}',\epsilon')^2 = \left(\frac{e\hbar}{\pi}\right)^2 \frac{v_F^2}{d}\, \delta_{\alpha,\beta}\, \frac{2\tau_e^2}{\gamma_e}\,, \\
\overline{\mathcal{H}}_2 &= \left(\frac{e\hbar}{\pi}\right)^2 \left(\frac{E}{\hbar\nu}\right)^2 \frac{v_F^2}{d}\, \frac{2\tau_e^2}{\gamma_e}\,, \\
\overline{\mathcal{H}}_3^a &= \overline{\mathcal{H}}_3^b = i\,\frac{e\hbar}{\pi}\, \frac{v_F^2}{d}\, \frac{2\tau_e^2}{\gamma_e}\, (\boldsymbol{k} + \boldsymbol{k}')
\end{aligned}
\tag{4.56}
$$
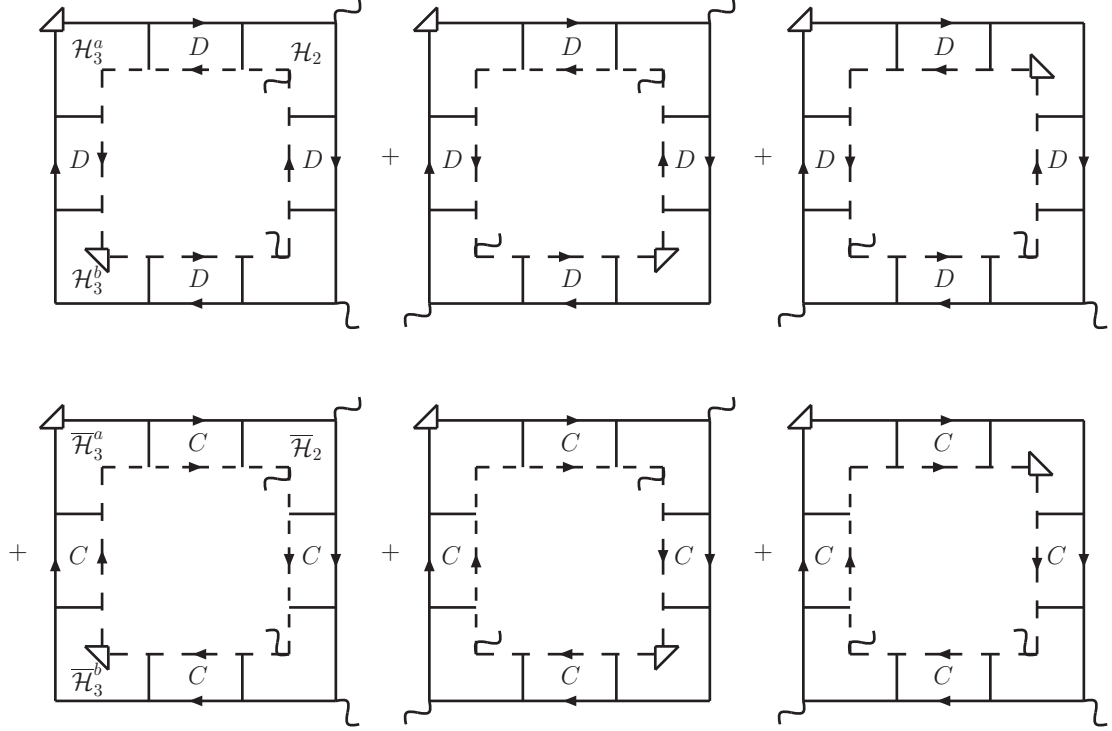
Figure 4.7: The diagrams for RRR/AAA-like terms of the current fluctuations corresponding to the lower equilibrium diagrams in Figure 4.4.

for the cooperon Hikami boxes.

Collecting the contributions from the diagrams we get for the diffuson part of the current fluctuations in x-direction (along the ring)

$$\langle j_x j_x \rangle_{\text{Diff}} = 8\, e^6\, \frac{E^4}{(\hbar\nu)^4} V \sum_{\nu,\nu'} \sum_{q_-} \int \frac{d\omega}{2\pi} \int \frac{d\omega'}{2\pi}\, n(\omega)\, n(\omega') \left(\frac{D}{\gamma}\, 2\tau_e \right)^3$$

$$\text{Re}\bigg\{ D(q_-, \omega - \omega')^2 D(q_-, \omega \pm \nu - \omega' \mp \nu') -$$

$$2\frac{D}{\gamma}\, \tau_e\, V q_-^2 \left[2D(q_-, \omega - \omega')^3 D(q_-, \omega \pm \nu - \omega' \mp \nu') \right.$$

$$\left. + D(q_-, \omega \pm \nu - \omega')^2 D(q_-, \omega - \omega' \mp \nu')^2 \right] \bigg\}. \tag{4.57}$$

44

Shifting $\omega \to \omega \mp \nu$ and the $\nu \to \nu'$ in the last term, we get

$$\langle j_x j_x \rangle_{\text{Diff}} = 8\,e^6 \frac{E^4}{(\hbar\nu)^4} V \sum_{\nu,\nu'} \sum_{q_-} \int \frac{d\omega}{2\pi} \int \frac{d\omega'}{2\pi} \left(\frac{D}{\gamma} 2\tau_e\right)^3$$

$$\text{Re}\Big\{ D(q_-, \omega - \omega')^2 D(q_-, \omega \pm \nu - \omega' \mp \nu')\, n(\omega)\, n(\omega') -$$

$$2\frac{D}{\gamma}\tau_e\, V q_-^2 \left[2D(q_-, \omega - \omega')^3 D(q_-, \omega \pm \nu - \omega' \mp \nu')\, n(\omega)\, n(\omega') \right.$$

$$\left. + D(q_-, \omega \pm \nu - \omega')^2 D(q_-, \omega - \omega' \mp \nu')^2 \left(n(\omega \pm \nu) - n(\omega) \right) n(\omega') \right] \Big\}. \quad (4.58)$$

The unperturbed diffusons are given by

$$D(\boldsymbol{q}, \omega) = \frac{\gamma}{V\tau_e} \left[D\,\boldsymbol{q}^2 + \tau_{\text{in}}^{-1} - i\omega/\hbar \right]^{-1}, \quad (4.59)$$

where we introduced the inelastic scattering time τ_{in} [37]. Assuming that the ring is slim, i.e. $L_x \gg L_{y,z}$, we can concentrate on the summation over the modes in x-direction and replace expression (4.59) by

$$D(q_-, \epsilon = \omega/E_C) = \frac{\gamma}{V} \frac{\hbar}{E_C \tau_e} \left(n^2 + \eta - i\epsilon \right)^{-1}, \quad (4.60)$$

$\eta = \hbar \tau_{\text{in}}^{-1}/E_C$ the dimensionless inelastic scattering time. Introducing the flux through the ring which corresponds to replacing the momenta by

$$\boldsymbol{k}_x = \frac{2\pi}{L} n \longrightarrow \frac{2\pi}{L}(n - \varphi) \text{ and}$$

$$\boldsymbol{k}'_x = \frac{2\pi}{L} m \longrightarrow \frac{2\pi}{L}(m - \varphi'), \quad (4.61)$$

we get

$$D(q_- = k_x - k'_x, \epsilon = \omega/E_C) = \frac{\gamma}{V} \frac{\hbar}{E_C \tau_e} \left((n - \varphi_-)^2 + \eta - i\epsilon \right)^{-1}, \quad (4.62)$$

where $\varphi_- = \varphi - \varphi'$. Inserting this into the expression for $\langle j_x j_x \rangle_{\text{Diff}}$ yields

$$
\langle j_x j_x \rangle_{\text{Diff}} = \frac{8e^6}{4\pi^2} \frac{E^4}{(\hbar\nu)^4} \frac{V}{E_C} \sum_{\nu,\nu'} \sum_n \int \frac{d\epsilon}{E_C} \int \frac{d\epsilon'}{E_C} \left(\frac{D}{\gamma} 2\tau_e\right)^3 \left(\frac{\gamma}{V\tau_e}\right)^3 n(\epsilon)\, n(\epsilon')
$$

$$
\text{Re}\Bigg\{ \left[(n-\varphi_-)^2 - i(\epsilon - \epsilon')\right]^{-2} \left[(n-\varphi_-)^2 - i(\epsilon \pm \nu - \epsilon' \mp \nu')\right]^{-1}
$$

$$
- 2(n-\varphi_-)^2 \left(2\left[(n-\varphi_-)^2 - i(\epsilon - \epsilon')\right]^{-3} \left[(n-\varphi_-)^2 - i(\epsilon \pm \nu - \epsilon' \mp \nu')\right]^{-1}\right.
$$

$$
\left.+ \left[(n-\varphi_-)^2 - i(\epsilon - \epsilon')\right]^{-2} \left[(n-\varphi_-)^2 - i(\epsilon \pm \nu - \epsilon' \mp \nu')\right]^{-2}\right)\Bigg\}
$$

$$
- \frac{8e^6}{4\pi^2} \frac{E^4}{(\hbar\nu)^4} V \sum_{\nu,\nu'} \sum_n \int \frac{d\epsilon}{\tau_D} \int \frac{d\epsilon'}{\tau_D} \left(\frac{D}{\gamma} 2\tau_e \frac{\gamma}{V} \frac{\tau_D}{\tau_e}\right)^3 (n(\epsilon \pm \nu) - n(\epsilon))\, n(\epsilon')
$$

$$
\text{Re}\Bigg\{ 2(n-\varphi_-)^2 \left[(n-\varphi_-)^2 - i(\epsilon - \epsilon')\right]^{-2} \left[(n-\varphi_-)^2 - i(\epsilon \pm \nu - \epsilon' \mp \nu')\right]^{-2}\Bigg\},
$$

$$
(4.63)
$$

where we omitted $\eta = \tau_{\text{in}}^{-1}$ to keep the expressions compact.

We see, that the term splits into one part depending just on the distribution function $n(\epsilon)$ and one depending on the difference $(n(\epsilon \pm \nu) - n(\epsilon))$. We start by manipulating the first one. In order to calculate the current current correlation function and not the correlation function of the current density, as we did so far, we have to multiply with the area squared $\left(\frac{L^2}{4\pi}\right)^2$. Further we can simplify the formula by replacing the circumference of the ring by the radius, $L = 2\pi R$, and by introducing the flux quantum $\phi_0 = \frac{h}{e}$. We get

$$
\langle I_x I_x \rangle_{\text{Diff,I}} = \frac{64}{\pi^2} \left(\frac{eER}{\hbar\nu}\right)^4 \left(\frac{E_C}{\phi_0}\right)^2 \sum_{\nu,\nu'} \sum_n \int d\epsilon \int d\epsilon'\, n(\epsilon)\, n(\epsilon')
$$

$$
\text{Re}\Bigg\{ \left[(n-\varphi_-)^2 - i(\epsilon - \epsilon')\right]^{-2} \left[(n-\varphi_-)^2 - i(\epsilon \pm \nu - \epsilon' \mp \nu')\right]^{-1}
$$

$$
- 2(n-\varphi_-)^2 \left(2\left[(n-\varphi_-)^2 - i(\epsilon - \epsilon')\right]^{-3} \left[(n-\varphi_-)^2 - i(\epsilon \pm \nu - \epsilon' \mp \nu')\right]^{-1}\right.
$$

$$
\left.+ \left[(n-\varphi_-)^2 - i(\epsilon - \epsilon')\right]^{-2} \left[(n-\varphi_-)^2 - i(\epsilon \pm \nu - \epsilon' \mp \nu')\right]^{-2}\right)\Bigg\} \qquad (4.64)
$$

Performing a Poisson summation yields

$$\langle I_x I_x \rangle_{\text{Diff,I}} = \frac{64}{\pi^2} \left(\frac{eER}{\hbar\nu} \right)^4 \left(\frac{E_C}{\phi_0} \right)^2 \sum_{\nu,\nu'} \int d\epsilon \int d\epsilon' \, n(\epsilon) \, n(\epsilon')$$

$$\text{Re} \Bigg\{ \sum_p \int dx \, e^{-2\pi i p x} e^{-2\pi i p \varphi_-} \left[x^2 - i(\epsilon - \epsilon') \right]^{-2} \left[x^2 - i(\epsilon \pm \nu - \epsilon' \mp \nu') \right]^{-1}$$

$$- 2x^2 \left(2 \left[x^2 - i(\epsilon - \epsilon') \right]^{-3} \left[x^2 - i(\epsilon \pm \nu - \epsilon' \mp \nu') \right]^{-1} \right.$$

$$+ \left. \left[x^2 - i(\epsilon - \epsilon') \right]^{-2} \left[x^2 - i(\epsilon \pm \nu - \epsilon' \mp \nu') \right]^{-2} \right) \Bigg\}$$

$$= \left(\frac{eER}{\hbar\nu} \right)^4 \left(\frac{8E_C}{\pi\phi_0} \right)^2 \sum_{\nu,\nu'} \int d\epsilon \int d\epsilon' \, n(\epsilon) \, n(\epsilon')$$

$$\text{Re} \Bigg\{ \sum_p e^{-2\pi i p \varphi_-} \int dx \, e^{-2\pi i p x} \partial_x \left(\frac{x}{\left[x^2 - i(\epsilon - \epsilon') \right]^2 \left[x^2 - i(\epsilon \pm \nu - \epsilon' \mp \nu') \right]} \right) \Bigg\}.$$

$$(4.65)$$

The second part in Eq. (4.63) can be written as

$$\langle I_x I_x \rangle_{\text{Diff,I}} = \left(\frac{eER}{\hbar\nu} \right)^4 \left(\frac{8E_C}{\pi\phi_0} \right)^2 \sum_{\nu,\nu'} \int d\epsilon \int d\epsilon' \, (n(\epsilon) - n(\epsilon \pm \nu)) \, (n(\epsilon') - n(\epsilon' \pm \nu'))$$

$$\text{Re} \Bigg\{ \sum_p e^{-2\pi i p \varphi_-} \int dx \, e^{-2\pi i p x} \frac{x^2}{\left[x^2 - i(\epsilon - \epsilon') \right]^2 \left[x^2 - i(\epsilon \pm \nu - \epsilon' \mp \nu') \right]^2} \Bigg\}.$$

$$(4.66)$$

We can get the cooperon terms out of this by replacing φ_- by $\varphi_+ = \varphi + \varphi'$ and adding the relative minus signs coming from the Hikami boxes. Thus, defining $I_0^2 = \left(\frac{eER}{\hbar\nu} \right)^4 \left(\frac{8E_C}{\pi\phi_0} \right)^2$, the full expression for the RRR/AAA diagrams turns into

$$\langle I_x I_x \rangle_{\text{RRR/AAA}} = I_0^2 \sum_{\nu,\nu'=\pm\nu} \int d\epsilon \int d\epsilon' \text{Re} \Bigg\{ \sum_p \left[e^{-2\pi i p \varphi_-} - e^{-2\pi i p \varphi_+} \right] \int dx \, e^{-2\pi i p x}$$

$$\left[\partial_x \frac{x \, n(\epsilon) n(\epsilon')}{\left[x^2 - i(\epsilon - \epsilon') \right]^2 \left[x^2 - i(\epsilon \pm \nu - \epsilon' \mp \nu') \right]} \right.$$

$$\left. - \frac{x^2 \left(n(\epsilon) - n(\epsilon \pm \nu) \right) \left(n(\epsilon') - n(\epsilon' \pm \nu') \right)}{\left[x^2 - i(\epsilon - \epsilon') \right]^2 \left[x^2 - i(\epsilon \pm \nu - \epsilon' \mp \nu') \right]^2} \right] \Bigg\}.$$

$$(4.67)$$

Before we start evaluating the remaining sums and integrals, we will turn to the other possible diagrams for current fluctuations, since it will turn out to be useful to derive a compact expression for the correlation function which we can analyze before performing the calculations.

RRA and RAA Diagrams

The second kind of diagrams for the current fluctuations arise from pairing diagrams three and four in Figure 4.5. In this case it is neither possible to draw cooperon diagrams, nor to
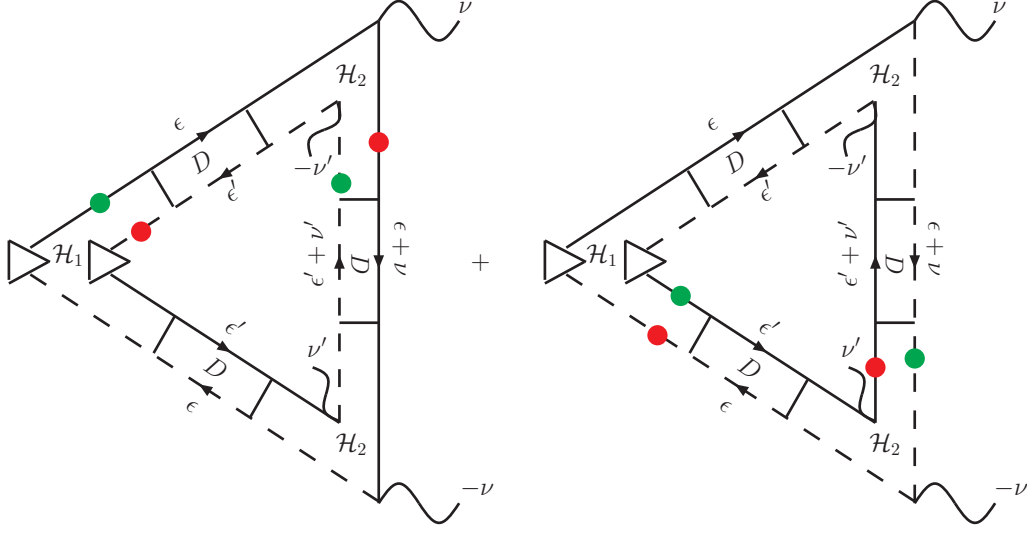
Figure 4.8: Diagrams corresponding to pairs of RRA and RAA diagrams in Figure 4.5. For zero flux these diagrams are similar to those calculated in Ref. [6].

split the current vertices by a diffuson as it is done in Figure 4.7. Thus the only diagrams we can construct are those of Ref. [6], shown in Figure 4.8. Since all Hikami boxes contain already two momenta coming from current vertices or field interactions, the Hikami boxes are the same as in Figure 4.6. Assuming again, that the microwave field points along the z-direction, we get

$$
\begin{aligned}
\langle I_x I_x \rangle_{\text{RRA/RAA}} &= \frac{64}{\pi^2} \left(\frac{eER}{\hbar\nu} \right)^4 \left(\frac{E_C}{\phi_0} \right)^2 \\
&\quad \sum_{\nu,\nu'} \int d\epsilon \int d\epsilon' \left(n(\epsilon) - n(\epsilon \pm \nu) \right) \left((n(\epsilon') - n(\epsilon' \pm \nu')) \right) \\
&\quad \text{Re} \Big\{ \left| \left[(n - \varphi_-)^2 - i(\epsilon - \epsilon') \right] \right|^{-2} \Big(\left[(n - \varphi_-)^2 - i(\epsilon \pm \nu - \epsilon' \mp \nu') \right]^{-1} \\
&\quad + \left[(n - \varphi_-)^2 + i(\epsilon \pm \nu - \epsilon' \mp \nu') \right]^{-1} \Big) \Big\} \\
&= \frac{64}{\pi^2} \left(\frac{eER}{\hbar\nu} \right)^4 \left(\frac{E_C}{\phi_0} \right)^2 \\
&\quad \sum_{\nu,\nu'} \int d\epsilon \int d\epsilon' \left(n(\epsilon) - n(\epsilon \pm \nu) \right) \left((n(\epsilon') - n(\epsilon' \pm \nu')) \right) \text{Re} \Big\{ 2(n - \varphi_-)^2 \\
&\quad \left| \left[(n - \varphi_-)^2 - i(\epsilon - \epsilon') \right] \right|^{-2} \left| \left[(n - \varphi_-)^2 - i(\epsilon - \epsilon' + \nu - \nu') \right] \right|^{-2} \Big\}.
\end{aligned}
$$

(4.68)

Performing a Poisson summation yields

$$
\langle I_x I_x \rangle_{\mathrm{RRA/RAA}} = I_0^2 \sum_{\nu\nu'} \int d\epsilon \int d\epsilon' \, \mathrm{Re}\bigg\{ \sum_p e^{-2\pi i p \varphi_-} \int dx \, e^{-2\pi i p x}
$$
$$
\frac{2(x^2 + \eta)\,(n(\epsilon) - n(\epsilon \pm \nu))\,((n(\epsilon') - n(\epsilon' \pm \nu')))}{|[x^2 + \eta - i(\epsilon - \epsilon')]|^2 \, |[x^2 + \eta - i(\epsilon \pm \nu - \epsilon' \mp \nu')]|^2} \bigg\}, \qquad (4.69)
$$

where we introduced $I_0^2 = \left(\frac{eER}{\hbar\nu}\right)^4 \left(\frac{8E_C}{\pi\phi_0}\right)^2$ again and put back the η-dependence.

Before starting to evaluate the expressions for the current fluctuations we can combine the RRR/AAA and RRA/RAA results into a relatively compact expression. Introducing the dimensionless diffuson operator

$$
D(E) = \frac{1}{x^2 + \eta - i(\epsilon - \epsilon' + E)}, \qquad (4.70)
$$

we get

$$
\langle I_x(\varphi) I_x(\varphi') \rangle = I_0^2 \sum_{\nu,\nu'} \int d\epsilon \int d\epsilon' \, \mathrm{Re}\bigg\{ \sum_p \int dx \, e^{-2\pi i p x}
$$
$$
\bigg(\left[e^{-2\pi i p \varphi_-} - e^{-2\pi i p \varphi_+} \right] \Big[\underbrace{\partial_x \, x D(0)^2 D(\pm\nu \mp \nu')\, n(\epsilon)\, n(\epsilon')}_{\mathrm{Contribution1}}
$$
$$
- \underbrace{x^2 D(0)^2 D(\pm\nu \mp \nu')^2 \, (n(\epsilon) - n(\epsilon \pm \nu)) \, (n(\epsilon') - n(\epsilon' \pm \nu'))}_{\mathrm{Contribution2}} \Big]
$$
$$
+ \underbrace{e^{-2\pi i p \varphi_-} \, 2(x^2 + \eta) \, |D(0)|^2 \, |D(\pm\nu \mp \nu')|^2 \, (n(\epsilon) - n(\epsilon \pm \nu)) \, (n(\epsilon') - n(\epsilon' \pm \nu'))}_{\mathrm{Contribution3}} \bigg),
$$
$$
(4.71)
$$

for the current correlation function. We have already indexed the terms we will treat separately in the following. Exploiting that the underbraced terms in Eq. (4.71) do not depend on the sign of x, we can simplify the expression to

$$
\langle I_x(\varphi) I_x(\varphi') \rangle = I_0^2 \, \mathrm{Re}\bigg\{ \sum_{p>0} 4 \, \sin(2\pi p \varphi) \sin(2\pi p \varphi') \left[\langle II \rangle_{\mathrm{Contr.1}} + \langle II \rangle_{\mathrm{Contr.2}} \right] \bigg\}
$$
$$
+ \langle II \rangle_{\mathrm{Contr.3,p=0}} + \sum_{p>0} 2 \cos(2\pi p (\varphi - \varphi')) \langle II \rangle_{\mathrm{Contr.3}}, \qquad (4.72)
$$

where we abbreviated

$$\langle II \rangle_{\text{Contr.1}} = \sum_{\nu,\nu'=\pm\nu} \int d\epsilon \int d\epsilon' \int dx\, e^{-2\pi i p x} \partial_x\, x D(0)^2 D(\pm\nu \mp \nu')\, n(\epsilon)\, n(\epsilon')\,,$$

$$\langle II \rangle_{\text{Contr.2}} = -\sum_{\nu,\nu'=\pm\nu} \int d\epsilon \int d\epsilon' \int dx\, x^2\, e^{-2\pi i p x} D(0)^2 D(\pm\nu \mp \nu')^2$$

$$\times \left(n(\epsilon) - n(\epsilon \pm \nu)\right)\left(n(\epsilon') - n(\epsilon' \pm \nu')\right)$$

$$\langle II \rangle_{\text{Contr.3}} = \text{Re}\Bigg\{ \sum_{\nu,\nu'=\pm\nu} \int d\epsilon \int d\epsilon' \int dx\, e^{-2\pi i p x}\, 2(x^2 + \eta)\, |D(0)|^2 \left|D(\pm\nu \mp \nu')\right|^2$$

$$\times \left(n(\epsilon) - n(\epsilon \pm \nu)\right)\left(n(\epsilon') - n(\epsilon' \pm \nu')\right)\Bigg\}. \tag{4.73}$$

Thus we have arrived at a quite compact expression for the current-current correlation function. Prior to the evaluation of the remaining integrals, we take this expression (4.72) and discuss the physics behind it as well as expected orders of magnitudes and observability of the effect at this point.

4.3.3   Second order and other terms

As we already mentioned in the beginning of Section 4.3.2, the second order terms for the current fluctuations will vanish. The reason for this is on the one hand that there are no first order DC corrections to the current, and we thus would have to pair a second- and a zeroth order current diagram in order to get second order fluctuations. Furthermore this diagrams would involve Hikami boxes containing only one field-interaction. Those Hikami boxes vanish (as argued in Appendix A.3) due to the angular integration as long as the microwave field stands perpendicular on the ring.

Another contribution to the correlation function in the fourth order of the field comes from the terms proportional to $\boldsymbol{A}^2$ in the kinetic momentum. Introducing a vector potential changes the kinetic part of the Hamiltonian according to

$$\frac{\boldsymbol{p}^2}{2m} \longrightarrow \frac{(\boldsymbol{p} - e\boldsymbol{A})^2}{2m} = \frac{\boldsymbol{p}^2}{2m} - \frac{2\boldsymbol{p}\cdot\boldsymbol{A}}{2m} + \frac{e^2\boldsymbol{A}^2}{2m}\,. \tag{4.74}$$

So far we neglected the $\boldsymbol{A}^2$ term and expanded the second term to second order in the vector potential in Section 4.3.1. The diagrams contributing to the correlation function arising from this terms look similar to the ones in Figures 4.6 and 4.7, but now containing two field interaction on the same loop, each contributing a factor $\frac{e^2\boldsymbol{A}^2}{2m}$. The difference in the diagrams is indicated in Figure 4.9. When calculating the Hikami boxes on the right of Figure 4.9, we see that they are smaller by a factor $\hbar\tau_e^{-1}/mv_F$, i.e. by the quotient scattering rate over Fermi energy which is assumed to be small in the diffusive regime. Thus the terms can be neglected.

Finally the diamagnetic terms $ne^2\boldsymbol{A}/m$ of the current do not contribute to the considered fluctuations in x-direction as long as the microwave field stands perpendicular to the ring.
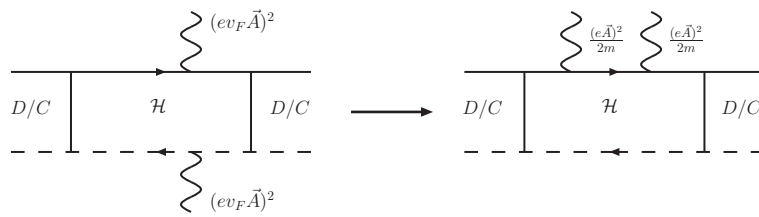
Figure 4.9: Change in the Hikami boxes when calculating the contribution from the $(e\boldsymbol{A})^2$-terms.

4.4 Magnitude and observability of the effect

Before we turn towards the calculation of the terms in equation (4.73) we should comment on the physics behind the terms we derived yet and discuss the magnitudes of the parameters in a real system. The discussion will have an experiment along the lines of Ref. [14] in mind, which is why we use material constants of which can be found in [14] and the respective supporting online material [30].

4.4.1 Fluctuations of the density of states and rectification currents

There is an obvious qualitative difference between the terms arising from the RRR/AAA-diagrams and those from the RRA/RAA-diagrams, manifesting itself in the prefactor of the abbreviations introduced in (4.73): while the first and the second contribution vanish for zero flux, as one could expect for persistent currents which arise from breaking the time reversal symmetry, the third contribution remains still finite. The reason for this behavior it that the terms arise from fundamentally different physical contexts.

The persistent current calculated from the RRR/AAA terms is very similar to the equilibrium persistent current. The difference is a change in the density of states which arises from the perturbation of the microwave field. Thus the physical properties of the first two contributions will also be reminiscent of those of the equilibrium persistent current, including e.g. the vanishing of the contribution when the magnetic flux goes to zero, i.e. the time reversal symmetry is not broken. The third contribution describes a mesoscopic photovoltaic effect in the sample. This effect still exists in the presence of time reversal symmetry, since it relies on local symmetry breaking arising from a random distribution of impurities in the metal. This contribution was already calculated in [6] for linear sample geometries, and indeed one can see that our expression for the RRA/RAA contributions simplifies to the expressions given in Ref. [6] when we set $\varphi - \varphi' = 0$ and subtract the zero-momentum mode which vanishes in [6] due to the boundary conditions in a linear sample.

Experiments measure the dependence of the typical current on the applied magnetic field, which can be described by the current-current correlation function at $\varphi = \varphi'$, rather than the correlation function. On top a smooth background is subtracted from the data, as it it can be seen in [14, figure 1 D/E]. In a measuring procedure like this one would not see the photovoltaic contribution to the typical current, since the corresponding third term in equation (4.72) is constant in the magnetic field when setting $\varphi = \varphi'$. However, a photovoltaic contribution can become important when measuring the dependence of the typical current on the frequency of the applied microwave field while keeping the magnetic field constant. In this scenario the equilibrium persistent current would remain constant and could be subtracted from the signal. Thus, when evaluating equation (4.72), we have to specify which measuring process we have in mind.

4.4.2 Heating effects

The derivation of our expression for the functions above was performed perturbatively in the external field. This approach implicitly assumes that there is an adequate relaxation to stabilize the system. In the studied case the relaxation mechanism is due to phonons

that carry away the energy pumped in the system by the external field. In this section we will describe this relaxation mechanism in a qualitative way in order to estimate the magnitude of the effect later.

The simplest way to accommodate excitation effects is to assume that the phonon relaxation maintains the equilibrium form of the electronic distribution with an effective temperature higher than the lattice temperature. This model is justified when the excitation rate is much smaller than the electron-electron collision rate driving the system towards the equilibrium distribution. The effective electronic temperature can be estimated by requiring balance between excitation and relaxation processes as outlined in this section.

The transitions induced by a harmonic perturbation $H(t) = H' e^{-i\omega t} + H'^\dagger e^{i\omega t}$ can be calculated from the Fermi Golden Rule [38]

$$\Gamma_{i \to f} = 2\pi |\langle f|H'|i\rangle|^2 \delta(E_f - E_i \mp \omega). \tag{4.75}$$

The total energy flux can be obtained from the rate by multiplying by the transition frequency, averaging over the initial states and summing over the final states:

$$
\begin{aligned}
J_E &= 2\pi \sum_{i,f} P_i |\langle f|H'|i\rangle|^2 \omega\, \delta(E_f - E_i - \omega) - 2\pi \sum_{i,f} P_i |\langle f|H'|i\rangle|^2 \omega\, \delta(-(E_f - E_i) - \omega) \\
&= -2\omega \operatorname{Im} \sum_{i,f} P_i \frac{\langle f|H'|i\rangle\langle i|H'|f\rangle}{\omega - E_{fi} + i0^+} + 2\omega \operatorname{Im} \sum_{i,f} P_i \frac{\langle f|H'|i\rangle\langle i|H'|f\rangle}{\omega + E_{fi} + i0^+} \\
&= -2\omega \operatorname{Im} \sum_{i,f} (P_i - P_f) \frac{\langle f|H'|i\rangle\langle i|H'|f\rangle}{\omega - E_{fi} + i0^+}\,,
\end{aligned}
\tag{4.76}
$$

where P_i is the probability of state i (note also that $\operatorname{Im}\left(\frac{1}{x+i0^+}\right) = -\pi\delta(x)$) and $E_{fi} = E_f - E_i$. The two terms on right hand side of the first line correspond to a field-induced absorption ($E_f - E_i = \omega > 0$) and emission ($E_f - E_i = -\omega < 0$). Working in a gauge where the external field enters as a scalar potential the time-dependent perturbation can be written as

$$H(t) = \frac{1}{2} \int dx\, V(x)\rho(x) e^{-i\omega t} + \text{h.c.} \tag{4.77}$$

where $\rho(x) = \psi^\dagger(x)\psi(x)$. Using this expression in Eq. (4.77) the net excitation takes the form

$$J_E = -2\omega \operatorname{Im}\left(\frac{1}{2}\right)^2 \int dx\, dx'\, V(x)V(x') \sum_{i,f} (P_i - P_f) \frac{\langle f|\rho(x)|i\rangle\langle i|\rho(x')|f\rangle}{\omega - E_{fi} + i\eta}\,. \tag{4.78}$$

The last part in the right-hand side containing the summation can be identified as the Lehmann representation of a retarded density-density correlation function $C_{\rho\rho}^r(x,x',t) = -i\Theta(t)\langle[\rho(x,t),\rho(x,0)]_-\rangle$, so the expression can be rewritten as

$$J_E = -\frac{\omega}{2} \int dx\, dx'\, V(x)V(x') \operatorname{Im} C_{\rho\rho}^r(x,x',\omega)\,. \tag{4.79}$$

Now we proceed by writing the density response function in terms of the current response to create a connection to the conductivity. It is straightforward to show that $C^r_{\dot\rho\dot\rho}(x,x',\omega) = \omega^2 C^r_{\rho\rho}(x,x',\omega)$. Making use of the continuity equation $\dot\rho(x) = \nabla \cdot J(x)$, the energy current can be expressed in terms of the current response function as

$$
\begin{aligned}
J_E &= \frac{1}{2\omega} \int dx\, dx'\, V(x)V(x')\operatorname{Im}\partial_\alpha \partial'_\beta C^r_{J^\alpha J^\beta}(x,x',\omega) \\
&= \frac{1}{2} \int dx\, dx'\, \partial_\alpha V(x)\partial'_\beta V(x')\operatorname{Im}\frac{1}{\omega}C^r_{J^\alpha J^\beta}(x,x',\omega)\,.
\end{aligned}
\tag{4.80}
$$

By identifying the usual linear response expression for the conductivity $\operatorname{Im}\frac{1}{\omega}C^r_{J^\alpha J^\beta}(x,x',\omega) = \operatorname{Re}\sigma^{\alpha\beta}(x,x',\omega)$ the energy current finally becomes

$$
J_E = \frac{1}{2} \int dx\, dx'\, \partial_\alpha V(x)\partial'_\beta V(x')\operatorname{Re}\sigma^{\alpha\beta}(x,x',\omega)\,.
\tag{4.81}
$$

When the conductivity can be approximated by an isotropic and local expression $\sigma^{\alpha\beta}(x,x',\omega) = \sigma_0 \delta_{\alpha\beta}\delta(x-x')^2$, we get

$$
\begin{aligned}
J_E &= \frac{1}{2} \int dx \sum_\alpha \partial_\alpha V(x)\partial_\alpha V(x)\operatorname{Re}\sigma_0 \\
&= \frac{\sigma_0}{2} \int dx \sum_\alpha (E_\alpha(x))^2 = \frac{\sigma_0}{4}E_0^2 V\,,
\end{aligned}
\tag{4.82}
$$

where E_0 is the amplitude of the electric field and V is the sample volume. Note that this result has the parametric dependence that is also claimed in [6].

In a steady state, the excitation energy rate by the external field should be compensated by the electron-phonon relaxation. This leads to the requirement

$$
J_E - J_{e-ph} = 0\,.
\tag{4.83}
$$

The electron-phonon energy current in mesoscopic sample is commonly approximated by $J_{e-ph} = \Sigma V(T_e^5 - T_{ph}^5)$, where Σ is an effective electron-phonon coupling and T_e, T_{ph} are electron and lattice temperatures. Condition (4.83) can be then used to estimate the effective electron temperature:

$$
T_e^5 = \frac{\sigma_0 \mathrm{E}_0^2}{4\Sigma} + T_{ph}^5.
\tag{4.84}
$$

Thus the effective electron temperature only depends on material parameters and the lattice temperature. For Al (material used by the Harris group) these parameters are $\Sigma = 2.4 \cdot 10^9 W/m^3 K^5$ and $\sigma_0^{-1} \approx 1.0 \cdot 10^{-8}\Omega m$. Using these numbers it is possible to estimate the effective temperature entering the electron distribution functions.

---

[2]The frequency-dependent conductivity can be approximated by its DC value since we are dealing with frequencies much smaller than the inverse mean-free time τ^{-1}, see also [6].

4.4.3 Magnitude of the parameters in the experiment

In order to estimate the magnitude of the effect and to get realistic values for the parameter regime when evaluating our results we collect some realistic values for the parameters of the system. Therefore we concentrate on the experimental setup of Ref. [14], since the experimental technique used provides the most accurate experimental data to date.

The data are mainly collected from Refs. [14, 23, 30]. The group measures the persistent current of arrays of aluminium rings. The relevant material properties are listed in the following table

Quantity	Symbol	Magnitude
Length	L	$1.2 - 3.1\,\mu m$
Diffusion constant	D	$0.026 \pm 0.01\,m^2/s$
Temperature	T	$\sim 0.2 - 0.6\,K$
Conductivity	σ_0	$1.0 \cdot 10^8\,\Omega m$
Electron-Phonon coupling constant	Σ	$2.4 \cdot 10^9\,W/m^3 K^5$
Fermi velocity	v_F	$2.0 \cdot 10^6\,m/s$.

We will choose $L = 1.2\,\mu m$ in the following. From this data we can calculate the following quantities

Quantity	Symbol	Magnitude
Thouless energy	E_C	$7.5 \cdot 10^{-23}\,J$
Mean free time	τ_e	$\sim 2.0 \cdot 10^{-14}\,s$
Mean free path	l_e	$\sim 3.9 \cdot 10^{-8}\,m$
Characteristic temperature	T_T	$0.87\,K$.

These values allow us to estimate the regions for temperatures, electric field intensities and frequencies which lie within the assumptions of our perturbation theory. First of all we assumed that the mean free time τ_e and mean free path l_e are the smallest quantities in the problem [6]. This implies, that

$$\omega \ll \tau_e^{-1} \approx 5 \cdot 10^{13}\,s^{-1} \tag{4.85}$$

is an upper border for the frequency of the applied field. In choosing the electric field intensity we can follow two different strategies. On the one hand one can apply a weak field in the sense, that the electronic and the phononic temperature are similar. From Eq. (4.84) follows, that field intensities of $E^{\text{weak}} = 0.15\,V/m$ will keep the electronic temperature equal to the phononic temperature up to ten percent. On the other hand the effect of the microwave field will presumably be more pronounced for higher intensities as long as the electronic temperature is of the order of the characteristic temperature. This constraint leads to a field intensity of $E^{\text{strong}} = 6\,V/m$.

The choice of the intensity of the microwave field confines also the frequencies we can analyze without leaving the limits of the perturbative approach. We have assumed

$$\frac{E e l_e}{\hbar \omega} \ll 1 \;\Rightarrow\; \omega \gg \frac{E e l_e}{\hbar} = \begin{cases} \sim 9 \cdot 10^6\,s^{-1} & \text{for } E^{\text{weak}} \\ \sim 4 \cdot 10^8\,s^{-1} & \text{for } E^{\text{strong}} \end{cases} \tag{4.86}$$

which gives us a lower limit for the frequency.

4.4.4 Magnitude of the photovoltaic effect

To get a feeling for the orders of magnitude of the typical current arising from the photovoltaic effect, we can adopt the results of Ref. [6] and insert the parameters of the preceding section. Ref. [6] estimates the photovoltaic current in high frequency case, $\omega \gg EeL/\hbar$, to be of the order

$$I_{\text{typ}}^{\text{PV}} \sim e \left(\frac{\omega}{\tau_D} \right)^{1/2} \left(\frac{EeL}{\hbar\omega} \right)^2 . \tag{4.87}$$

Inserting the parameters and comparing to the equilibrium typical persistent current $\sim e/\tau_D$ shows that we expect the photovoltaic contribution to be six (three) orders of magnitude smaller for a weak (strong) field amplitude. In the low frequency limit we can expect an even smaller signal from the photovoltaic contribution (cf. [6, Eq. 2.8]).

On the other hand we can estimate the magnitude of the effect arising from the field-induced change in the density of states by dividing the prefactor I_0 in Eq. (4.71) by e/τ_D. We can see that the typical current can be of the same order of magnitude as the equilibrium persistent current at low frequencies.

4.5 Evaluation and results

In this section we finally calculate the remaining integrals in Eq. (4.72) and evaluate the results in the parameter region discussed in Section 4.4. Since the evaluation process is similar for the three different contributions defined in Eq. (4.73), we show the calculation for the first term and shift the calculations for the other terms to Appendix A.4.

4.5.1 Evaluation of Contribution 1

Throughout the following calculations we will have to deal with square roots of imaginary units. We will always choose the branch cut of the complex square root to be on the negative real axis, leading to

$$\sqrt{i} = \frac{1+i}{\sqrt{2}}\,,\ \sqrt{-i} = \frac{1-i}{\sqrt{2}} = -i\sqrt{i}\,. \tag{4.88}$$

We start by calculating the integrals of the first contribution. The term reads after integrating by parts

$$\langle II \rangle_{\text{Contr.1}} =$$
$$2\pi i p \sum_{\nu,\nu'=\pm\nu} \int d\epsilon \int d\epsilon' \int dx \, \frac{x \, e^{-2\pi i p x}}{(x^2 + \eta - i(\epsilon - \epsilon'))^2 (x^2 + \eta - i(\epsilon - \epsilon' + \nu - \nu'))} \, n(\epsilon)\, n(\epsilon'). \tag{4.89}$$

We can discriminate between the cases where $\nu = \nu'$ and $\nu = -\nu'$, and start with the latter one.

$\nu = -\nu'$

As a first step we note, that the term in Eq. (4.89) in the case $\nu - \nu' = -2\nu$ is the complex conjugate of the term for $\nu - \nu' = +2\nu$ as one can see by substituting $x \to -x$ and replacing $\epsilon \leftrightarrow \epsilon'$. Thus we can concentrate on the case $\nu - \nu' = 2\nu$ and take twice the real part of the result.

We start by integrating over x. Due to the exponent and since p is larger than zero we can close the integration contour in the lower plane. Defining $a = \sqrt{\eta - i(\epsilon - \epsilon')}$ and $b = \sqrt{\eta - i(\epsilon - \epsilon' + 2\nu)}$ the x-integral turns into

$$\int dx \, \frac{x \, e^{-2\pi i p x}}{(x^2 + \eta - i(\epsilon - \epsilon'))^2 (x^2 + \eta - i(\epsilon - \epsilon' + \nu - \nu'))} = \int dx \, \frac{x \, e^{-2\pi i p x}}{(x^2 + a^2)^2 (x^2 + b^2)}\,, \tag{4.90}$$

where the poles of the integrand lie at $x = \pm ia$ and $x = \pm ib$. Writing

$$ia = i\sqrt{\eta - i(\epsilon - \epsilon')} = \frac{i+1}{\sqrt{2}}\sqrt{\epsilon - \epsilon' + i\eta} \qquad \text{for } \epsilon - \epsilon' > 0 \text{ and}$$

$$ia = \frac{i-1}{\sqrt{2}}\sqrt{-(\epsilon - \epsilon') - i\eta} \qquad\qquad \text{for } \epsilon - \epsilon' < 0 \tag{4.91}$$

we see, that it is always the pole at $x = -ia$ which lies in the lower plane. The same applies for the pole at $x = -ib$ in the cases $\epsilon - \epsilon' > -2\nu$ and $\epsilon - \epsilon' < -2\nu$. Thus we can calculate the integral by adding the residues and get

$$
\int dx\, \frac{x\, e^{-2\pi i p x}}{(x^2 + a^2)^2 (x^2 + b^2)} =
$$
$$
- 2\pi i \left(\mathrm{Res} \left[\frac{x\, e^{-2\pi i p x}}{(x^2 + a^2)^2 (x^2 + b^2)}, x = -ia \right] + \mathrm{Res} \left[\frac{x\, e^{-2\pi i p x}}{(x^2 + a^2)^2 (x^2 + b^2)}, x = -ib \right] \right)
$$
$$
= - \frac{i\pi \left[e^{-2\pi p b} + e^{-2\pi p a} \left(-1 - \pi p a + \frac{\pi p b^2}{a} \right) \right]}{(a^2 - b^2)^2} . \tag{4.92}
$$

Reinserting the terms for a and b we get for the x-integral

$$
\int dx\, \frac{x\, e^{-2\pi i p x}}{(x^2 + \eta - i(\epsilon - \epsilon'))^2 (x^2 + \eta - i(\epsilon - \epsilon' + 2\nu))}
$$
$$
= - \frac{i\pi}{(2\nu)^2} \left[e^{-2\pi p \sqrt{\eta - i(\epsilon - \epsilon' + 2\nu)}} \right.
$$
$$
\left. + e^{-2\pi p \sqrt{\eta - i(\epsilon - \epsilon')}} \left(-1 - \pi p \sqrt{\eta - i(\epsilon - \epsilon')} + \frac{\pi p (\eta - i(\epsilon - \epsilon' + 2\nu))}{\sqrt{\eta - i(\epsilon - \epsilon')}} \right) \right]. \tag{4.93}
$$

Due to the exponential factors in Eq. (4.93) we can close the contour of the remaining integral over ϵ in the upper half, and the contour of the ϵ'-integral in the lower half, encircling only the poles of the Fermi functions[3]. These poles are of first order and lie at $\epsilon = \frac{\pi i}{\beta}(2l + 1)$ and $\epsilon' = \frac{\pi i}{\beta}(2m + 1)$, l, m integers. Since

$$
\lim_{z \to \frac{\pi i}{\beta}(2l+1)} n(z) = -\frac{1}{\beta}, \tag{4.94}
$$

we get for expression (4.89) in the case $\nu + \nu' = \pm 2\nu$

$$
2\mathrm{Re}\left[2\pi i p \int d\epsilon \int d\epsilon' \int dx\, \frac{x\, e^{-2\pi i p x}}{(x^2 - i(\epsilon - \epsilon'))^2 (x^2 - i(\epsilon - \epsilon' + 2\nu))}\, n(\epsilon)\, n(\epsilon') \right]
$$
$$
= \sum_{l,m=0}^{\infty} 2\mathrm{Re}\left[\frac{2p\pi^4\, e^{-2\pi p \left(\sqrt{\frac{2\pi}{\beta}(l+m+1)+\eta} + \sqrt{\frac{2\pi}{\beta}(l+m+1)+\eta-2i\nu} \right)}}{\beta^2 \nu^2 \sqrt{\frac{2\pi}{\beta}(l+m+1)+\eta}} \right.
$$
$$
\left[- e^{2\pi p \sqrt{\frac{2\pi}{\beta}(l+m+1)+\eta}} \sqrt{\frac{2\pi}{\beta}(l+m+1)+\eta} \right.
$$
$$
\left. \left. + e^{2\pi p \sqrt{\frac{2\pi}{\beta}(l+m+1)+\eta-2i\nu}} \left(\sqrt{\frac{2\pi}{\beta}(l+m+1)+\eta} + 2\pi i p \nu \right) \right] \right]. \tag{4.95}
$$

---

[3] The poles on the contour at $\epsilon = \epsilon'$ can be pushed away from the integration area by the small but finite positive inelastic scattering time η.

Note, that since ϵ and ϵ' where dimensionless, also $\beta = \frac{E_C}{k_B T}$ has to be dimensionless in this expression. Replacing $2\pi/\beta \to 2\pi \frac{k_B T}{E_C} = \frac{T}{T_T}$ with $T_T = \frac{2\pi \hbar D}{k_B L^2}$ yields

$$
2\mathrm{Re}\left[-2\pi i p \int d\epsilon \int d\epsilon' \int dx \, \frac{x\, e^{-2\pi i p x}}{(x^2 - i(\epsilon - \epsilon'))^2 (x^2 - i(\epsilon - \epsilon' + 2\nu))} \, n(\epsilon)\, n(\epsilon') \right]
$$

$$
= \sum_{l,m=0}^{\infty} \left(\frac{T}{T_T} \right)^2 \mathrm{Re}\left[\frac{p\pi^2 \, e^{-2\pi p\left(\sqrt{\frac{T}{T_T}(l+m+1)+\eta} + \sqrt{\frac{T}{T_T}(l+m+1)+\eta - 2i\nu} \right)}}{\nu^2 \sqrt{\frac{T}{T_T}(l+m+1) + \eta}} \right.
$$

$$
\left[-e^{2\pi p \sqrt{\frac{T}{T_T}(l+m+1)+\eta}} \sqrt{\frac{T}{T_T}(l+m+1) + \eta} \right.
$$

$$
\left. \left. + e^{2\pi p \sqrt{\frac{T}{T_T}(l+m+1)+\eta - 2i\nu}} \left(\sqrt{\frac{T}{T_T}(l+m+1) + \eta} + 2\pi i p \nu \right) \right] \right]. \qquad (4.96)
$$

$\nu = \nu'$

The $\nu = \nu'$-contribution to Eq. (4.89) takes the form

$$
4\pi i p \int d\epsilon \int d\epsilon' \int dx \, \frac{x\, e^{-2\pi i p x}}{(x^2 + \eta - i(\epsilon - \epsilon'))^3} \, n(\epsilon)\, n(\epsilon') . \qquad (4.97)
$$

We note, that this term is ν independent and start by performing the x-integration. Abbreviating $a = \sqrt{\eta - i(\epsilon - \epsilon')}$, the x-integral reads

$$
\int dx \, \frac{x\, e^{-2\pi i p x}}{(x^2 + \eta - i(\epsilon - \epsilon'))^3} = \int dx \, \frac{x\, e^{-2\pi i p x}}{(x^2 + a^2)^3} . \qquad (4.98)
$$

As before we can close the contour in the lower plane, encircling the pole at $-ia$ clockwise. Thus the integral turns into

$$
\int dx \, \frac{x\, e^{-2\pi i p x}}{(x^2 + a^2)^3} = -2\pi i \, \mathrm{Res}\left[\frac{x\, e^{-2\pi i p x}}{(x^2 + a^2)^3}, x = -ia \right]
$$

$$
= -\frac{i e^{-2\pi p a} \pi^2 p (1 + 2\pi p a)}{4 a^3} . \qquad (4.99)
$$

Reinserting $a = \sqrt{\eta - i(\epsilon - \epsilon')}$ we get

$$
\int dx \, \frac{x\, e^{-2\pi i p x}}{(x^2 + \eta - i(\epsilon - \epsilon'))^3} = -\frac{i p \pi^2 e^{-2\pi p \sqrt{\eta - i(\epsilon - \epsilon')}}}{4(\eta - i(\epsilon - \epsilon'))^3} \left(1 + 2\pi p \sqrt{\eta - i(\epsilon - \epsilon')} \right) . \qquad (4.100)
$$

We see that we can close contour of the remaining integral over ϵ in the upper, and the contour of the integral over ϵ' in the lower half again, encircling only the poles of the Fermi
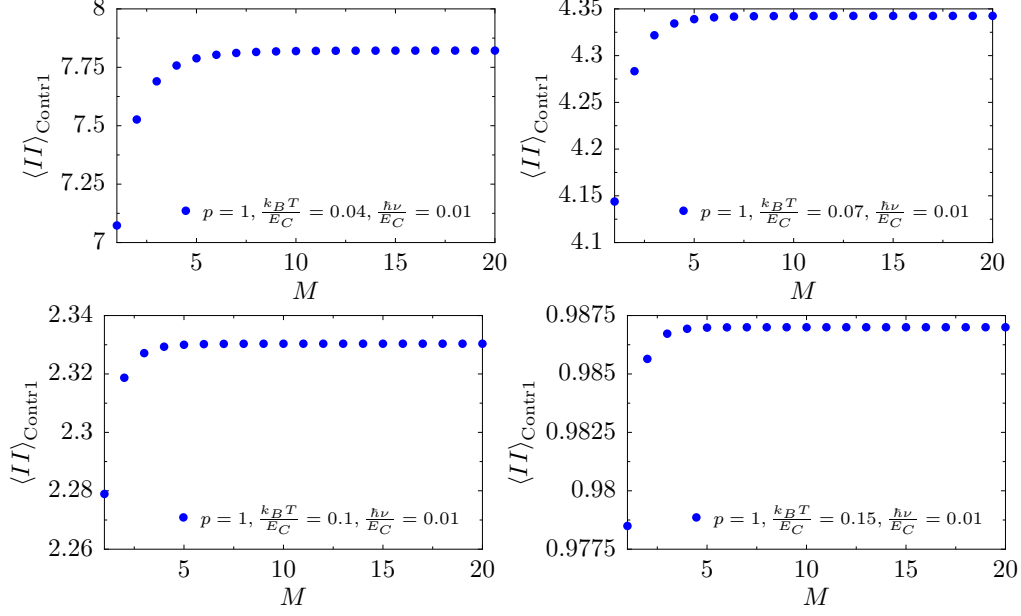
Figure 4.10: Convergence of the first contribution for the sum over the Fermi poles for different temperatures in the case $\eta \to 0$.

function. Following the same steps as for the case $\nu + \nu' = 2\nu$ we get

$$
4\pi i p \int d\epsilon \int d\epsilon' \int dx \, \frac{x \, e^{-2\pi i p x}}{(x^2 - i(\epsilon - \epsilon'))^3} \, n(\epsilon) \, n(\epsilon')
$$

$$
= \sum_{l,m=0}^{\infty} \frac{4p^2\pi^5 e^{-2\pi p\sqrt{\frac{2\pi}{\beta}(l+m+1)+\eta}}}{\beta^2 \left(\frac{2\pi}{\beta}(l+m+1)+\eta\right)^{3/2}} \left(1 + 2\pi p\sqrt{\frac{2\pi}{\beta}(m+l+1)+\eta}\right)
$$

$$
= \sum_{l,m=0}^{\infty} \left(\frac{T}{T_T}\right)^2 \frac{p^2\pi^3 e^{-2\pi p\sqrt{\frac{T}{T_T}(l+m+1)+\eta}}}{\left(\frac{T}{T_T}(l+m+1)+\eta\right)^{3/2}} \left(1 + 2\pi p\sqrt{\frac{T}{T_T}(m+l+1)+\eta}\right), \quad (4.101)
$$

where we replaced $2\pi/\beta \to T/T_T$ again.

Evaluation of contribution 1

For the evaluation we will use the experimentally relevant dimensionless parameters derived in Section 4.4. Since we will evaluate the remaining sums over the Fermi poles numerically, the first step is to examine the convergence of the two contributions for large l and m. In Figure 4.10 we plot the two contributions for different parameters summing l and m from 0 to M. We see, as one can expect, that we have to sum over more and more Fermi poles when the temperature becomes higher, and that we can expect the result to converge sufficiently within the temperature range we are interested in if we choose $M = 20$.
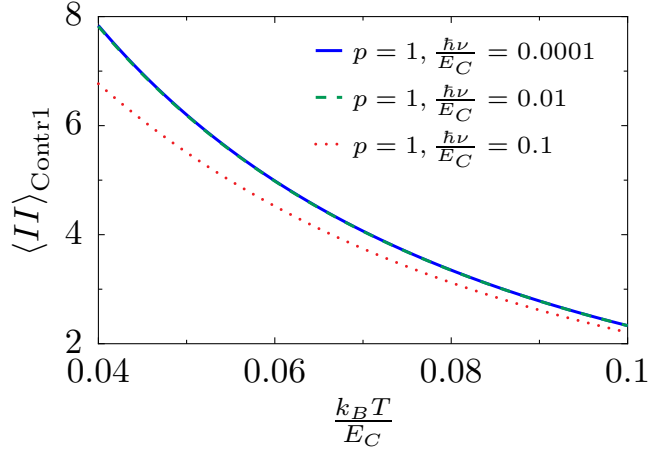
Figure 4.11: Temperature dependence of contribution one for different values of the frequency in the case $\eta \to 0$.

Temperature dependence We evaluate the temperature dependence of the first contribution by replacing $\beta \to E_C/k_B T$. The result is plotted in Figure 4.11 for different values of the frequency, where one can see the expected we exponential damping of the components.

ν-dependence Since the contribution in the case $\nu - \nu' = 0$ is ν-independent, we plot the two cases independently for different parameters in Figure 4.12. The ν-dependent term is equal to the ν-independent term at $\nu \ll 1$ and damped for high frequencies.

Contributions two and three The calculation of the other two contributions resembles the calculation of the first contribution and is shown in Appendix A.4. We show the frequency depencies of the two contributions in Fig. 4.13. It turns out that due to the difference of the Fermi functions both contributions are damped for low frequencies – the regime favoured by the prefactor which will be included in the following section.

4.5.2 Results

When evaluating the calculations we have performed we will have different experimental strategies in mind. Since a subtraction of a constant background signal from the raw data is always possible, we have to identify the signal which changes with the respective parameters varied in the experiment. First we will evaluate the influence of the additional microwave field on the experiment on the typical current in [14] where the magnetic field and thus the flux ($\varphi - \varphi'$ in Eq. (4.72)) is changed. After this we will look at the dependence of the signal on the frequency of the microwave field. Since the equilibrium persistent current as well as some parts of the correlation function in Eq. (4.72) are not frequency dependent we can subtract their constant signal. Finally we will comment on the results one can achieve when evaluating the current-current correlation function from the experimental data.
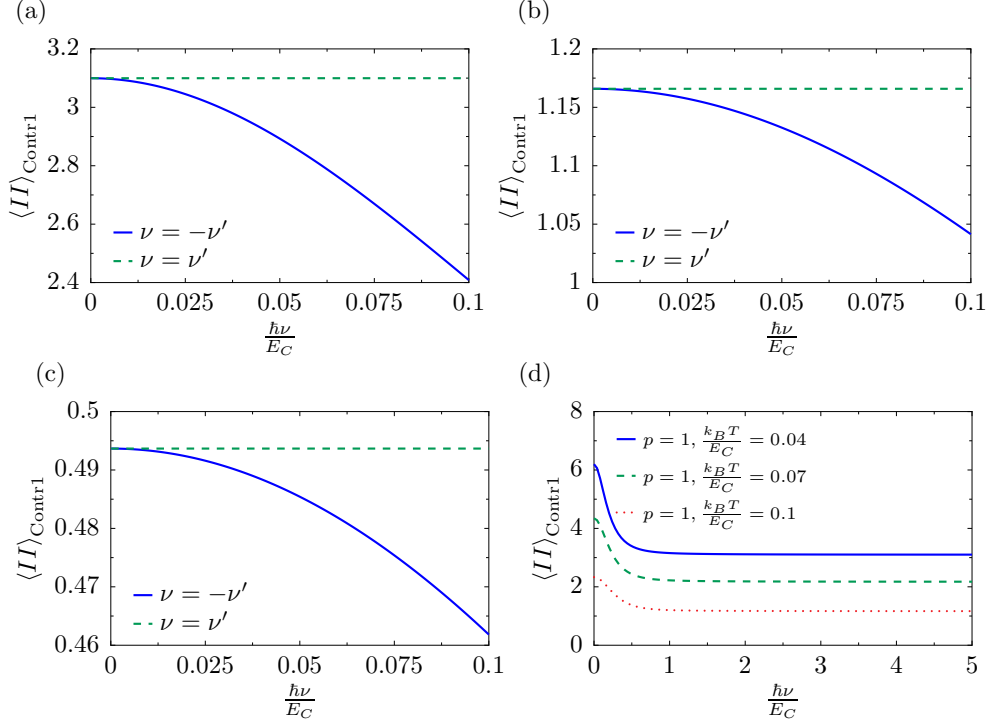
Figure 4.12: Frequency dependence of contribution one in the case $\eta \to 0$ for different temperatures. (a)-(c) show the $\nu = \nu'$ and $\nu = -\nu'$ contributions for $p = 1$ separately for different temperatures $\frac{k_B T}{E_C} = 0.05$ (a), 0.1 (b), 0.15 (c). In (d) the sum of both contributions is plotted for a wider frequency range.

Variation of the magnetic field

By varying the magnetic field one can receive the correlation function at $\varphi = \varphi'$ from the data. As already mentioned in Section 4.4.1 in this case the third contribution which has its physical origin in rectification effects [6] will be constant and can be subtracted from the raw data. Thus we are left with the equilibrium persistent current and with contributions one and two from Eq. (4.72). Note that switching off the electric field during the experiment will not only result in disappearance of the additional contribution we calculated, but also in a lower electron temperature (Eq. (4.84)) leading to a larger equilibrium persistent current. Thus for measuring the effect of an additional microwave field just by switching the field on and off one would need a better picture of the influence of the field on the distribution function than the qualitative dependence we derived in Section 4.4.2 (cf. the comments in Section 5.1).

Subtracting the constant terms, Eq. (4.72) simplifies to

$$\langle I_x(\varphi) I_x(\varphi) \rangle = \left(\frac{eER}{\hbar\nu} \right)^4 \left(\frac{8E_C}{\pi\phi_0} \right)^2 \text{Re}\left\{ \sum_{p>0} 4 \sin^2(2\pi p\varphi) \left[\langle II \rangle_{\text{Contr.1}} + \langle II \rangle_{\text{Contr.2}} \right] \right\}.$$

$$(4.102)$$
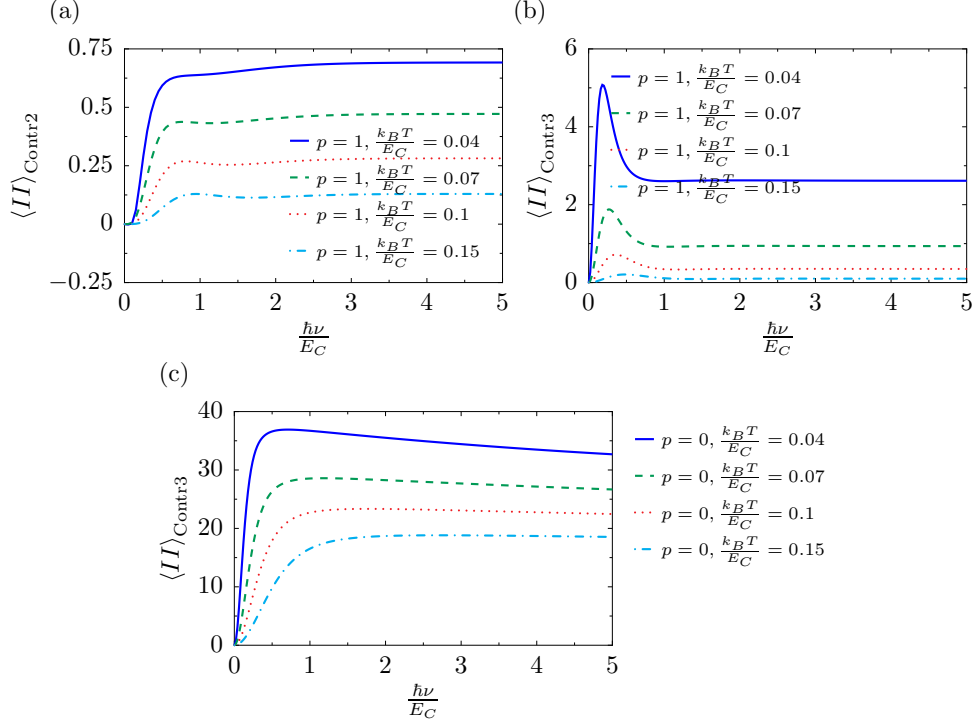
Figure 4.13: Frequency dependence of contributions two (a) and three (b,c) in the case $\eta \to 0$ for different temperatures.

Since the equilibrium typical current is of order e/τ_D (Section 2.4.3, [5, 14, 23]) we will pull a factor $(e/\tau_D)^2 = (\pi E_C/\phi_0)^2$ out of the equation to be able to compare the orders of magnitude of the effects. We get

$$\frac{\langle I_x(\varphi) I_x(\varphi) \rangle}{(e/\tau_D)^2} = \frac{4}{\pi^6} \left(\frac{eER}{\hbar\nu} \right)^4 \mathrm{Re} \left\{ \sum_{p>0} 4 \sin^2(2\pi p\varphi) \left[\langle II \rangle_{\mathrm{Contr.1}} + \langle II \rangle_{\mathrm{Contr.2}} \right] \right\}.$$
(4.103)

In order to see also the effects of higher harmonics on the typical current, we plot the typical current of the first three harmonics for a specific realistic choice of parameters in Figure 4.14.

We can see already in Figure 4.14 that it is possible to find parameters under which the microwave-induced part of the typical current becomes of order of the equilibrium typical current. We also note that the typical current of higher harmonics is damped. It turns out that it is sufficient to take the first three harmonics into account.

We plot the typical current for different frequencies and temperatures in Figure 4.15. As expected the effect is more pronounced for low frequencies.
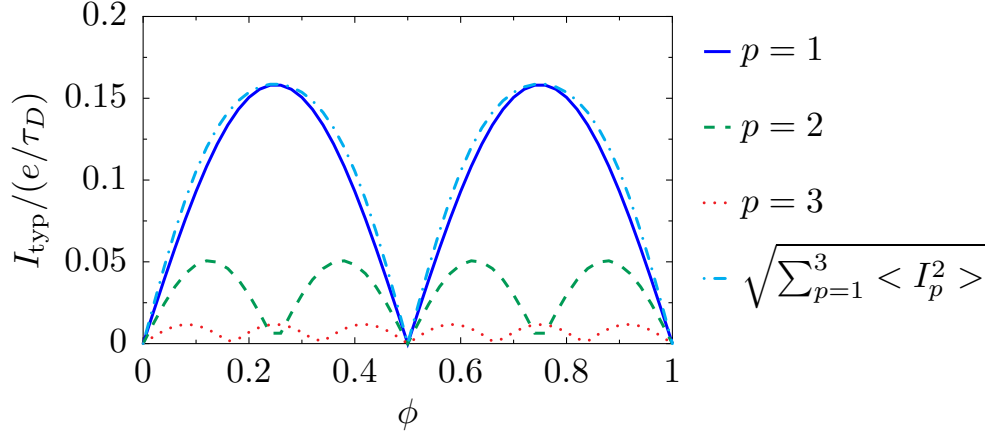
Figure 4.14: Variable part of the microwave-induced typical current of metal rings. We choose the parameters $L = 1.2\,\mu m$, $D = 0.026\,m^2/s$, $\frac{k_B T}{E_C} = 0.07$ and $\frac{h\nu}{E_C} = 5 \cdot 10^{-4}$ which lie well within the region of our approximations.

High intensities

We expect a more pronounced signal for higher field intensities. As argued above we will set $E = 6\,V/m$ which will heat the electronic temperature up to a value just under the characteristic temperature. The results are plottet in Figure 4.16.

It turns out that it seems to be possible to get a signal that is even larger than the eqiulibrium persistent current, but highly suppressed for higher frequencies.

Variation of the frequency

The variation of the frequency of an applied microwave field at different values of the applied flux allows to study the field-dependent part of the persistent current in more detail in an experimental setup. Dependent on the applied flux one can for example observe the contribution of the third part in Eq. (4.72) alone ($\varphi = \varphi' = 0$), or study various combinations of the first two contributions on the one hand and the third contribution on the other. Furthermore it is possible to subtract the equilibrium persistent current as well as the frequency-independent parts of the field-dependent signal from the data.

To illustrate the possibilities we plot the frequency dependence of the expected signal for different values of the applied flux in Figure 4.17. We can see that the contribution of the third part in Eq. (4.72), which corresponds to the photovoltaic effect in Ref. [6], is negligible compared to the other two terms arising from a change in the density of states due to the microwave field at low frequencies, while high frequencies will be highly damped by the ν^{-4}-dependence of the prefactor.

Correlation function

In order to evaluate the effect of a microwave field on the current-current correlation function, we evaluate Eq. (4.72) as a function of the difference $\delta = \varphi - \varphi'$. Setting
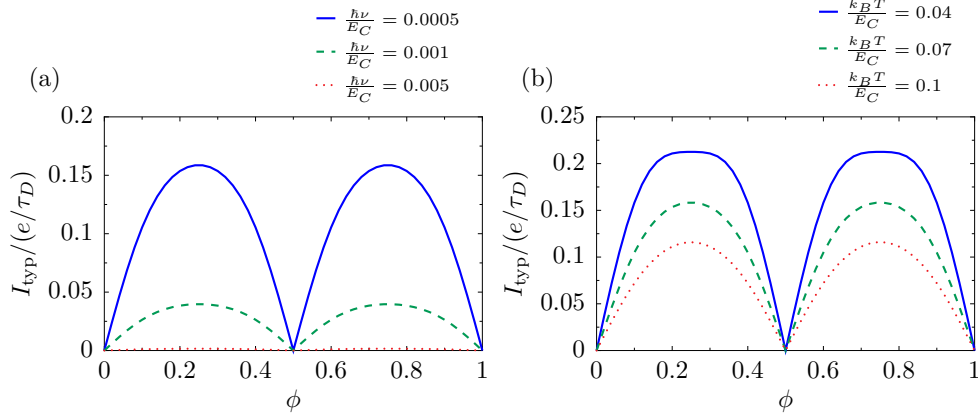
Figure 4.15: Variable part of the microwave-induced typical current of metal rings for different values of the frequency and temperature. (a) Different values for the frequency at temperature $\frac{k_B T}{E_C} = 0.7$, (b) different temperature values for frequency $\frac{\hbar \nu}{E_C} = 5 \cdot 10^{-4}$. We choose the parameters $L = 1.2\,\mu m$, $D = 0.026\,m^2/s$ and $E = 0.15\,V/m$.

$\varphi' = \varphi - \delta$, Eq. (4.72) turns into

$$\langle I_x(\varphi) I_x(\varphi - \delta) \rangle = I_0^2 \operatorname{Re} \Bigg\{ \sum_{p>0} 4 \left(\sin^2(2\pi p \varphi) \cos(2\pi p \delta) - \frac{1}{2} \sin(4\pi p \varphi) \sin(2\pi p \delta) \right)$$

$$\times \left[\langle II \rangle_{\text{Contr.1}} + \langle II \rangle_{\text{Contr.2}} \right] \Bigg\} + \langle II \rangle_{\text{Contr.3,p=0}} + \sum_{p>0} 2 \cos(2\pi p \delta) \, \langle II \rangle_{\text{Contr.3}} \, .$$

$$(4.104)$$

We plot the correlation function for different values of φ and the frequency and temperatures already used above in Figure 4.18. One can see that the correlation function is dominated by the first two terms in Eq. (4.72) as long as $\varphi \neq 0$. As one can expect from Eq. (4.104), not only the magnitude but also the phase of the harmonics in the correlation function is shifted when φ varies.

For higher frequencies the three contributions can become of similar order of magnitude as it can be seen in Figure 4.13. To obtain an larger effect from the third contribution, we evaluate the correlation function at the the frequency leading to the maximal signal from this contribution. As shown in Figure 4.19, this leads to a mix of the different harmonics in the correlation function. However, the magnitude of the effect is in this case small compared to the equilibrium persistent current which makes an experimental observation improbable.
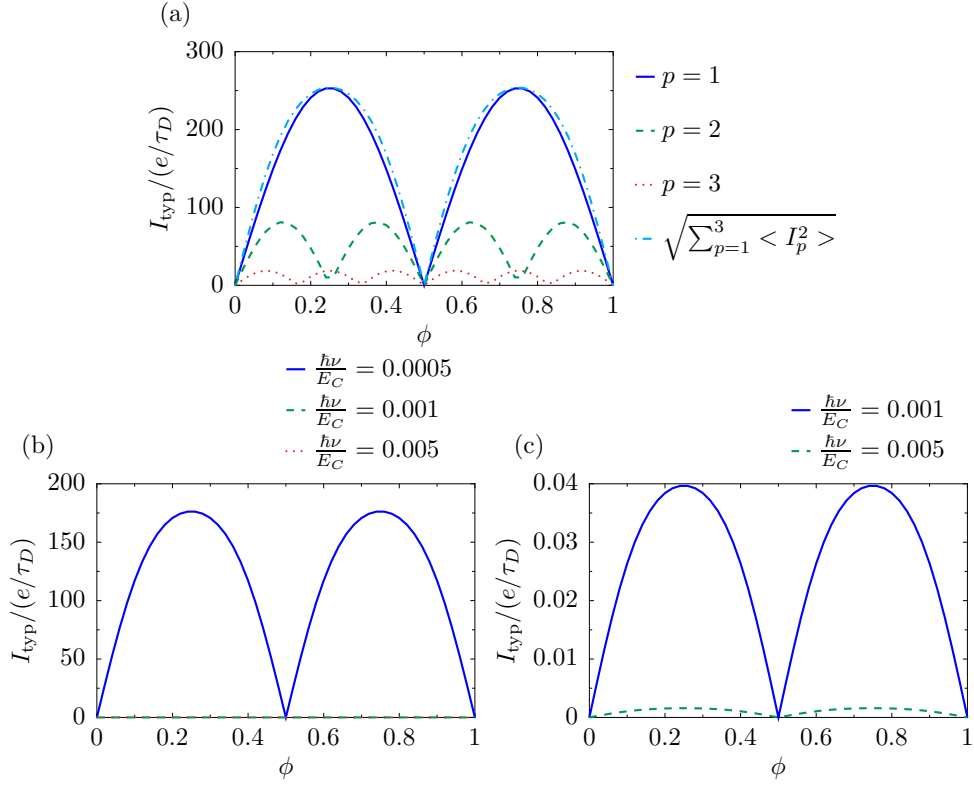
Figure 4.16: Microwave-induced typical current for high field intensities. The electronic temperature is fixed by the field at $T_e \sim 0.8\,K$. The other parameters are $E = 6\,V/m$, $L = 1.2\,\mu m$ and $D = 0.026\,m^2/s$. (a) Shows different harmonics for $\frac{\hbar\nu}{E_C} = 5 \cdot 10^{-4}$, (b) depicts the typical current for different frequencies, while the lower two frequencies are depicted in (c) again.
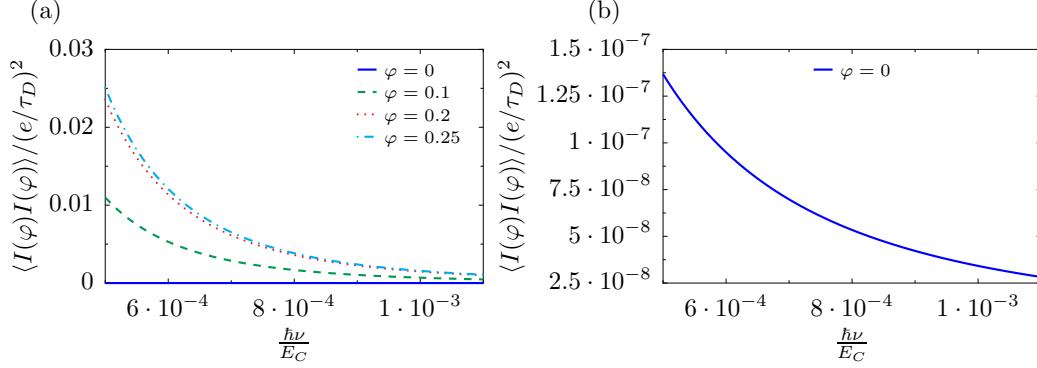
Figure 4.17: Frequency dependence of the microwave-induced current correlation function for different values of the magnetic flux. (a) For $\varphi \neq 0$ the correlation function is dominated by the first two terms in Eq. (4.72), while in (b) $\varphi = 0$ picks out the contribution of the third term alone. We choose the parameters $L = 1.2\,\mu m$, $D = 0.026$, $E = 0.15\,V/m$, $\frac{k_B T}{E_C} = 0.7$.
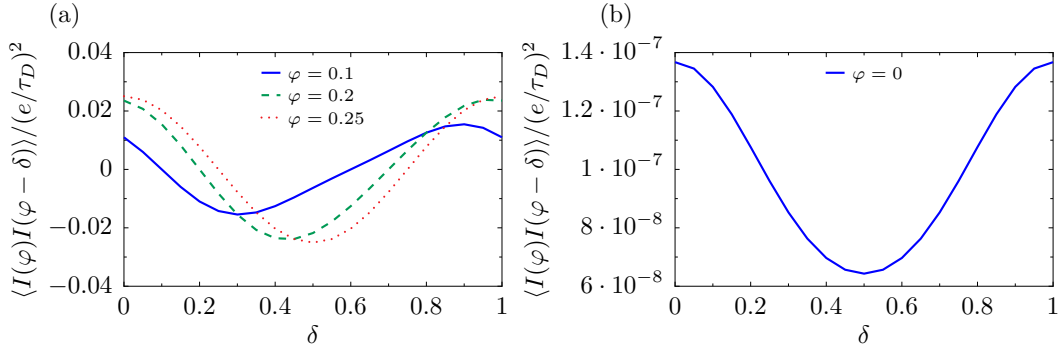
Figure 4.18: Dependence on $\delta = \varphi - \varphi'$ of the microwave-induced current correlation function of metal rings for different values of φ. (a) For $\varphi \neq 0$ the first two terms dominate correlation function, while in (b) $\varphi = 0$ picks out the contribution of the third term alone. We choose the parameters $L = 1.2\,\mu m$, $D = 0.026$, $E = 0.15\,V/m$, $\frac{k_B T}{E_C} = 0.7$ and $\frac{\hbar \nu}{E_C} = 5 \cdot 10^{-4}$.
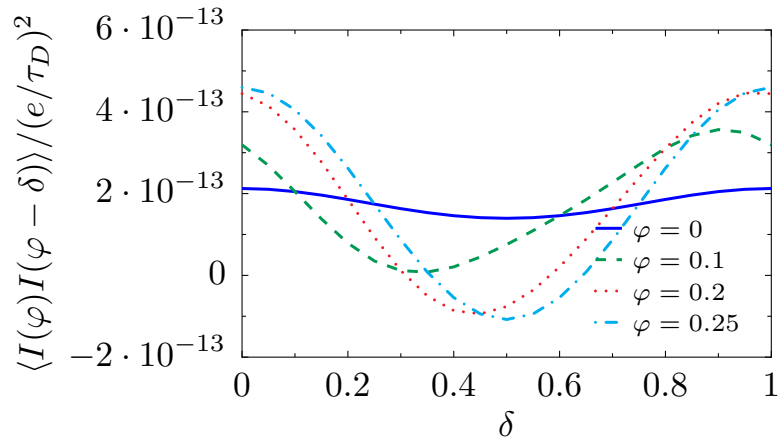
Figure 4.19: Dependence on $\delta = \varphi - \varphi'$ of the microwave-induced current correlation function in the high-frequency regime. We choose the parameters $L = 1.2\,\mu m$, $D = 0.026$, $E = 0.15\,V/m$, $\frac{k_B T}{E_C} = 0.7$ and $\frac{\hbar \nu}{E_C} = 1$.

Chapter 5

Conclusions and outlook

In the first part of the thesis we have considered normal (non-superconducting) metal rings which exhibit persistent currents under breaking of time-reversal symmetry. We have extended existing theories towards the inclusion of an additional microwave field which drives the system out of equilibrium. For this we have treaten the problem in the Keldysh formalism which inherently allows for out-of-equilibrium studies. The considerations concentrated on experimentally significant quantities like the average and the typical current.

We have seen that an additional microwave field can cause an extra contribution to the persistent current of normal metal rings which can be of the order of the equilibrium current for an appropriate choice of field amplitude and frequency. This additional contribution splits in two parts originating from different physical effects. First, the presence of the microwave field gives rise to corrections to the density of states which in turn affects the current correlation function. Second, the random impurity distribution in the rings can cause local symmetry breaking which leads to a photovoltaic effect in mesoscopic samples under microwave irradiation, as already stated in Ref. [6].

Our analysis has shown that in the considered regime the first effect produces a signal which is orders of magnitude larger that the photovoltaic effect, and strongly damped for higher temperatures and frequencies. The characteristic temperature scale is of order k_B/E_C which coincides with the equilibrium persistent current. We have seen that we can choose parameters within the assumptions of our operturbative approach under which the additional signal will be of the same order of magnitude or even larger than the equilibrium persistent current. Thus adding an additional microwave field with appropriate frequency and amplitude will lead to a clear measurable additional signal.

In the following we will comment on various limits and expansions of our assumptions which can motivate future work on the subject.

5.1 Kinetic equation for the Keldysh Green function

In our considerations we have assumed that the electronic distribution stays in its equilibrium form and that we can account for the effect of the microwave field on the electronic distribution by considering an electronic temperature estimated in Section 4.4.2. In our expressions the amplitude E of the microwave field enters through a prefactor proportional

to E^4 and through the change in the electronic temperature $T_{el} = \left(\frac{\sigma_0 E^2}{4\Sigma} + T_p h^5 \right)^{1/5}$ (cf. Eq. (4.84)). However, this rough estimate will presumably not be sufficient when predicting the dependence of the current correlation function on the amplitude of the microwave field. A more detailed analysis could be based on a kinetic equation for the Keldysh Green function as it is done e.g. in Refs. [39, 40].

The strategy of this analysis is not to replace the Keldysh Green function contained in expression (4.50) of the current in second order in the field by its equilibrium form (4.15), but to expand the Keldysh Green function in the field, too.

5.2   In-plane microwave field

Throughout the calculation we have assumed the microwave field to stand perpendicular to the ring. This led to numerous calculational simplifications mentioned in Section 4.3. However, in an experiment like that in Ref. [14] it will be hard to realize a field without in-plane components. An in-plane microwave field will influence the motion of the electrons directly and can lead to physically distinct features. In the calculations this will manifest in considering also diagrams in which the field interactions do not come in pairs and will eventually even give rise to second order contributions and contributions from the diamagnetic current.

Part II

Quantum dots with vibrational degrees of freedom and negative-U instability

The second part of the thesis is dedicated to studying quantum dots with vibrational degrees of freedom. Here the term "quantum dot" describes a low-dimensional nanometer-sized system which serves as a confinement of only a few electrons and was introduced by M. Reed *et al.* [41]. Artificial creation of such controllable and manipulable few-electrons quantum confinements opened a field of physics in which it is possible to study paradigms of quantum mechanical many body systems.

Besides the scientific motivation to create such "artificial atoms" or "designer atoms", as quantum dots were called in the beginning [42, 43], also the potential for technological applications is exciting. The miniaturization process of semiconductor microchips, empirically remarkably well described by "Moore's law" [44], suggests that dealing with quantum mechanical effects in electric devices will become necessary if the progress in constructing faster and more powerful transistors is maintained.

The most intuitive way to think of an experimental realization of a quantum dot is to fabricate the system by restricting a two dimensional electron gas (e.g. realized in a semiconductor heterostructure or graphene) laterally, using electrostatic gates [45, 46], or vertically by etching techniques [47]. Other experimental techniques involve electron beam lithography [48, 49] or optical confinements [50]. Preparation of these devices made it possible to study effects of one dimensional physics, such as localization and electron electron interactions [51, 52] as well as trapping of single electrons [53] and universal conductance fluctuations [54].

The concept of coupling the electronic degrees of freedom of a quantum dot to vibrational modes and effects following from this coupling is known for several decades [55, 56, 57]. However, it attracted even more notice when it became possible to fabricate devices where single molecules serve as quantum dots [58], since experimental observations suggested, that the electronic degrees of freedom couple to a single vibrational mode of the molecule, describing e.g. nanomechanical vibrations [59]. Implications of this coupling are vibrational sidebands in the current-voltage characteristics, the so called Franck-Condon blockade [60], and the formation of a regime with an effectively negative charging energy, the so-called negative-U regime [10].

In this second part of the thesis we analyze a variation of the latter situation. The electron phonon coupling is in the negative-U regime so strong, that it leads to an effectively negative charging energy which causes an instability. In Ref. [10] a situation where the effective charging energy was negative but smaller than the loss in single-particle energy was analyzed. We analyze the counterpart of this situation where the energy gain from adding or removing one electron to the quantum dot overcomes the cost in single-particle energy due to finite level spacing. Here the instability can be regularized by the anharmonic contribution to the vibron energy. The resulting effective charging energy as a function of the electron number takes a double well form leading to new features in Coulomb-blockade physics, which are discussed here. We also argue, that the negative-U regime discussed is accessible to modern day experimental techniques.

The outline of this part of the thesis is as follows. In the first section (6.1) we will introduce the basic theoretical formalism for single electron transistors with vibrational degrees of freedom and derive basic effects. After that we will turn to molecular quantum dots and comment on the new physics emerging due to the coupling of the quantum dot to a vibrational degree of freedom in Section 6.2. Section 7 will deal with the negative-U

case. First we review theoretical work on molecules with large electron phonon coupling [10, 61] and then consider the situation in metallic quantum dots (i.e. quantum dots with a continuous density of states), discussing the instability towards adding or removing an arbitrary number of electrons to or from the dot, which occurs in the common model. Finally we discuss the consequences of an anharmonic term added to regulate the instability in the negative-U regime, first on equilibrium (Section 7.3) and then on transport results (Section 7.4). We conclude in Section 7.6.

Citations to previously published work Large portions of chapter 7, in particular sections 7.2, 7.3, 7.4 and 7.6 have been published in [62].

Chapter 6

Basic formalism

We begin by introducing the basic formalism describing single-electron tunneling through quantum dots. The section splits basically in two parts. First we will concentrate on so-called metallic quantum dots, i.e., systems with a continuous density of states, and then we will extend the theory to include also effects in molecular quantum dots where the level spacing is large, so that transport can be assumed to be dominated by a single energy level on the dot. In deriving the basic effects we will also comment shortly on the corresponding experiments.

In common devices, the quantization of charge, first measured by Millikan in 1911 [63], cannot be perceived in voltage or current measurements. The reason for this is, of course, on the one hand, that the number of electrons is very large in macroscopic devices, but also that the flow of charge in conducting materials is a continuous process involving delocalized electrons. E.g., the charge on a capacitor can be shifted by arbitrary small amounts, just by shifting the position of the electronic fluid with respect to the ionic background. In order to observe single-electron effects in solid state devices, one thus has to make use of a tunneling effect. Two metallic electrodes that are separated by an insulating barrier which is so thin that electrons can tunnel through it from one lead to the other, exhibit effectively quantized transport characteristics if a voltage is applied across the sample. On top of this tunneling effect, the two electrodes also behave as a capacitor. Thus the so called tunnel resistance R_t of the insulating barrier and the capacitance C of the capacitor are the two macroscopic parameters of such a junction. The tunnel resistance R_t is defined via the rate V/eR_t at which the electrons tunnel across the junction if a voltage V is applied, and is fundamentally different from the ohmic resistance of a usual resistor through which charge can flow continuously.

6.1 Metallic quantum dots

As mentioned, we call a quantum dot metallic if it has such a high density of states that many electronic levels are involved in transport through the dot. In introducing the basic concepts we will mainly follow the introduction in [64, Chapter 3]. We start by studying the effect of the number of electrons, the transport- and the gate voltage on the charging energy in two standard systems, the so called single-electron box (Section 6.1.1)and the

single-electron transistor (Section 6.1.2). After this we will introduce the formalism used to study transport in this system in Section 6.1.3.

6.1.1 Single-electron box

The single electron box (SEB) is the most simple system for which we can analyze charging effects. It contains a tunneling junction which can be thought to be a small metallic island between two metallic leads, and which is capacitively coupled to a gate voltage source, such that a metallic island is formed between the gate-voltage-capacitor and the tunnel junction. Since the island is surrounded by insulating material, the only way for electrons to enter or leave is through the tunnel junction. An equivalent circuit of the SEB can be seen in Figure 6.1.
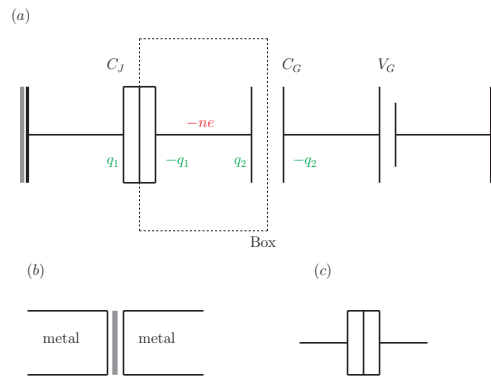
Figure 6.1: (a) Equivalent circuit of the single electron box. C_G is the capacitance of the coupling electrode, C_J the tunnel capacitance, V_G the gate voltage and $-ne$ the charge on the quantum dot. $\pm q_i$ denote the charges on the different sides of the capacitors. (b) Schematic drawing of the tunnel junction. (c) Symbol for a metallic tunnel junction.

One can define the number of excess electrons n on the island as the difference of the charges on the two capacitor plates within the island in multiples of the electron charge, i.e. $q_2 - q_1 = ne$ in the notation of Figure 6.1. Although q_1 and q_2 are continuous variables as discussed before, n is integer since electrons can enter or leave the island only one by one. If the gate voltage is zero, in the lowest energy state there are $n = 0$ excess electrons on the island. Changing the gate voltage results in a change of the number of electrons, which can tunnel across the junction, on the island. While the gate voltage can be tuned continuously, the number of electrons on the island is discrete. The charging energy, i.e. the energy needed for n electrons to tunnel on the island can be derived by standard electrostatic arguments ([64], Appendix B.1), and is given by

$$E_{\text{ch}}(n, Q_g) = \frac{(ne - Q_g)^2}{2C} \, , \tag{6.1}$$

where $Q_G = C_G V_G$ stands for the gate charge, and $C = C_J + C_G$ denotes the total capacitance of the island. In a plot (Figure 6.2) of the charging energy one can see that in the lowest energy state the number of electrons increases with increasing gate voltage

in discrete steps. It increases from n to $n+1$ at the point $Q_G/e = n + 1/2$, so that the number of electrons becomes a step-like function of the gate charge.
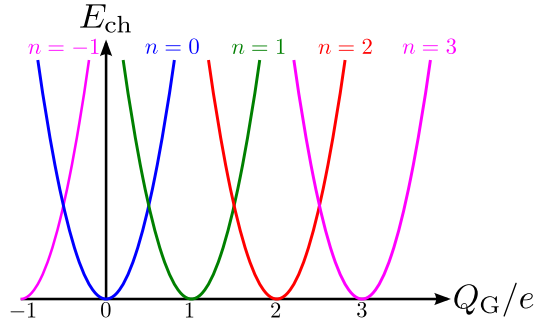
Figure 6.2: Charging energy $E_{\text{ch}}(n, Q_G)$ of a SEB as a function of the gate voltage. The differently colored curves stand for different numbers n of electrons on the quantum dot.

For finite temperatures this step-like behavior is washed out, and the steps are rounded, vanishing when the characteristic energy $k_B T$ of one excess electron on the island becomes large compared to the electrostatic energy $E_C = e^2/2(C_J + C_G)$.

6.1.2 Single electron transistor

As it can be seen in the equivalent circuit (Figure 6.3), the single electron transistor (SET) consists of two tunnel junctions capacitively coupled to a gate voltage. Across the island, which is indicated by a dotted square in Figure 6.3, a voltage drop $V_L - V_R$ is applied such that a current can flow.
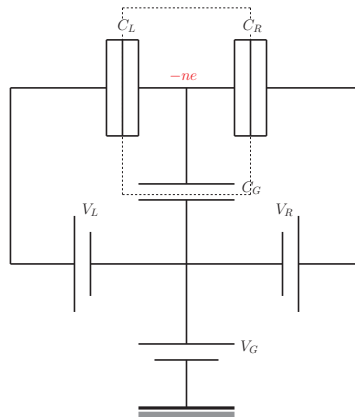
Figure 6.3: Equivalent circuit of a single electron transistor.

The charging energy of the SET is derived in Appendix B.2 (cf. [64, 65]) and again given by

$$E_{\text{ch}} = \frac{(ne - Q_G)^2}{2C} \, , \tag{6.2}$$

77

where $C = C_L + C_R + C_G$ is the sum of the capacitances, and $Q_G = C_L V_L + C_R V_R + C_G V_G$ is the gate charge defined by the three voltage sources. Thus adding an electron to the island by tunneling changes the charging energy by

$$E_{\mathrm{ch}}(n+1, Q_G) - E_{\mathrm{ch}}(n, Q_G) = \frac{e^2}{2C}\left(2n + 1 - \frac{2Q_G}{e}\right), \qquad (6.3)$$

which leads to equidistant energy levels on the dot that can be shifted by the gate voltage. Two distinct situations are drafted in Figure 6.4. If an energy level on the dot lies between the chemical potentials of the leads (we assume $V_L > V_R$ for simplicity) a tunneling current can flow, but if there is no dot-energy level between the lead energy levels (Figure 6.4 (b)) the system is in the so called Coulomb blockaded regime, and no current can flow although a voltage is applied. In a plot of the conductance in the $(V_L - V_R, V_G)$-plane this leads to
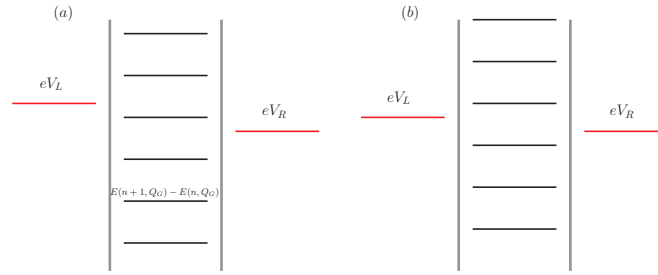
Figure 6.4: Draft of the energy levels of the leads (red) and on the dot (black). (a) One energy level of the dot lies between the energy levels of the leads, such that a tunneling current can flow. (b) Coulomb blockade: Although a net voltage $V_L - V_R > 0$ is applied, no current can flow, since there is no energy level on the dot available to tunnel through.

the so called Coulomb diamond structure shown in Figure 6.5. Tunneling from the left lead into the island is allowed, if $eV_L > E_{\mathrm{ch}}(n+1, Q_G) - E_{\mathrm{ch}}(n, Q_G)$, and tunneling from the island into the right lead requires $E_{\mathrm{ch}}(n+1, Q_G) - E_{\mathrm{ch}}(n, Q_G) > eV_R$. If both conditions are fulfilled simultaneously, a current can flow through the SET.

6.1.3 Rate equations

After introducing a qualitative picture of the basic effects in a SEB and a SET, we turn now to a more quantitative description of the tunneling of electrons in a SET. This is done by introducing the Hamiltonian of the system and using first order perturbation theory ("Fermis golden rule") in the tunneling constants, leading to a good picture of the system in the unblocked regime. Within the Coulomb blockade regime, higher order tunneling processes like cotunneling become important[1].

The Hamiltonian of a SET consists of five parts and can be written as

$$H = H_{\mathrm{L}} + H_{\mathrm{I}} + H_{\mathrm{R}} + H_{\mathrm{ch}} + H_{\mathrm{tun}} \qquad (6.4)$$

[1]For a review of cotunneling effects, see e.g. [66, Section 6]
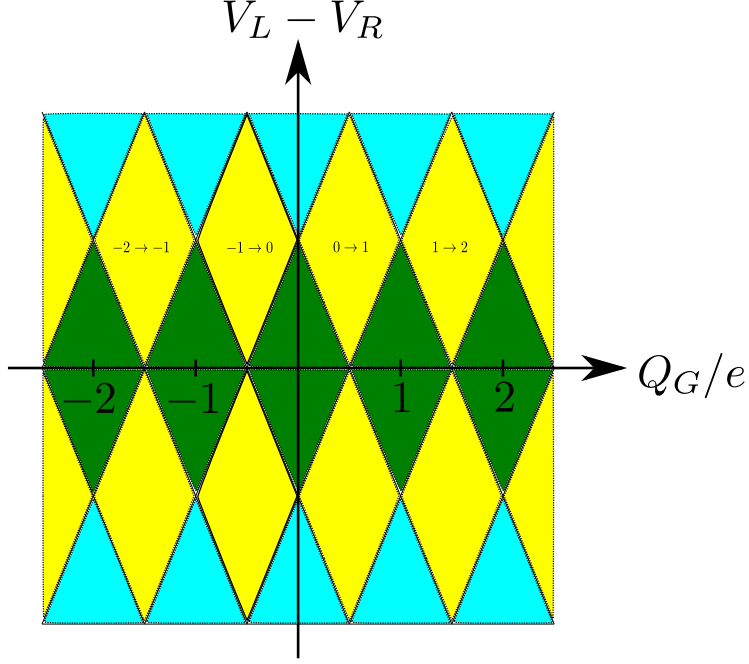
Figure 6.5: Coulomb blockade diamonds for a symmetric SET. The green areas are in the Coulomb blockaded regime where no current flows, in the yellow (light blue) areas one (two) channel(s) on the dot lie(s) between the left and the right gate energies.

where $H_\mathrm{L} + H_\mathrm{R} = \sum_{\boldsymbol{k},\sigma} \epsilon_{\boldsymbol{k}} \, c^\dagger_{\boldsymbol{k},\sigma} c_{\boldsymbol{k},\sigma} + \sum_{\boldsymbol{q},\sigma} \epsilon_{\boldsymbol{q}} \, c^\dagger_{\boldsymbol{q},\sigma} c_{\boldsymbol{q},\sigma}$, $c^\dagger_{\boldsymbol{k},\sigma} \, (c_{\boldsymbol{k},\sigma})$ the creation (annihilation) operator of an electron with momentum $\boldsymbol{k}$ and spin σ, describes the quasiparticles in the two metal electrodes, $\boldsymbol{k}$ represents the momentum of an electron in the left, and $\boldsymbol{q}$ in the right electrode, and H_I describes the electrons on the island. H_ch is the Coulomb interaction which we assume to depend only on the number of excess electrons on the island and which is thus equal to the charging energy,

$$H_\mathrm{ch} = \frac{(\hat{n} - Q_G)^2}{2C} \, , \tag{6.5}$$

$\hat{n}$ the number operator, and H_tun is the tunneling Hamiltonian describing charge transfer from and to the island, e.g. for the tunneling between the left lead and the dot

$$H_\mathrm{tun,L} = \sum_{\boldsymbol{k},\boldsymbol{p},\sigma} t_{\boldsymbol{k},\boldsymbol{p}} c^\dagger_{\boldsymbol{k},\sigma} c_{\boldsymbol{p},\sigma} + \mathrm{h.c.} \, , \tag{6.6}$$

where the term written out describes the annihilation of an electron in state $(\boldsymbol{p}, \sigma)$ on the island and creation of an electron in state $(\boldsymbol{k}, \sigma)$ on the left electrode, i.e. tunneling from the island to the left electrode, and $t_{\boldsymbol{k},\boldsymbol{p}}$ is the respective tunneling probability amplitude. The hermitian conjugate describes the conjugated process $(\boldsymbol{k}, \sigma)_\mathrm{left\ electrode} \longrightarrow (\boldsymbol{p}, \sigma)_\mathrm{island}$.

Tunneling rates We now calculate the tunneling rates, starting with the Hamiltonian (6.4). We consider the tunneling Hamiltonian H_tun as a perturbation and calculate the

tunneling rate within the golden rule approximation

$$\Gamma_{i \to f} = \frac{2\pi}{\hbar} \, |\langle f|H_{\text{tun}}|i\rangle|^2 \, \delta(E_i - E_f) \,, \tag{6.7}$$

where $E_{i(f)}$ is the energy of the initial (final) state $|i\rangle$ ($|f\rangle$). For tunneling between the left lead and the island, the tunneling element thus becomes

$$\langle f|H_{\text{t}}|i\rangle = \langle E_f|H_{\text{tun}}^e|E_i\rangle + \langle E_f|H_{\text{tun}}^{e\,\dagger}|E_i\rangle \,, \tag{6.8}$$

where we used the shortcut $H_{\text{tun}}^e = \sum_{\boldsymbol{k},\boldsymbol{p},\sigma} t_{\boldsymbol{k},\boldsymbol{p}} c_{\boldsymbol{k},\sigma}^\dagger c_{\boldsymbol{p},\sigma}$. The total rate of electrons tunneling from the left lead into the island can be calculated by summing over all initial and final states, weighted with the probabilities to find the initial state occupied, $f_L(\epsilon_{\boldsymbol{k}})$, and the final state empty, $[1 - f_I(\epsilon_{\boldsymbol{p}})]$, where $f(\epsilon)$ is the distribution function. We get, assuming the tunnel probability amplitudes to be constants, $t_{\boldsymbol{k},\boldsymbol{p}} \equiv t$,

$$\Gamma_{\text{LI}} = \frac{4\pi}{\hbar} N_I(0)\Omega_I N_L(0)\Omega_L |t|^2 \int_{-\infty}^{\infty} d\epsilon_{\boldsymbol{k}} \int_{-\infty}^{\infty} d\epsilon_{\boldsymbol{p}} \, f_L(\epsilon_{\boldsymbol{k}}) \, [1 - f_I(\epsilon_{\boldsymbol{p}})] \, \delta(\epsilon_{\boldsymbol{p}} - \epsilon_{\boldsymbol{k}} + \delta E_{\text{ch}}) \,, \tag{6.9}$$

which can be reduced to

$$\Gamma_{\text{LI}} = \frac{1}{e^2 R_{\text{t,L}}} \int_{-\infty}^{\infty} d\epsilon_{\boldsymbol{k}} \int_{-\infty}^{\infty} d\epsilon_{\boldsymbol{p}} \, f_L(\epsilon_{\boldsymbol{k}}) \, [1 - f_I(\epsilon_{\boldsymbol{p}})] \, \delta(\epsilon_{\boldsymbol{p}} - \epsilon_{\boldsymbol{k}} + \delta E_{\text{ch}}) \,, \tag{6.10}$$

where we introduced the tunnel conductance

$$\frac{1}{R_{\text{t,L}}} = \frac{4\pi e^2}{\hbar} N_I(0)\Omega_I N_L(0)\Omega_L |t|^2 \,, \tag{6.11}$$

with $N_{I/L}(0)$ the density of states at the Fermi level of the island and the left lead respectively, and $\Omega_{I/L}$ the corresponding volumes,

The tunneling rate depends on the applied voltage at the left lead and the gate voltage through the charging energy term in the delta function. Explicitly we have

$$\delta E_{\text{ch}} = E_{\text{ch}}(n + 1, Q_G) - E_{\text{ch}}(n, Q_G) - eV_L \,. \tag{6.12}$$

In a situation where we can assume the distribution functions $f_{L/I}(\epsilon)$ on the leads and on the island to stay in their equilibrium form, i.e. to take the form of a Fermi function, we can perform the integrals, leading to

$$\Gamma_{\text{LI}}(n) = \frac{1}{e^2 R_{\text{t,L}}} \frac{\delta E_{\text{ch}}}{e^{\delta E_{\text{ch}}/k_B T} - 1} \,. \tag{6.13}$$

From this equation, we can already deduce the basic properties introduced sections 6.1.1 and 6.1.2. For low temperatures, $k_B T \ll \delta E_{\text{ch}}$, tunneling is suppressed if $\delta E_{\text{ch}} > 0$, i.e., if the charging energy increases in the tunneling process. Since the change of the charging energy is given by Eq. (6.12), and current can only flow if tunneling from the left lead to the island and tunneling from the island to the right lead are not suppressed, this leads to the same conditions for a current to flow as derived in the end of Section 6.1.2.

Master equations Master equations are equations for the evolution of the probabilities $p_s(t)$ that the system can be found in state $|s\rangle$ at time t. In this paragraph we will derive the form of those equations phenomenologically following [67] and show how to use them to get expressions for the current through the quantum dot. A systematic derivation using diagrammatic techniques can be found in Refs. [68, 69].

The starting point is a simplified version of the model (6.4), $H = H_{\mathrm{dot}} + H_{\mathrm{tun}} + H_{\mathrm{L}} + H_{\mathrm{R}}$, where $H_{\mathrm{L/R/tun}}$ takes the same form as before (after Eq. (6.4)), and H_{dot} is assumed to contain all forms of interactions and to be diagonalized

$$H_{\mathrm{dot}} = \sum_s E_s |s\rangle\langle s| , \tag{6.14}$$

$|s\rangle$ denoting the discrete many body state on the dot. We further assume a symmetric splitting of the transport voltages, $\mu_{\mathrm{L/R}} = \mu \pm V/2$, and that the applied bias voltage is static, which will lead to stationary expressions for the probabilities $p_s(t) \equiv p_s^{\mathrm{st}}$. The change in the occupation probabilities $p_s(t)$ is now given by the sum of the transition rates $\Gamma_{s,s'}$ weighted with their respective probabilities

$$\dot{p}_s(t) = \sum_{s'} \Gamma_{s's} p_{s'}(t) , \tag{6.15}$$

which turns after defining the matrix $(\bar{\mathbf{\Gamma}})_{s's} = \Gamma_{s's}$ and the vector $(\boldsymbol{p}^{\mathrm{st}})_s = p_s^{\mathrm{st}}$ in the stationary case into

$$\bar{\mathbf{\Gamma}} \boldsymbol{p}^{\mathrm{st}} = 0 . \tag{6.16}$$

We can include the normalization $\sum_s p_s = 1$ by replacing one arbitrary row in the matrix $\bar{\mathbf{\Gamma}}$ by $(1, \ldots, 1)$ making the overdetermined Eq. (6.16) invertible and leading to the solution

$$\boldsymbol{p}^{\mathrm{st}} = (\tilde{\mathbf{\Gamma}})^{-1} \boldsymbol{v} . \tag{6.17}$$

Here $\tilde{\mathbf{\Gamma}}$ is equal to the matrix $\bar{\mathbf{\Gamma}}$ but with row r replaced by $(1, \ldots, 1)$, and $(\boldsymbol{v})_s = \delta_{s,r}$. The current through e.g. the left lead, which is under symmetric conditions equal to the total current, can now be calculated as the sum of the transitions rates times the occupation probabilities over all states,

$$I_{\mathrm{L}}(t) = -e \sum_s \left[\Gamma_{\mathrm{LI}}(s) - \Gamma_{\mathrm{IL}}(s) \right] p_s(t) . \tag{6.18}$$

To illustrate the usability of the master equations we derive the qualitative results from sections 6.1.1 and 6.1.2 within an easy model, assuming sequential tunneling and a two level system. We further assume the temperature and the transport voltage V to be so small, that only two levels on the dot have a non vanishing probability $p(n, t)$. Thus we have a two level system effectively. We can call the levels n and $n + 1$, which means, that we assume $ne < Q_G < (n+1)e$, where $Q_G = C_G V_G + C_L V_L + C_R V_R$ is the gate charge. We also can neglect all tunneling rates but those changing the island charge from n to $n + 1$ electrons or the other way round, i.e. $\Gamma_{\mathrm{IL}}(n+1)$, $\Gamma_{\mathrm{IR}}(n+1)$, $\Gamma_{\mathrm{RI}}(n)$ and $\Gamma_{\mathrm{LI}}(n)$.

In the sequential tunneling regime, i.e. if we assume, that just one electron tunnels at a time, Eq. (6.15) simplifies to

$$\frac{d}{dt}p(n,t) = \left[\Gamma_{\mathrm{LI}}(n-1) + \Gamma_{\mathrm{RI}}(n-1)\right]p(n-1,t) + \left[\Gamma_{\mathrm{IL}}(n+1) + \Gamma_{\mathrm{IR}}(n+1)\right]p(n+1,t)$$
$$- \left[\Gamma_{\mathrm{LI}}(n) + \Gamma_{\mathrm{IL}}(n) + \Gamma_{\mathrm{IR}}(n) + \Gamma_{\mathrm{IR}}(n)\right]p(n,t), \tag{6.19}$$

where we denoted the states by the number n of excess electrons on the dot. The first line in Eq. (6.19) describes processes changing the number of electrons on the dot from $n \pm 1$ to n, and the second line subtracts processes, where the number of electrons changes from n to $n \pm 1$. Note, that if we are interested in DC-current the current through the left and right lead will be equal, $I_{\mathrm{L}} = I_{\mathrm{R}}$, and we can use the stationary solution of (6.19), i.e. we can set $\frac{d}{dt}p(n,t) = 0$.

As a further simplification of the model we first assume, that the bias voltage is symmetric, $V_L = V_R = V/2$. The stationary solution of the master Eq. (6.19) reads

$$p(n) = \frac{\Gamma_{\mathrm{IL}}(n+1) + \Gamma_{\mathrm{IR}}(n+1)}{\Gamma_{\mathrm{LI}}(n) + \Gamma_{\mathrm{RI}}(n) + \Gamma_{\mathrm{RI}}(n+1)} \text{, and}$$
$$p(n+1) = \frac{\Gamma_{\mathrm{IL}}(n) + \Gamma_{\mathrm{IR}}(n)}{\Gamma_{\mathrm{LI}}(n) + \Gamma_{\mathrm{RI}}(n) + \Gamma_{\mathrm{RI}}(n+1)}, \tag{6.20}$$

where we used $p(n) + p(n+1) = 1$. Inserting this in Eq. (6.18) and again taking just those tunneling processes into account which leave the dot in state n or $n+1$ yields

$$I = I_L = I_R = -e\left[\Gamma_{\mathrm{LI}}(n)\,p(n) - \Gamma_{\mathrm{IL}}(n+1)\,p(n+1)\right]$$
$$= -e\frac{\Gamma_{\mathrm{LI}}(n)\Gamma_{\mathrm{IR}}(n+1) - \Gamma_{\mathrm{IL}}(n+1)\Gamma_{\mathrm{RI}}(n)}{\Gamma_{\mathrm{LI}}(n) + \Gamma_{\mathrm{RI}}(n) + \Gamma_{\mathrm{RI}}(n+1)}. \tag{6.21}$$

The change in the charging energy determining the tunneling rates is given by Eqs. (6.3) and (6.12), and turns in the case of symmetric bias voltage into

$$\delta E_{\mathrm{ch}}^{L/R} = \pm\left[E_{\mathrm{ch}}(n+1, Q_G) - E_{\mathrm{ch}}(n, Q_G) \mp \frac{eV}{2}\right]$$
$$= \pm\left[\frac{e^2}{2C}\left(2n+1 - \frac{2Q_G}{e}\right) \mp \frac{eV}{2}\right], \tag{6.22}$$

where the upper sign stands for the tunneling process from the left lead to the island, changing the state of the island from n to $n+1$ and the lower sign for tunneling from the island to the right lead changing the island state from $n+1$ to n. These are the processes which are allowed for $V > 0$, i.e. in the case where the current flows from left to right.

We can see, that tunneling from the left lead to the island is allowed at low temperatures ($\Gamma_{\mathrm{LI}}(n) \neq 0$), if $2Q_G - (2n+1)e \geq -VC$, and tunneling from the island to the right lead is allowed ($\Gamma_{\mathrm{IR}}(n+1) \neq 0$), if $2Q_G - (2n+1)e \leq VC$. Since both tunneling processes have to be allowed for a current to flow, we reproduced the same condition as we already deduced heuristically in Section 6.1.2, and a current can flow in a window $-VC \leq 2Q_G - (2n+1)e \leq$

VC. The current within this window can be calculated in the limit $T \to 0$ using the tunneling rates in equation (6.13), which fro zero temperature are given by

$$\Gamma_{\mathrm{LI}}(n) = \frac{1}{e^2 R_{\mathrm{t,L}}} \left| \delta E_{\mathrm{ch}}^L \right| \text{, and}$$

$$\Gamma_{\mathrm{IR}}(n+1) = \frac{1}{e^2 R_{\mathrm{t,R}}} \left| \delta E_{\mathrm{ch}}^R \right| . \tag{6.23}$$

Assuming symmetric tunnel junctions where $R_{\mathrm{t,L}} = R_{\mathrm{t,R}} \equiv R_{\mathrm{t}}$, we get for the current

$$I = -e \frac{\Gamma_{\mathrm{LI}}(n) \Gamma_{\mathrm{IR}}(n+1)}{\Gamma_{\mathrm{LI}}(n) + \Gamma_{\mathrm{IR}}(n+1)}$$
$$= \begin{cases} \frac{1}{4R_{\mathrm{t}}} \left[V - \frac{e^2}{C^2 V} \left(2n + 1 - \frac{2Q_G}{e} \right)^2 \right] & \text{if } -VC \leq 2Q_G - (2n+1) \leq VC \\ 0 & \text{else} \end{cases} . \tag{6.24}$$

This function is illustrated in Figure 6.6, where the Coulomb blockade regime manifests itself in the fact, that for integer Q_G/e the current vanishes as long as the bias voltage is below e/C. We also see evenly spaced peaks around half integer values of Q_G/e, consistent with what we expect from the qualitative discussion in Section 6.1.3.

As we have already seen in Figure 6.5, at higher transport voltages, $V > e/C$, more charge states contribute to the transport than we took into account in our two level model, since the voltage is high enough to overcome the increase of charging energy when an additional electron enters the island from the left lead. The steps in which the respectively next charge state comes into play are at transport voltages $V = (2n+1)e/C$, leading to the typical so called Coulomb staircase behavior of the transistor which is e.g. discussed in Ref. [70].

6.2 Molecular quantum dots

The field of molecular electronics was initiated by the pioneering work from Aviram and Ratner [71] in 1974 who introduced the idea of a molecular rectifier, although it was at this point far from being realized experimentally. Indeed it took twenty three more years, until first experiments on molecular junctions could be performed by Reed *et. al.* [58]. The main differences in the transport through conventional nanostructures and the transport through quantum dots consisting of a single molecule arise from the coupling of the electronic degrees of freedom to molecular vibrations.

In this section we will briefly introduce two of the consequences of this electron-vibron coupling on the transport, i.e. the development of vibrational sidebands (Section 6.2.1) and the Franck-Condon blockade (Section 6.2.2), and describe how it is possible to treat molecular quantum dots theoretically in the framework of the Anderson-Holstein Hamiltonian (Section 6.2.3).

6.2.1 Vibrational sidebands

The coupling to a vibrational mode provides low lying excited states (as indicated by the dotted lines in Figure 6.10) which can also contribute to the transport through the
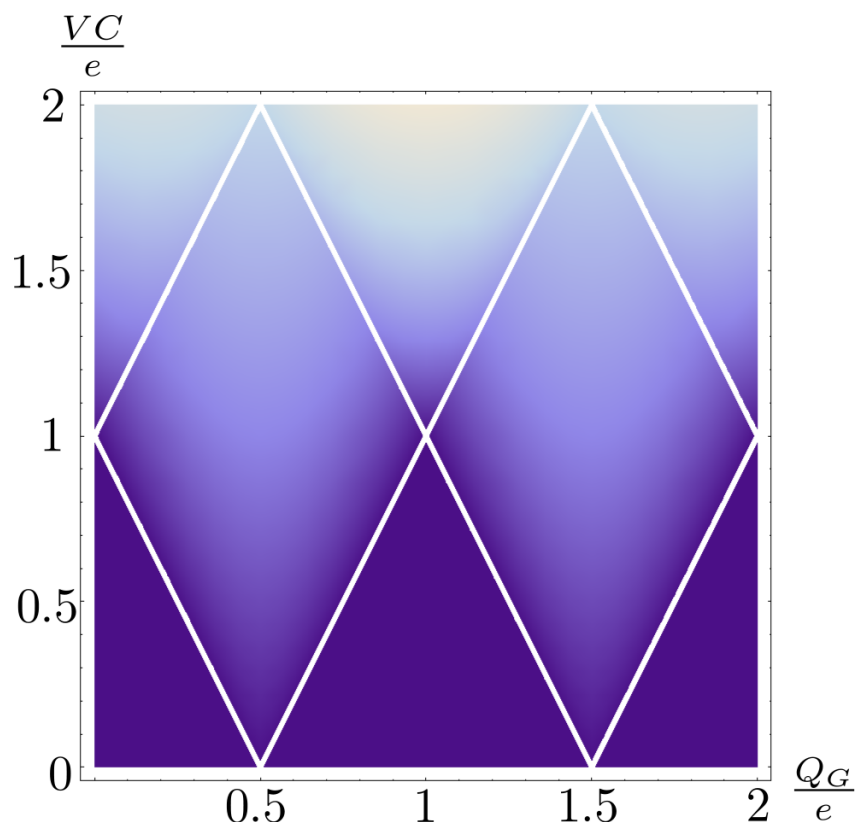
Figure 6.6: Density plot of the current in a symmetric single electron transistor at low temperatures and transport voltages. Lighter colors indicate higher current, and the Coulomb Diamonds which where already depicted in Figure 6.5, are indicated by white lines. As long as the transport voltage is low, $VC/e < 1$, only two charge states play a role, while more charge states are involved at higher transport voltages.

quantum dot. When an additional transition between two of these excited states or one excited states and the ground state becomes allowed, the current changes which leads to sidebands within the Coulomb blockade diamonds as indicated in Figure 6.7. Note, that these transitions are only allowed within the Coulomb diamonds, i.e. when the ground state transitions are allowed. This effect has been observed in a number of experiments [59, 72, 73, 74].

6.2.2 Franck-Condon blockade

The strong suppression of the sequential tunneling current at low bias voltage is referred to as Franck-Condon blockade [75, 76, 77]. Heuristically the effect arises due to the vibron-induced displacement of the potential surfaces (cf. Section 6.2.3) indicated in Figure 6.10 leading to a suppressed overlap of the low-lying vibrational states if this displacement is large compared to the quantum fluctuations (Figure 6.8). This causes a strong suppression of the current at low bias voltages which can not be lifted by changing the gate voltage as
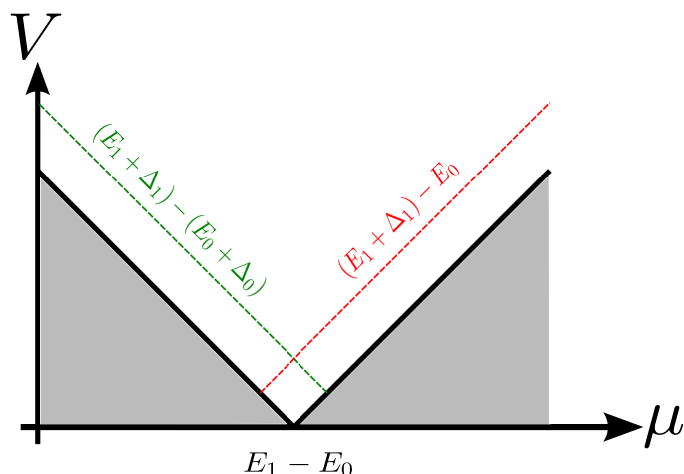
Figure 6.7: Sidebands due to transport through excited states in the μ-V-Diagram. The red dotted line indicates a transition from an excited state with energy $E_1 + \Delta_1$ to the ground state with energy E_0, the green line a transition between two excited stated and the bold black lines indicate transitions between ground states.

it is the case in the Coulomb blockade regime.

An additional crucial timescale in the Franck-Condon regime is the vibrational relaxation rate. Since just low lying vibrational states are blockaded it is obvious that the effect is more pronounced for fast vibrational relaxation. However, the effect still exists in the limit of slow vibrational relaxation [77].

Experimentally Leturcq *et. al.* [60] observed the Franck-Condon blockade in suspended carbon nanotubes. The longitudinal stretching mode of the nanotubes is coupled linearly to the electrons which leads to the appearance of a Franck-Condon blockaded regime in conductance measurements. In Figure 6.9 we depict experimental results as well as the corresponding theoretical predictions of Ref. [60], showing not only the suppression of the current at low bias voltages, but also the development of vibrational sidebands described in Section 6.2.1.

6.2.3   Model Hamiltonian – the Anderson-Holstein Hamiltonian

The system we want to analyze is a single electron transistor in which the metallic quantum dot is replaced by a single molecule. Thus two main differences compared to the considerations of the SET occur: First we assume that transport through the system is dominated by tunneling through only one spin degenerated electronic level, instead of the many levels of the metallic dot, and second we include the possibility of a single vibrational mode with frequency ω_0 coupled to the molecule. Due to the Coulomb interaction occupying the molecule with two excess electrons is possible, but costs an additional charging energy $U > 0$. We further keep the assumption, that the metallic leads stay in equilibrium at all times, i.e. that electronic relaxation in the leads is the shortest timescale in the system.

The natural starting point for an analytical discussion of the system is the so-called Anderson-Holstein Hamiltonian [56, 57, 78, 79, 80]. It consists of three parts, $H = H_{\mathrm{dot}} +$
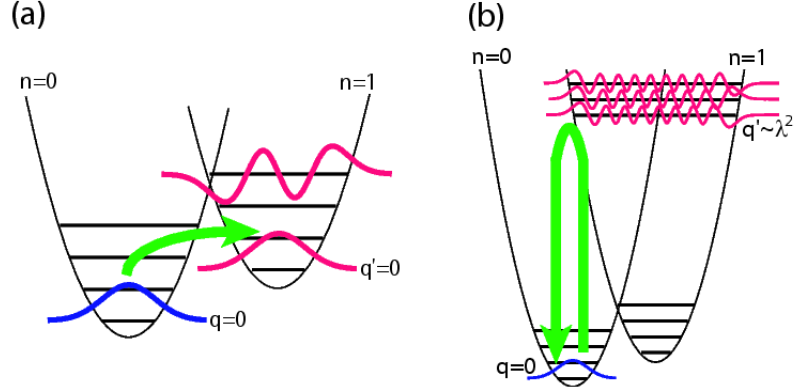
Figure 6.8: (a) Suppressed overlap of low-lying vibrational states. (b) Cotunneling processes partially lifting the suppression of the current in the Franck-Condon regime. Figure taken from [77].

$H_{\text{leads}} + H_{\text{tun}}$, where

$$H_{\text{dot}} = \epsilon_d n_d + U n_{d\uparrow} n_{d\downarrow} + \hbar\omega_0 b^\dagger b + \lambda\hbar\omega_0 (b^\dagger + b) n_d \qquad (6.25)$$

describes electronic and vibrational degrees of freedom on the molecular quantum dot as well as their coupling. The metallic leads are modeled by the Hamiltonian

$$H_{\text{leads}} = \sum_{\alpha=L,R} \sum_{\boldsymbol{p},\sigma} (\epsilon_{\boldsymbol{p}} - \mu_\alpha) c^\dagger_{\alpha,\boldsymbol{p}\sigma} c_{\alpha,\boldsymbol{p}\sigma} \,, \qquad (6.26)$$

and the tunneling Hamiltonian contains the two tunneling matrix elements t_L and t_R parameterizing the strength of the coupling between the dot and the left and right lead,

$$H_{\text{tun}} = \sum_{\alpha=L,R} \sum_{\boldsymbol{p},\sigma} t_\alpha c^\dagger_{\alpha,\boldsymbol{p}\sigma} d_\sigma + \text{h.c.} \,. \qquad (6.27)$$

Here the operator $n_{d,\sigma} = d^\dagger_{d,\sigma} d_{d,\sigma}$ is the number operator, counting the number of excess electrons on the dot, $d^\dagger_{d,\sigma}$, $d_{d,\sigma}$ are the creation and annihilation operators on the dot, and n_d stands for the spin resolved number operator, $n_d = \sum_\sigma n_{d,\sigma}$. The operators b and $b^\dagger$ annihilate and create a vibrational excitation with energy $\hbar\omega_0$, while the term $\lambda\hbar\omega_0 (d + d^\dagger) n_d$ describes the linear coupling of the electronic and the vibrational degrees of freedom on the dot, where the parameter λ parametrizes the coupling strength. Finally the operators $c_{\alpha\boldsymbol{p}\sigma}$ and $c^\dagger_{\alpha\boldsymbol{p}\sigma}$ denote the annihilation and creation operators on the left ($\alpha = L$) and right ($\alpha = R$) lead respectively.

It is assumed, that the leads consist of the same material, i.e. that they have the same band structure. We apply the wide-band limit, which means that we assume the energy range involved in transport to be small compared to the bandwidth of the conduction band of the leads, leading to an effectively constant density of states in the leads. The bias voltage can be modeled by fixing the chemical potentials of the dot, $\mu_L - \mu_R = eV$
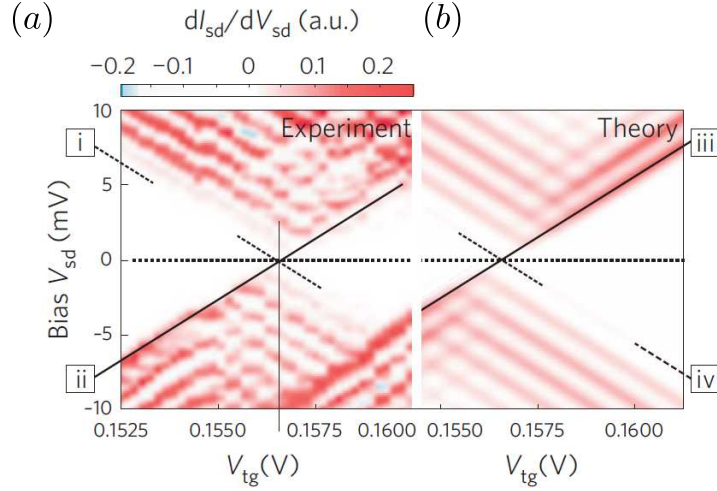
Figure 6.9: (a) Experimental data from Leturcq *et. al.* ([60]). One can see the suppression of the current at low bias voltage. (b) Numerical simulation of the Coulomb diamonds under the same conditions as the experimental data in (a). Figure taken from [60].

(compare to Eq. (B.7), first line). Since the bias voltage just defines the difference between the two chemical potentials we introduce a splitting parameter $0 \leq \eta \leq 1$ with $\mu_L = \eta eV$ and $\mu_R = (1 - \eta)eV$. The energy ϵ_d is the particle energy on the molecule which can be tuned by applying a gate voltage V_G. In the remainder of this section we will assume symmetric splitting $\eta = 1/2$, which can always be reached by changing the gate voltage.

The influence of the vibrational degrees of freedom can be enlightened by performing a canonical transformation which eliminates the coupling term in Eq. (6.25). The so-called Lang-Firsov transformation [81] map the Anderson-Holstein Hamiltonian to a Hamiltonian describing polaron quasiparticles in which the coupling between the quasiparticles and the vibration is absent. This mapping results in a change of the tunneling matrix elements and in the so called polaron shift – a renormalization of the charging energies ϵ_d and U. We present the transformation in Appendix B.3, and constrict ourselves to a qualitative argument at this point which will bring out the same results.

The vibrational part of the Anderson-Holstein Hamiltonian (6.25) reads

$$H_{\text{vibr}} = \hbar\omega_0 b^\dagger b + \lambda\hbar\omega_0(b + b^\dagger)n_d. \tag{6.28}$$

We switch to real space and momentum variables, $x = \frac{l_{\text{osc}}}{\sqrt{2}}(b + b^\dagger)$ and $p = \frac{\hbar}{i} \frac{1}{\sqrt{2}\,l_{\text{osc}}}(b - b^\dagger)$, yielding

$$H_{\text{vibr}} = \frac{p^2}{2m} + \frac{m\omega_0^2}{2}x^2 + \sqrt{2}\lambda\hbar\omega_0 \frac{x}{l_{\text{osc}}}n_d, \tag{6.29}$$

and complete the square in x

$$H_{\text{vibr}} = \frac{p^2}{2m} + \frac{\hbar\omega_0}{2}\left(\frac{x}{l_{\text{osc}}} + \sqrt{2}\hbar\omega_0 n_d\right)^2 - \lambda^2\hbar\omega_0 n_d^2. \tag{6.30}$$

We read off two consequences from this trivial rewriting: first the variable x in the harmonic oscillator is shifted by $\sqrt{2}\lambda n_d$, which means, that the potential minimum will vary with the occupation number n_d, and which will change the tunneling constants $t_{L/R}$. Second we see an additional energy shift. Rewriting this shift as

$$-\lambda^2\hbar\omega_0 n_d^2 = -2\lambda^2\hbar\omega_0 n_d(n_d-1)/2 - \lambda^2\hbar\omega_0 n_d\,, \qquad (6.31)$$

and comparing to the energy term $\epsilon_d n_d$ we can see, that the orbital one particle energy is shifted, $\epsilon_d \to \epsilon_d - \lambda^2\hbar\omega_0$. Further we can rewrite $U n_{d\uparrow} n_{d\downarrow} = U\frac{n_d(n_d-1)}{2}$ and see, that also the charging energy is renormalized, $U \to U - 2\lambda^2\hbar\omega_0$. From Appendix B.3 we read off, that the tunneling matrix elements are shifted as

$$t_{\alpha\boldsymbol{p}} \to t_{\alpha\boldsymbol{p}}\, e^{-\lambda(b^\dagger-b)} = t_{\alpha\boldsymbol{p}}\, e^{\sqrt{2}l_{\mathrm{osc}}\frac{d}{dx}}\,. \qquad (6.32)$$

which can be interpreted as a shift of the minimum potential surface in real space (see Figure 6.10). This shift originates from different equilibrium distances of the atoms in the molecular structure for different charge states [82] and is given by $\Delta x = \sqrt{2}\lambda l_{\mathrm{osc}}$, where $l_{\mathrm{osc}} = \sqrt{\hbar/M\omega_0}$ is the harmonic oscillator length. The potential surfaces of the Anderson-Holstein Hamiltonian for a spin degenerated electronic orbital are drafted in Figure 6.10.
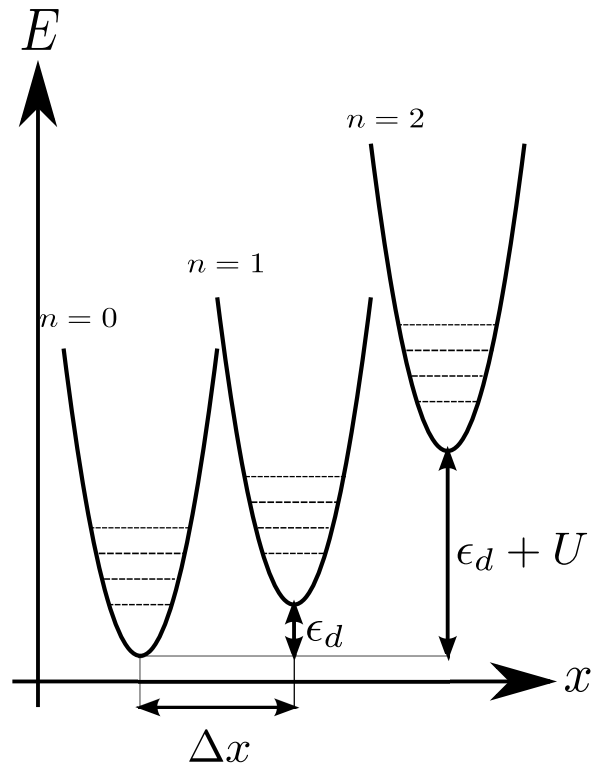
Figure 6.10: Sketch of the potential surfaces corresponding to the Anderson-Holstein Hamiltonian. Charging the molecule with one (two) electron(s) costs energy ϵ_d ($\epsilon_d + U$). The electron-phonon coupling causes a local shift of the potential surface by Δx each time an extra electron enters the molecule. The dotted lines indicate the ground state and the first excited states of the vibrational mode

Chapter 7

Negative-U regime

After sketching the aftermath of the shift in the tunneling matrix elements due to the coupling of a quantum dot to a vibrational degree of freedom, resulting in vibrational sidebands and the Franck-Condon blockade, we will concentrate on the influence of the polaron shift on the physical properties of the system in this section. As we have seen in Section 6.2.3 the electron-vibron coupling renormalizes the charging energy of the quantum dot. While in general a finite on-site interactions always opens the possibility of two electrons hopping on and off the quantum dot simultaneously, we will concentrate on the regime of an effectively negative charging energy, where hopping of two or more electrons at a time dominates the electronic transport.

The possibility of reaching a regime with effectively negative charging energy was first pointed out by Anderson in 1975 [83] who analyzed an attractive Hubbard model of localized states suitable for semi-conducting glasses which has no gap for two-electron excitations but an energy gap for one-electron ones. Ever since systems exhibiting a negative-U regime have been studied to some extend [10, 61, 84, 85, 86, 87, 88, 89, 90]. E.g. in chemistry molecules in the negative-U regime are known under the name "potential inversion [91]. In metallic quantum dots the negative-U regime can be reached if the electron vibron coupling is sufficiently strong, while indications of such a strong coupling e.g. in suspended carbon-nanotube quantum dots have been observed recently [60, 92, 93, 94, 95].

It has been shown recently that the negative-U regime opens the possibility for novel features such as an efficient electron pair tunneling through single molecules [10] and a charge-Kondo effect [61]. An underlying assumption of these works is that the negative charging energy does not induce an instability of the system. This is indeed the case when the energy gain due to the effectively attractive charging energy is smaller than the cost in single-particle energy due to the finite level spacing, when adding (removing) electrons to (from) the dot. This part of the thesis is devoted to study the opposite regime where the magnitude of the negative (renormalized) charging energy exceeds the single-particle level spacing. The studied system is modeled as a single-electron transistor (SET, see Section 6.1.2) whose center island is coupled to a mechanical vibration [59, 75, 92, 96, 97, 98]. It is shown that the system becomes unstable toward addition or extraction of electrons. Assuming that the vibron Hamiltonian contains an anharmonic contribution we show that the instability is regularized and that the system possesses a well-defined ground state. The effective charging energy as a function of the electron number in the dot has a double-well

structure which, moreover, depends on temperature. This is in striking contrast to the usual parabolic charging energy and leads to a variety of novel effects. At zero gate charge and low temperatures, there is a symmetry between particle-like and hole-like excitations causing the existence of degenerate minima of the effective charging energy. For a weak anharmonicity these are separated by a large number of electrons. The average population and the electron number fluctuations are highly sensitive to the gate voltage which breaks the symmetry between the minima. We also show that the transport properties of the system exhibit a number of distinctive features attributed to the unusual form of the effective charging energy.

The section is organized as follows. We will start (Section 7.1) by reviewing existing results on the negative-U regime in the case of a molecular quantum dot, i.e. if the level spacing is large compared to the absolute value of U [10, 61]. The model we use is introduced in Section 7.2, where we also demonstrate the origin of the negative-U instability, and state the precise conditions under which it takes place. In Section 7.3 we explore the equilibrium properties of the instability, including the effects of the vibron nonlinearity. Non-equilibrium (transport) properties in the presence of a bias voltage are discussed in Section 7.4. In Section 7.5 we argue that the system we analyze can eventually be realized experimentally in carbon nanotube quantum dots. We conclude in Section 7.6.

7.1 Negative-U in molecular quantum dots

As long as the absolute value of the charging energy is small compared to the level spacing, the transport is dominated by one single-particle orbital ϵ_d. When sweeping the gate voltage the ground state occupation of the molecule switches from empty to double occupied at the resonance condition $2\epsilon_d + U = 0$. Single occupation of the molecule is energetically unfavorable at all gate voltages. Thus we can conclude that also the transport through the system will be dominated by processes where two electrons hop on and off the dot simultaneously. To describe the transport through the system analytically we have to keep track of eight different pair-tunneling processes in total, including six processes where pairs of electrons tunnel on and off the molecule (two of them sketched in Figure 7.1 (b/c)) and two cotunneling processes [10] which are illustrated in Figure 7.1 (a).
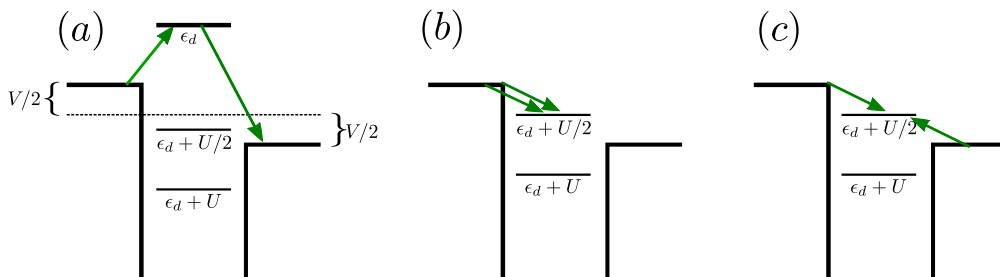
Figure 7.1: Schematic energy level configuration of the energies for the single (ϵ_d) and double ($\epsilon_d + U/2$) occupied dot as well as the energy for holes propagating through the double occupied dot ($\epsilon_d + U$). (a) Cotunneling process in which an electron propagates from the left lead to the right lead. (b) and (c) depict pair tunneling processes.

Assuming to be in a bias voltage and temperature regime where only the vibrational ground state is populated, the Hamiltonian of the system can be modeled as

$$H_{\text{eff}} = \epsilon_d \, n_d + U \, n_{d\uparrow} \, n_{d\downarrow} + H_{\text{leads}} + H_{\text{tun}} \,, \tag{7.1}$$

where we already absorbed the shifted energies and tunneling matrix elements due to the Lang-Firsov transformation in the definition and thus can assume U to be negative. The system can be treated analytically by performing a so-called Schrieffer-Wolff transformation [99, 100] which eliminates the tunneling Hamiltonian to first order, leading to the transformed Hamiltonian

$$H_{\text{SW}} = \epsilon_d \, n_d + U \, n_{d\uparrow} \, n_{d\downarrow} + H_{\text{leads}} + H_{\text{dir,ex}} + H_{\text{pair}} \,. \tag{7.2}$$

The first new term occurring after the Schrieffer-Wolff transformation describes the direct exchange interaction between molecule and leads, and occurs also in the positive-U-regime. It describes the single electron tunneling processes which dominate the transport in the positive-U regime and reads

$$H_{\text{dir,ex}} = \frac{1}{2} \sum_{\alpha\,\alpha'\,\boldsymbol{p}\,\boldsymbol{p}'\,\sigma} \left[\frac{t_\alpha \, t_{\alpha'}^*}{\epsilon_{\alpha\boldsymbol{p}} - \epsilon_d} \, c_{\alpha\boldsymbol{p}\sigma} c_{\alpha'\boldsymbol{p}'\sigma}^\dagger + t_\alpha \, t_{\alpha'}^* \, M(\epsilon_{\alpha\boldsymbol{p}}) \times \right.$$
$$\left. (d_{\bar{\sigma}}^\dagger d_\sigma c_{\alpha\boldsymbol{p}\sigma}^\dagger c_{\alpha'\boldsymbol{p}'\bar{\sigma}} - c_{\alpha\boldsymbol{p}\sigma}^\dagger c_{\alpha'\boldsymbol{p}'\bar{\sigma}} \, n_{d\bar{\sigma}}) + \text{h.c.} \right] \,, \tag{7.3}$$

where we introduced $M(\epsilon) = [\epsilon - \epsilon_d]^{-1} - [\epsilon - (\epsilon_d + U)]^{-1}$ and the notation $\bar{\uparrow}(\bar{\downarrow}) = \downarrow (\uparrow)$. In the negative-$U$ regime we also have to keep track of the pair-tunneling processes described by the last term in Eq. (7.2), which abbreviates

$$H_{\text{pair}} = \sum_{\alpha\,\alpha'\,\boldsymbol{p}\,\boldsymbol{p}'} t_\alpha t_{\alpha'} \, M(\epsilon_{\alpha\boldsymbol{p}}) \, d_\uparrow d_\downarrow \, c_{\alpha'\boldsymbol{p}'\downarrow}^\dagger c_{\alpha\boldsymbol{p}\uparrow}^\dagger + \text{h.c.} \,. \tag{7.4}$$

One can see immediately, that H_{pair} vanishes for zero effective charging energy U.

At this point one can calculate the tunneling rates for the tunnel processes indicated in Figure 7.1 in the golden rule approximation [10]. The rates for pair-tunneling processes arising from H_{pair} turn in a regime where single occupation of the dot is negligible ($|2\epsilon_d + U|$, $|eV|$, $k_B T \ll \epsilon_d$, $|\epsilon_d + U|$) and for symmetric voltage splitting out to be

$$\Gamma_{0\to2}^{aa'} = \frac{2\pi N_a(0) N_{a'}(0) |t_a|^2 |t_{a'}|^2}{\hbar} \, M^2(0) \, F[2\epsilon_d + U + eV_a + eV_{a'}] \,. \tag{7.5}$$

Here we have defined the function $F(\epsilon) = \epsilon/[\exp(\beta\epsilon) - 1]$, and $\Gamma_{0\to2}^{aa'}$ describes the rate of the process where an electron with spin up originating from lead a and one with spin down originating from lead a' enter the dot, and thus change the dot occupation from zero to two. The rates $\Gamma_{2\to0}^{aa'}$ for electron pairs leaving the dot differ just by an overall minus sign in the argument of $F(\epsilon)$.

From Eq. (7.5) one can immediately deduce several features of the pair tunneling process. First we note, that only pair tunneling with electrons originating from the same lead (Figure 7.1(c); $a = a'$ in Eq. (7.5)) leads to rates depending on the bias voltage, while

for pair tunneling of electrons from different leads the bias voltage dependence drops out. The rate of the pair tunneling, if allowed energetically, is proportional to the energy of the pair state $2\epsilon_d + U$[1]. This can be explained by the fact, that only the sum of the energy of the two electrons involved in the pair tunneling process is fixed by energy conservation – in contrast to the single particle sequential tunneling, where the energy of the electron is fixed (cf. Eq. (6.9)). This leads to a phase space whose size is proportional to $2\epsilon_d + U$.

The rates for cotunneling in the same regime turn out to be

$$\Gamma_{0\to0}^{aa'} = 2\, \frac{2\pi N_a(0)N_{a'}(0)|t_a|^2|t_{a'}|^2}{\hbar}\, \frac{F(eV_a)}{\epsilon_d^2}\,,\text{ and}$$

$$\Gamma_{2\to2}^{aa'} = 2\, \frac{2\pi N_a(0)N_{a'}(0)|t_a|^2|t_{a'}|^2}{\hbar}\, \frac{F(eV_a)}{(\epsilon_d + U)^2}\,, \tag{7.6}$$

where a factor of two for spin degeneracy was included.

The stationary master equation reduces in this regime to

$$0 = P_2\Gamma_{2\to0} - P_0\Gamma_{0\to2}\,, \tag{7.7}$$

where we introduced the total rates for transitions from state i to state f, $\Gamma_{i\to f} = \sum_{a,a'}\Gamma_{i\to f}^{a,a'}$. Including the normalization of the probabilities, $P_2 = 1 - P_0$, we can solve Eq. (7.7), leading to

$$P_0 = \frac{\Gamma_{2\to0}}{\Gamma_{2\to0} + \Gamma_{0\to2}}\,. \tag{7.8}$$

The current can now be calculated as in Section 6.1.3. We distinguish between the current arising from pair tunneling[2],

$$I_{\text{pairs}}/e = P_0\left[2\Gamma_{0\to2}^{LL} + \Gamma_{0\to2}^{LR} + \Gamma_{0\to2}^{RL}\right] - P_2\left[2\Gamma_{2\to0}^{LL} + \Gamma_{2\to0}^{LR} + \Gamma_{2\to0}^{RL}\right]\,, \tag{7.9}$$

and the cotunneling current, which takes the form

$$I_{\text{cot}}/e = P_0\left[\Gamma_{0\to0}^{LR} - \Gamma_{0\to0}^{RL}\right] + P_2\left[\Gamma_{2\to2}^{LR} - \Gamma_{2\to2}^{RL}\right]\,. \tag{7.10}$$

Linearizing the current in the symmetric bias voltages $V_L = -V_R = V/2$ leads to the expression for the linear conductance, dI/dV,

$$G = \frac{2e^2\Gamma_L\Gamma_R}{h}\left[\frac{U^2}{\epsilon_d^2(\epsilon_d + U)^2}\frac{\beta(2\epsilon_d + U)}{2\sinh[\beta(2\epsilon_d + U)]} + \frac{f(-2\epsilon_d - U)}{\epsilon_d^2} + \frac{f(2\epsilon_d + U)}{(\epsilon_d + U)^2}\right] \tag{7.11}$$

which is plotted in Figure 7.2. One can see, that the linear conductance is composed of a featureless background resulting from the cotunneling contributions and a pair-tunneling induced peak of height and width $\sim T$.

---

[1]To be more exact one should say, that the rate is proportional to the detuning of the pair state from the Fermi energy which is set to zero.

[2]As in Section 6.1.3 we calculate the current between the left lead and the dot, which is for symmetric transport voltages equal to the total current.
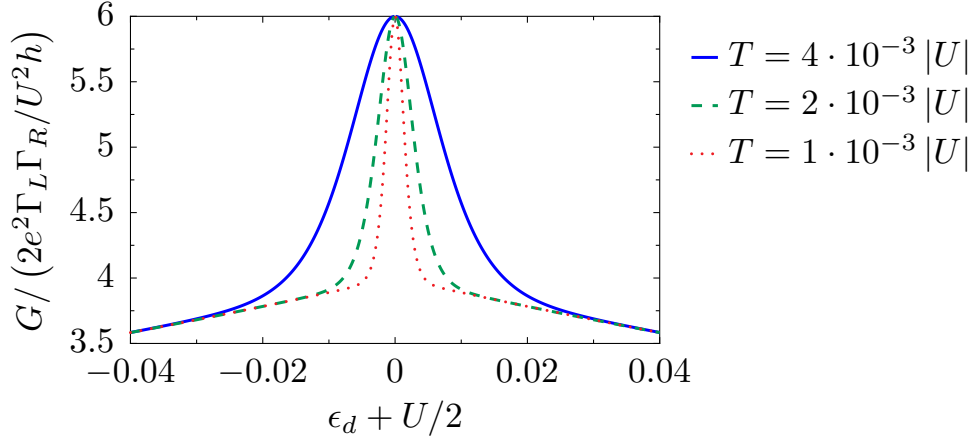
Figure 7.2: Linear conductance of a molecular quantum dot in the negative-U regime for different temperatures. The figure resembles [10, Fig. 2].

While it turns out that the linear conductance stays in the same form for asymmetric bias voltages, the current, i.e. the finite-bias behavior, still depends on this symmetry. We abbreviate the discussion of the calculation of the current at this point and instead show the results of Ref. [10] in Figure 7.3. In the symmetric case one can see that, in contrast to the Coulomb blockade regime, the conductance peak lies at zero gate voltage and its width is determined by the bias voltage. In the asymmetric case, Figure 7.3(b), we observe an asymmetry with respect to voltage inversion. Due to this feature asymmetric molecular quantum dots in the negative-U regime can be use as rectifiers, as it is argued in Ref. [10].
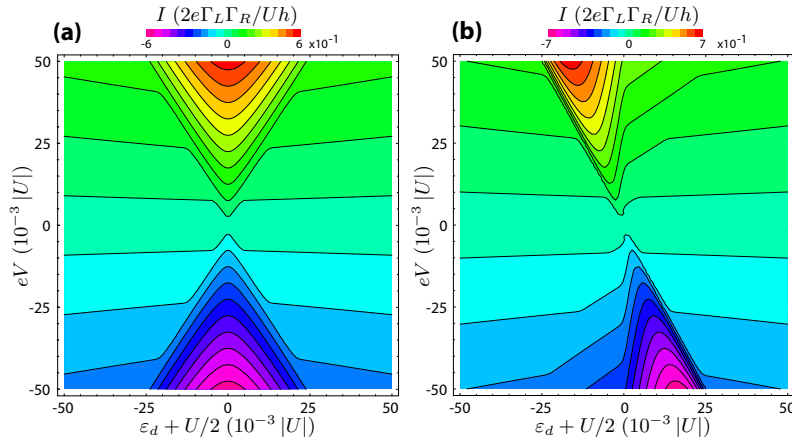
Figure 7.3: Color plot of the current dependence on bias and gate Voltage for (a) a symmetric junction, $\Gamma_L = \Gamma_R = k_B T$ and (b) an asymmetric junction with $\Gamma_L = 0.1 \, k_B T$ and $\Gamma_R = 10 \, k_B T$. Figure taken from [10].

95

7.2 Model and negative-U instability
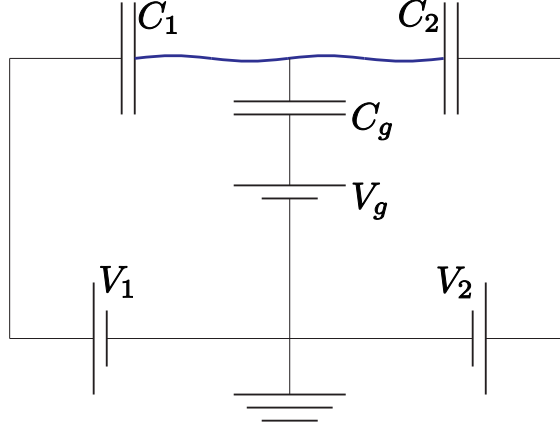
Figure 7.4: Equivalent circuit of the quantum dot. Capacitances C_1 and C_2 model high resistance tunnel junctions which allow the island to exchange electrons with the reservoirs, C_g represents a gate capacitance. The central part is coupled to a vibrational mode.

We are considering a quantum dot or a single-molecule junction coupled to a single vibrational degree of freedom. The dot is modeled as a SET where the number of electrons on the island couples to a vibron mode, see Figure 7.4. The system could be realized, for example, by a suspended center element between large metallic leads enabling tunneling between the dot and the leads. The electronic part of the Hamiltonian for a SET is

$$H_{\mathrm{e}} = \sum_{\mathrm{L,R,C}} \epsilon_j c_j^\dagger c_j + H_{\mathrm{T}} + U(N), \tag{7.12}$$

where the first term represents the single-particle energies of the leads and the center part, the second term describes tunneling between the leads and the center, and the last term is the relevant charging energy of the system. The tunneling Hamiltonian and the charging energy take the standard forms

$$H_{\mathrm{T}} = \sum_{i \in \mathrm{C},\, j \in \mathrm{L/R}} \left(t_{ij} c_i^\dagger c_j + t_{ij}^* c_j^\dagger c_i \right), \tag{7.13}$$

and

$$U(N) = \frac{(Ne - Q_g)^2}{2C}, \tag{7.14}$$

respectively. Here, $N = \sum_{\mathrm{C}} c_j^\dagger c_j - N_0$ is the number of excess electrons on the island, $C = C_1 + C_2 + C_g$, and $Q_g = V_1 C_1 + V_2 C_2 + V_g C_g$ is the total induced gate charge. The number N_0 corresponds to the positively charged lattice ions on the central island. The full Hamiltonian of the system, $H = H_{\mathrm{e}} + H_{\mathrm{ph}}$, also includes the vibrational contribution

$$H_{\mathrm{ph}} = \frac{P^2}{2M} + \frac{1}{2} M \Omega^2 x^2 + \alpha (2M\Omega^2)^2 x^4 + \lambda \, \hbar\Omega \, N \frac{x}{l_{\mathrm{osc}}}, \tag{7.15}$$

96

where we have included the electron-vibron coupling $\lambda\,\hbar\Omega\,Nx/l_{\text{osc}}$ with $l_{\text{osc}} = \sqrt{\hbar/2M\Omega}$ into the phonon Hamiltonian. The Hamiltonian (7.15) also includes an anharmonic x^4 term whose strength is controlled by the parameter α.

The anharmonic term becomes comparable to harmonic effects when the phonon displacement is of the order of $(\alpha\hbar\Omega)^{-2}$ times the oscillator length l_{osc}. The inclusion of this term, even in the weakly nonlinear case $\alpha\,\hbar\Omega \ll 1$, is crucial for the stability of the system for large couplings λ. To demonstrate this let us first assume $\alpha = 0$ and examine the phonon-induced modification of the charging energy. Since the electron number couples linearly to the phonon position, it is possible to introduce a shifted phonon coordinate by completing the square in the phonon Hamiltonian. As a result one eliminates the coupling term and generates an extra term $\Delta U(N)$ quadratic in N, leading to the effective charging energy

$$U^{\text{eff}}(N) = U(N) + \Delta U(N) = \frac{(Ne - Q_g)^2}{2C} - N^2\lambda^2\hbar\Omega. \tag{7.16}$$

It is important to recognize that the well-known polaron shift $\Delta U(N)$ gives rise to a *negative* contribution. The overall prefactor of the N^2-term will be negative if

$$\gamma = \frac{e^2}{2C} - \lambda^2\hbar\Omega < 0, \tag{7.17}$$

meaning that the effective potential favors large absolute values of N. Defining the quantity $E_{\text{ch}} = e^2/2C$, the negative charging energy condition (7.17) takes the form

$$\lambda > \sqrt{\frac{E_{\text{ch}}}{\hbar\Omega}}. \tag{7.18}$$

Consequently, in metallic quantum dots with a vanishingly small single-particle level separation, the energy can always be lowered by adding or removing an arbitrary number of particles when condition (7.18) holds. Thus the system does not possess a ground state and is unstable. In dots whose orbital energies due to confinement are not negligible compared to the charging and vibron energies, the single-particle energy cost should also be taken into account. To analyze this, we introduce equidistant single-electron orbitals

$$E_n = \hbar\,v_{\text{F}}\frac{n\pi}{L_d} = \Delta n, \tag{7.19}$$

where v_{F} is the Fermi velocity of the dot, L_d is the effective size of the electronic confinement and $\Delta = \hbar v_{\text{F}}\pi/L_d$ is the level separation. Expression (7.19) is appropriate in the vicinity of the Fermi energy and holds exactly for a one-dimensional Dirac spectrum. The energy cost of adding or removing N electrons to or from the lowest available orbitals (ignoring the spin degeneracy) is

$$\sum_{n=1}^{N} E_n = \Delta\frac{N(N+1)}{2}. \tag{7.20}$$

Adding the single-particle contribution to the effective potential (7.16) we get

$$U^{\text{eff}}(N) = \Delta\frac{N(N+1)}{2} + E_{\text{ch}}(N - Q_g/e)^2 - N^2\lambda^2\hbar\Omega$$

$$= \left(\frac{\Delta}{2} + E_{\text{ch}}\right)(N - Q_g/e)^2 - N^2\lambda^2\hbar\Omega + \text{const}, \tag{7.21}$$

where the second line follows by shifting the gate charge $Q_g \to Q_g + \frac{\Delta}{2E_{ch}}(\frac{e}{2} + Q_g)$. The constant in Eq. (7.21) is independent of N and can be dropped. Thus the functional form of the effective potential remains invariant, and the finite level separation just renormalizes charging energy and gate charge. The system is still fundamentally unstable provided that

$$\lambda > \sqrt{\frac{E_{ch} + \Delta/2}{\hbar\Omega}}. \tag{7.22}$$

In the spin-degenerate case Δ should be replaced by $\Delta/2$. Alternatively, we can write this condition as $E_{ch} - \lambda^2\hbar\Omega < -\Delta/2$, i.e., we find an instability when the magnitude of the renormalized charging energy becomes larger than the level spacing.

Result (7.22) shows that a constant (or decreasing) level spacing is not adequate to stabilize the system at sufficiently large couplings. The instability tends to change the electron number by increasing the displacement of the phonon mode. Therefore it is natural to assume that at some point when the displacement becomes large the harmonic approximation for the vibron mode breaks down and anharmonic effects become significant. It turns out that a generalization of the above analysis to include a nonzero anharmonic term ($\alpha > 0$) in Eq. (7.15) always produces a well-defined ground state. The effective potential for electrons becomes temperature dependent and exhibits a variety of novel features.

Our discussion has a close relation to familiar stability conditions in Fermi-liquid theory [101]. In fact, it is well known that the Fermi liquid remains stable even when the Landau interaction parameter F_0 becomes negative as long as $F_0 > -1$. Since F_0 measures the interaction strength in units of the density of states, this is a precise analog of the stability condition (7.22) expressed as $(E_{ch} - \lambda^2\hbar\Omega)/(\Delta/2) > -1$[3].

7.3 Thermal equilibrium properties

7.3.1 Effective potential

In this section we study effects of the anharmonic phonon term on the negative-U instability, focusing on thermal equilibrium properties of the junction. Diagonalizing (7.15) one obtains phononic eigenvalues $\{E_j(N)\}$ as a function of the electron number N and the island partition function becomes[4]

$$Z = \sum_{N,j} \exp\{-\beta[U(N) + E_j(N)]\}$$

$$= \sum_N \exp\{-\beta U(N)\} \sum_j \exp\{-\beta E_j(N)\}. \tag{7.23}$$

In Eq. (7.23) we have assumed that the electron tunneling is weak and its contribution to the partition function is negligible compared to the charging energy[5]. Defining a phononic

---

[3]The quantity $(E_{ch} - \lambda^2\hbar\Omega)/(\Delta/2)$ corresponds to F_0 apart the difference of factor two which can be readily traced to trivial differences in definitions.

[4]For simplicity, we present our analysis in the case $\Delta = 0$. A nonzero Δ can be readily included by a simple renormalization of E_{ch} and Q_g.

[5]Tunneling is still important in the sense that in the equilibration process the island can change its charging state by exchanging electrons with the leads.

partition function as $Z_{\mathrm{ph}}(N) = \sum_j \exp\{-\beta E_j(N)\}$, the partition function takes the form

$$
\begin{aligned}
Z = \; & Z_{\mathrm{ph}}(N = 0) \\
& \times \sum_N \exp\left\{-\beta[U(N) - \frac{1}{\beta}\ln\left(Z_{\mathrm{ph}}(N)/Z_{\mathrm{ph}}(N = 0)\right)]\right\}.
\end{aligned}
\tag{7.24}
$$

From expression 7.24 one can identify the effective electronic potential

$$
U^{\mathrm{eff}}(N, T) = U(N) - \frac{1}{\beta}\ln\left[Z_{\mathrm{ph}}(N)/Z_{\mathrm{ph}}(N = 0)\right].
\tag{7.25}
$$

In the absence of the electron-phonon interaction, Eq. (7.25) reduces to the ordinary charging energy, and in the absence of the anharmonic term ($\alpha = 0$) it is temperature independent and coincides with expression (7.16). In the anharmonic case the polaron shift depends on the phonon state and thus the effective potential depends on the phonon temperature. In general, an evaluation of Eq. (7.25) requires one to diagonalize (7.15) numerically and to compute the phonon partition function. The behavior of the system is then determined by the relative strength of the energy scales E_{ch}, $\hbar\Omega$, α^{-1}, and the magnitude of dimensionless electron-phonon coupling λ.

7.3.2 Analytical considerations

Analytical expressions for the effective potential can be obtained for weakly unstable systems at zero temperature when considering the vibronic degree of freedom as classical. As this already illustrates some of the essential physics, we first consider this case before presenting more general numerical results for the fully quantum mechanical model.

Starting with equation (7.25), we can write the effective potential at zero temperature as

$$
U^{\mathrm{eff}}(N) = U(N) + E_0(N) - E_0(0),
\tag{7.26}
$$

where $E_0(N)$ denotes the ground state energy of the phonon Hamiltonian H_{ph} for excess charge N. In the classical limit, the ground state energy is simply given by the minimum of the potential energy. Noting that $E_0(0)$ vanishes, we obtain

$$
\begin{aligned}
U^{\mathrm{eff}}(N) = \; & U(N) - \lambda^2\hbar\Omega N^2 \\
& + \min_x\{\frac{1}{2}M\Omega^2(x + 2\lambda N\ell_{\mathrm{osc}})^2 + \alpha(2M\Omega^2)^2 x^4\}.
\end{aligned}
\tag{7.27}
$$

For a weakly unstable system near zero gate charge, we expect that the effective potential has a minimum for small (but nonzero) N. Thus, we can neglect the quartic term when determining the position of the minimum in equation (7.27),

$$
x_0 \simeq -2\hbar\Omega N.
\tag{7.28}
$$

It is straightforward to include corrections to this expression and find that this approximation is valid as long as $\lambda^2|E_{\mathrm{ch}} - \lambda^2\hbar\Omega|/\hbar\Omega \ll 1$, i.e., as long as the instability is only weakly developed. With this expression for x_0, we find for the effective potential

$$
U^{\mathrm{eff}}(N) = U(N) - \lambda^2\hbar\Omega N^2 + 16\alpha(\hbar\Omega)^2 N^4.
\tag{7.29}
$$

Focusing on the case of zero gate charge, we can now compute the number of electrons N_0 which are entering the quantum dot as a consequence of the instability. Minimizing the effective potential in equation (7.29), we find

$$N_0^2 = \frac{|E_{\mathrm{ch}} - \lambda^2 \hbar\Omega|}{32\alpha(\hbar\Omega)^2}. \tag{7.30}$$

Note that there are indeed degenerate minima at $N = \pm N_0$ for zero gate charge.

Once the instability develops, we can define an effective charging energy $E_{\mathrm{ch}}^{\mathrm{eff}}$ which describes the curvature of the effective potential in the vicinity of the minima. Expanding equation (7.29) around the minima, we find

$$E_{\mathrm{ch}}^{\mathrm{eff}} = 2|E_{\mathrm{ch}} - \lambda^2\hbar\Omega| \tag{7.31}$$

This sign reversal of the effective charging energy induced by the instability has important consequences. While a negative renormalized charging energy leads to pair tunneling in the absence of the instability [75], the positive effective charging energy $E_{\mathrm{ch}}^{\mathrm{eff}}$ implies that transport will be dominated again by single electron sequential tunneling processes once the instability develops. It is also interesting to note that the Coulomb blockade is significantly weakened near the instability where many charge states have similar energies.

We close this section with a remark on the validity of the classical approximation for the vibrons employed in this section. As can be readily seen from equation (7.26), the quantum-mechanical zero-point energy of the vibron mode cancels out from this expression as long as the vibron remains harmonic, implying that the zero-point energy is independent of the electron number N. Thus, quantum corrections to our classical discussion are proportional to the anharmonicity and our classical expressions are an excellent approximation to the results of a fully quantum mechanical calculation as long as the anharmonicity remains small (see Section 7.3.3 for a comparison with numerical results).

7.3.3 Numerical results

A solution of the full quantum problem for arbitrary parameter values requires a numerical approach. We now focus on the results of such a calculation. Figure 7.5 illustrates the dependence of the effective potential on the electron-phonon coupling strength and the charging energy. As the coupling strength is increased the system exhibits a crossover between the $\gamma > 0$ regime and the negative-U regime $\gamma < 0$, signaled by the formation of a double-well structure. Decreasing the (bare Coulomb) charging energy results in qualitatively similar behavior as increasing the coupling strength.

Figure 7.6 shows the temperature dependence of a typical effective charging curve $U^{\mathrm{eff}}(N, T)$ in the negative-U regime $\gamma < 0$. At low temperatures the potential exhibits a double-well structure whose details depend on the particular parameter values. The shape of the potential can also change qualitatively as the temperature is increased: the double well structure present in Figure 7.6 is eventually deformed to a single-well potential. The temperature dependence of the potential is a consequence of the nonlinear phonon interaction. In the asymmetric case (i.e., at nonzero gate charge $Q_g \neq 0$) there exists a metastable energy minimum whose decay towards the global minimum requires multiple
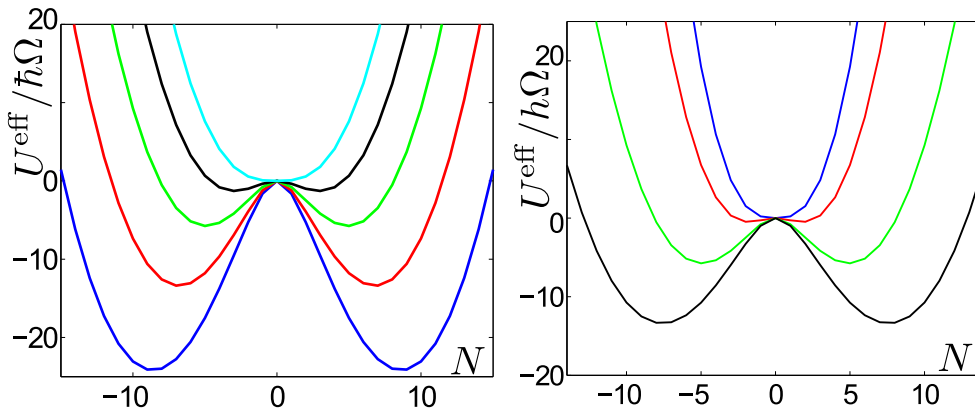
Figure 7.5: Effective potential as a function of the electron number. Left: the coupling-dependence of the potential, $T = 0.1\,\hbar\Omega$, $\alpha = 0.01$, $E_{\mathrm{ch}} = \hbar\Omega$, $Q_g = 0$ and from bottom to top $\lambda^2 = 3, 2.5, 2, 1.5, 1$. Right: the effective potential corresponding to different charging energies, $\alpha = 0.01(\hbar\Omega)^{-1}$, $\lambda^2 = 2$, $T = 0.1\,\hbar\Omega$, $Q_g = 0$, and from bottom to top $E_{\mathrm{ch}} = 0.5, 0.8, 1, 1.5, 2 \times \hbar\Omega$.

electron tunneling (roughly 10 electrons for the parameter values). Figure 7.7 (left) shows a comparison between the full quantum mechanical solution obtained numerically and the classical result obtained in Section 7.3.2. As argued above, we find that the classical approximation is quite accurate for small anharmonicity. The wells are closer at stronger anharmonicity and higher temperature, as indicated by Figure 7.7 (right).

The average number of electrons as a function of the gate charge is presented in Figure 7.8. In the absence of the electron-phonon coupling and at low temperatures, the average number $\langle N \rangle$ exhibits the usual Coulomb staircase behavior. As the coupling is increased, this is gradually transformed into a new dependence reflecting the double-well nature of the effective potential. The double-well structure leads to a rapid increase of the population at low gate charges. The reason for this is that the gate acts as a symmetry breaking field and the values $Q_g/e \gtrsim k_{\mathrm{B}}T/E_{\mathrm{ch}}$ are sufficient for the system to prefer one of the two nearly degenerate wells.

This physics is also clearly reflected in the average number $\langle N \rangle$ as function of temperature, as shown for various gate charges in Figure 7.9. For finite positive gate charge the zero temperature average value corresponds to the minimum of the right well. As the gate charge increases, the position of the minimum shifts and electrons are added to the dot in discrete jumps of one electron. At higher temperatures, the system is no longer trapped in the right well so that the average number of electrons decreases rapidly. However, the average number saturates at a finite value at high temperatures, reflecting the gate-induced asymmetry of the potential.

Charge fluctuations also exhibit interesting behaviors. In the absence of the electron-phonon interaction the electronic potential is $U(N) = E_c(N - Q_g/e)^2$, so the mean square
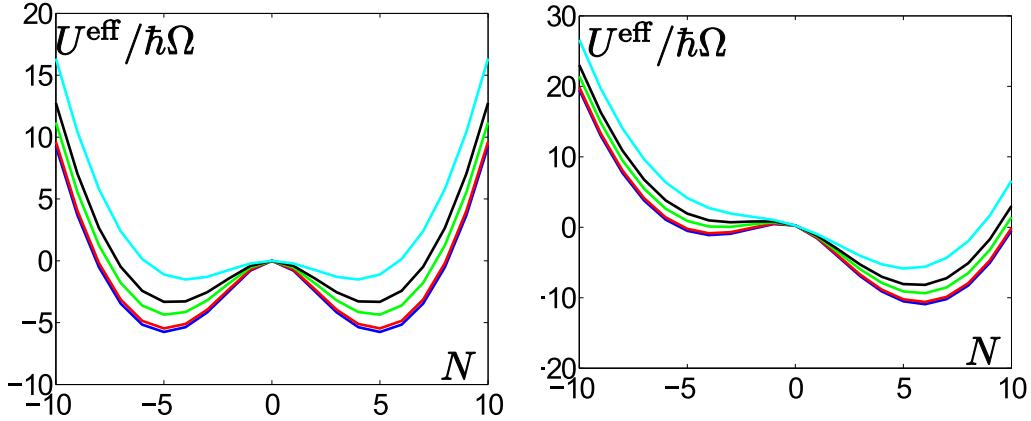
Figure 7.6: Effective potential as a function of the electron number. Left: Curves illustrate the temperature dependence of the potential corresponding to parameters $E_{\mathrm{ch}} = \hbar\Omega$, $\alpha = 0.01(\hbar\Omega)^{-1}$, $\lambda^2 = 2$, $Q_g = 0$ at $T = 0.1, 3, 5, 10 \times \hbar\Omega$ (from bottom to top). Right: The same as the left figure but at finite gate charge $Q_g = e/2$.

number fluctuation,

$$\Delta N^2 = \langle N^2 \rangle - \langle N \rangle^2 \,, \tag{7.32}$$

is proportional to temperature, $\Delta N^2 \propto T$. The situation is very different when the electrons couple to an anharmonic vibron mode. First of all, the zero-temperature number fluctuations do not vanish at zero gate charge, $Q_g = 0$, but saturate to a finite value, see Figure 7.10. This happens because there exist symmetric minima on both sides of the origin. The curve also exhibits a weak dip at finite temperatures since charge fluctuates more frequently towards values smaller than the charge at the minima. Eventually fluctuations grow due to the population of higher energy states. At finite gate values $Q_g \neq 0$ the fluctuations are drastically modified at low temperatures. The symmetry between the minima is broken and only states close to the preferred minimum are populated. When there is a single global minimum, the fluctuations vanish at zero temperature. At finite gate charge the curves approach to the zero gate curve at finite temperatures. At small gate charges, even a weak thermal excitation is sufficient to restore an approximate symmetry between the minima, leading to a sharp increase of the fluctuations from zero to the symmetric value at $Q_g = 0$.

7.4 Transport properties

So far we have explored consequences of the negative-U and the anharmonic phonon effects on equilibrium properties. In this section we focus on non-equilibrium characteristics of the system in the negative-U regime. To simplify the analysis we assume a continuous density of states of the dot and that the energy scales separate $\hbar\Omega \gg E_{\mathrm{ch}}$ so that only the lowest vibrational state $|E_0(N)\rangle$ is relevant at low temperatures and bias voltages. As
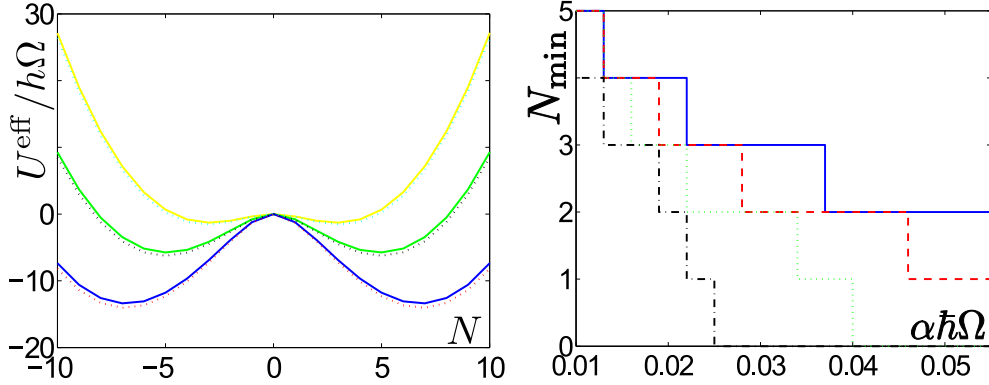
Figure 7.7: Left: Comparison of the classical and quantum mechanical effective potentials. Solid curves correspond to the quantum mechanical calculation with parameters $E_{ch} = \hbar\Omega$, $\alpha = 0.01\,(\hbar\Omega)^{-1}$, $Q_g = 0$, $T = 0$ and $\lambda^2 = 2.5$ (blue), $\lambda^2 = 2.0$ (green), $\lambda^2 = 1.5$ (yellow). The dotted lines correspond to the classical approximation obtained by minimizing the phonon potential energy. Right: Electron number corresponding to the minimum of the right potential well as a function of the nonlinearity, $E_{ch} = \hbar\Omega$, $\lambda^2 = 2$, $Q_g = 0$ and $T = 0.1\,\hbar\Omega$ (solid), $T = 3\,\hbar\Omega$ (dashed), $T = 5\,\hbar\Omega$ (dotted) and $T = 10\,\hbar\Omega$ (dash-dotted).

implied by considerations in Section 7.3 and the estimate for the effective charging energy Eq. (7.31), close to the instability the curvature of the potential is weak and one expects the sequential tunneling processes to dominate the transport. In the lowest order of the tunneling coupling transport properties are described by a rate equation with Golden-Rule transition rates [102]. Rates for the processes in which the initial dot state contains N electrons and where the electron number changes by one due to the tunneling through the left/right junction are

$$\Gamma_{N\pm1,N}^{L/R} = \gamma^{L/R} f\left(U^{eff}(N \pm 1) - U^{eff}(N) \pm \mu_{L/R}\right), \tag{7.33}$$

where $f(x) = \frac{x}{e^{\beta x}-1}$, $\gamma^{L/R} = \frac{|\langle E_0(N\pm1)|E_0(N)\rangle|^2}{e^2 R_t}$ and $1/R_t = \frac{4\pi e^2 |t|^2 \nu_{L/R}\nu_C}{\hbar}$. In the positive-$U$ regime in the absence of the anharmonic term the matrix element $|\langle E_0(N \pm 1)|E_0(N)\rangle|^2$ leads to the usual Franck-Condon suppression of the conductance given by $|\langle E_0(N \pm 1)|E_0(N)\rangle|^2 = e^{-\lambda^2}$. The probability $P(N)$ of having N extra electrons on the dot follows from the detailed balance condition $\Gamma_{N-1,N}P(N) = \Gamma_{N,N-1}P(N-1)$, where the rates Γ are given by the sum of the corresponding left and right lead rates. The stationary current through the SET can then be calculated from the expression

$$I = -e \sum_N \left(\Gamma_{N+1,N}^L - \Gamma_{N-1,N}^L\right) P(N). \tag{7.34}$$

In Figure 7.11 we have plotted the current as a function of the gate charge at different temperatures and bias voltages. The current is normalized to the Franck-Condon suppressed tunneling current $I_0 = e^{-\lambda^2}\hbar\Omega/eR_t$. At temperatures $T \gtrsim E_{ch}/2$ current is a

103
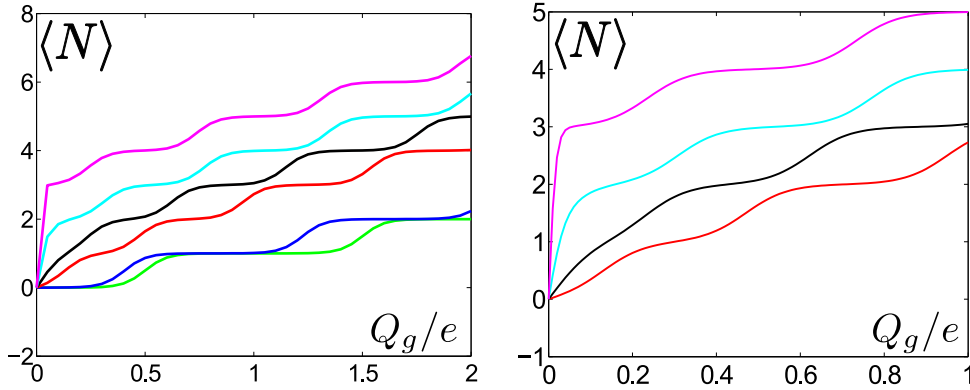
Figure 7.8: Average dot population as a function of the gate charge. The left figure corresponds to parameters $T = 0.1\,\hbar\Omega$, $\alpha = 0.01(\hbar\Omega)^{-1}$, $E_{\mathrm{ch}} = \hbar\Omega$ and from bottom to top $\lambda^2 = 0, 0.2, 0.8, 1, 1.2$ and 1.5. At vanishing coupling ($\lambda = 0$) we recover the usual Coulomb steps, in the strong coupling we have a rapid increase at low gate voltages. The right figure clarifies the small gate charge region for couplings $\lambda^2 = 0.8, 1, 1.2, 1.5$ (from bottom to top).

slowly varying function of the gate charge. Below this temperature it gradually starts to show signatures of Coulomb-like oscillations which become pronounced at low temperatures. Although this is in qualitative agreement with the standard Coulomb blockade results in absence of the vibron interaction there are also some essential differences. All the curves exhibit a slowly decreasing tendency and the amplitude of current oscillations grow as a function of gate charge. The strict periodicity of the usual Coulomb-blockade conductance is broken by the nonlinear phonon interaction which does not leave the effective charging spectrum invariant as Q_g is increased by multiples of the electron charge. Figure 7.11 (right) shows also that, within a reasonable accuracy, the current is a linear function of the applied voltage at low bias.

It is noteworthy that the current is not completely blocked even at relatively low temperatures $T \sim 0.1\,E_{\mathrm{ch}}$ where the usual Coulomb-blockade current is completely suppressed around integer gate charges. The reduction of the blockade can be qualitatively understood by considering the estimate (7.31), which indicates that in the vicinity of the instability the value of the effective charging is reduced. With parameters corresponding to Figures 7.11 and 7.12 the minima of the double-well potential are flatter than the minima corresponding to the bare electronic potential in the absence of vibrations and, as illustrated in Figure 7.12, there exist two (and at weaker nonlinearity more) almost degenerate states in each well. Transitions between these closeby states at the bottom of the wells enable current to flow below temperatures where the bare electronic energy cost would block it. The estimate for the effective charging (7.31) is valid only in the vicinity of the instability and by increasing $|E_{\mathrm{ch}} - \lambda\hbar\Omega|$ one eventually enters deep in the negative-U region where the curvature at the potential minimum exceeds E_{ch}. In this region the blockade is stronger than the usual Coulomb blockade and one has to consider higher-order tunneling processes.
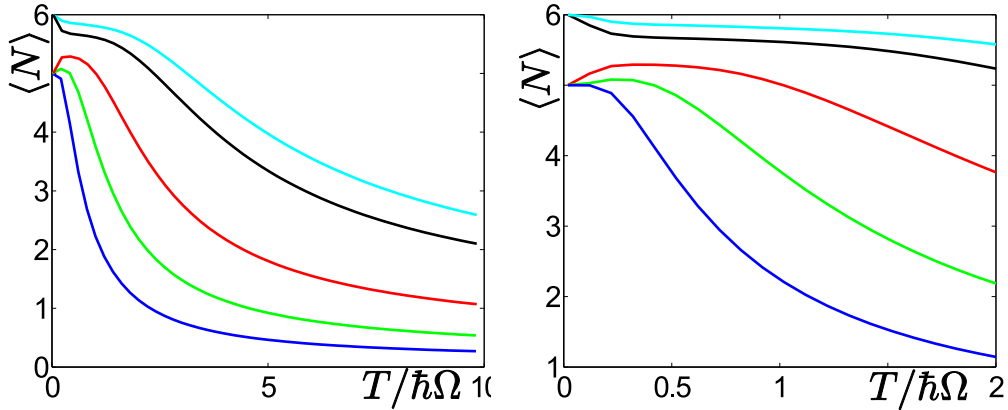
Figure 7.9: Average dot population as a function of temperature. The left figure corresponds to parameters $\lambda^2 = 2$, $\alpha = 0.01$, $E_{\mathrm{ch}} = 1$ and from bottom to top $Q_g/e = 0.05, 0.1, 0.2\,0.4$ and 0.5. The right figure clarifies the low-temperature region.

In Figure 7.13 we have plotted current vs. gate charge with a variable phonon nonlinearity. Small changes in the strength of the nonlinearity change energy differences of the nearby states at the potential minima leading to phase shifts in the current oscillations. Since the current is an even function of the gate charge it exhibits a cusp close to $Q_g = 0$ depending on the phase of the current oscillations. The most pronounced effect is achieved when the current oscillations jump by half a period at the origin. At finite temperatures the cusp is always smooth and becoming sharper when temperature decreases. The reason for the existence of the cusp is the symmetry breaking between the two minima of the effective potential at finite Q_g. Even small gate values localize the system in one minimum leading to observable effects in the current through the structure.

7.5 Carbon nanotube realization

The interplay of electronic and mechanical degrees of freedom is enriched when the corresponding energy scales are roughly of the same order of magnitude. Then the realization of the negative-U regime requires that also the coupling energy scale is comparable to the charging and the vibron energies, as indicated by conditions (7.18) and (7.22). This requirement seems to rule out the currently existing suspended electron beam lithography samples where the coupling energy is still a small fraction of the uncoupled energy scales. However, recent experimental [60] and theoretical [9] studies seem to indicate that the negative-U regime could be reached in suspended carbon nanotube quantum dots.

The relevant phonon modes for this purpose in the case of a nanotube are stretching modes and breathing modes. The mechanical motion associated with these modes correspond to a longitudinal and a radial stretch and contraction, respectively. Stretching modes provide a large electronic coupling, limitation being that the vibron energy scale tends to be somewhat smaller than the single particle and charging energies. For breathing
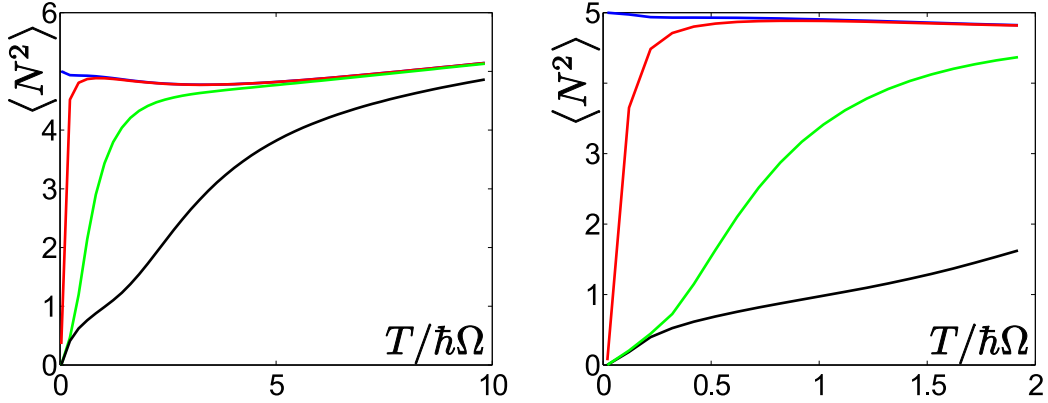
Figure 7.10: Root mean square fluctuation as a function of temperature. The left figure corresponds to parameters $E_{\mathrm{ch}} = \hbar\Omega$, $\alpha = 0.01\,(\hbar\Omega)^{-1}$, $\lambda^2 = 2$ and from bottom to top $Q_g/e = 0.5, 0.1, 0.01, 0$. At vanishing gate the low-temperature fluctuations saturate at finite value, otherwise they will go to zero. The right figure clarifies the low-temperature region.

modes the situation is reversed, the vibron energy is large but the electronic coupling is smaller. To realize condition (7.22) it is beneficial to have high vibron energies and coupling, so one has to search for an optimal trade off. The vibron energies are determined by the material constants and the tube dimensions as

$$\Omega^{\mathrm{stretch}} = v_{\mathrm{stretch}} q\,,$$
$$\Omega^{\mathrm{breath}} = \sqrt{(Ar^2 + \kappa)/\rho_0 r^4}, \tag{7.35}$$

where $v_{\mathrm{stretch}} \approx 2.4 \times 10^4$ m/s, $A = 2\mu + \lambda'$, $\mu = 4\lambda' = 9 \times 10^{20} eV\,\mathrm{m}$ and $\kappa = 1\,eV$ [9]. These numbers lead to the prediction

$$\hbar\Omega^{\mathrm{stretch}} \approx 0.60\,\mathrm{K/L}[\mu\mathrm{m}]\text{ and}$$
$$\hbar\Omega^{\mathrm{breath}} \approx 200\,\mathrm{K/r}[\mathrm{nm}], \tag{7.36}$$

where L and r are the length and the radius of the (suspended part of the) nanotube. Employing the above introduced numerical values the single-particle level separation (7.19) becomes $\Delta = 24\mathrm{K}/L_d[\mu\mathrm{m}]$. Estimates for coupling constants become

$$\lambda^{\mathrm{stretch}} = \frac{3}{\sqrt{L_\perp[\mathrm{nm}]}}\text{ and}$$
$$\lambda^{\mathrm{breath}} = \frac{7 \times 10^{-2}}{\sqrt{L[\mu\mathrm{m}]}}. \tag{7.37}$$

Assuming that the charging energy is in the range $E_{\mathrm{ch}} \sim 10 - 20$ K, the above estimates suggests that condition (7.22) could be realized for a breathing mode of a nanotube of
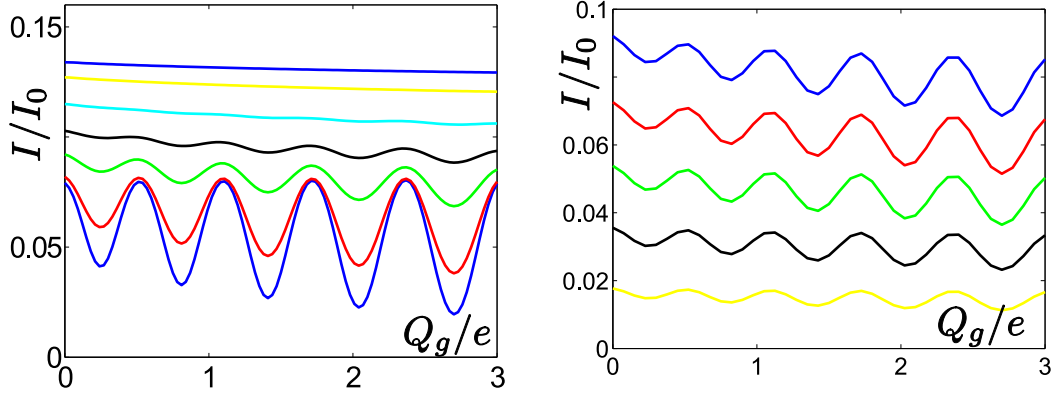
Figure 7.11: Current as a function of the gate charge. Left: Different curves correspond to temperatures (from top to bottom) $T = 0.2, 0.15, 0.1, 0.07, 0.05, 0.03, 0.02 \times \hbar\Omega$, other parameters being $E_{\text{ch}} = 0.2\,\hbar\Omega$, $\alpha = 0.05\,(\hbar\Omega)^{-1}$, $\lambda^2 = 0.5$, and $\mu_L = -\mu_R = 0.1\,\hbar\Omega/e$. Right: Curves correspond to voltages (from top to bottom) $\mu_L = -\mu_R = 0.1, 0.08, 0.06, 0.04, 0.02 \times \hbar\Omega/e$, other parameters being $E_{\text{ch}} = 0.2\,\hbar\Omega$, $\lambda^2 = 0.5$, $\alpha = 0.05$, and $T = 0.05\,\hbar\Omega$.

dimensions $r \sim 1\,\text{nm}$ and $L \sim 50 - 100\,\text{nm}$. For a stretching mode condition (7.22) could be fulfilled if the electronic confinement length is roughly ten times the suspended length $L_d \sim 10\,L$. The recent experiment [60] indicates that, indeed, it is possible that the effective electronic confinement length is larger than the suspended part of the nanotube which is beneficial for reaching the negative-U regime by coupling to a stretching mode. Although the employed material constants are not known accurately, preventing us making a precise statement, they indicate that the instability is at least a real possibility in suitable circumstances. Moreover, there is at least no fundamental principle which would make it impossible.

7.6 Conclusions

In this part of the thesis, we have studied effects of strong electron-phonon interaction in quantum dots with a vibrational degree of freedom. At sufficiently strong couplings the vibron-induced polaron shift overcomes the charging energy cost and the effective potential for electrons favors large charging. The instability towards an arbitrarily large electron population on the dot is regularized by the anharmonic contribution to the phonon energy. The effective potential differs qualitatively from the usual Coulomb repulsion, leading to characteristic modifications of the low temperature Coulomb blockade properties. Signatures include a rapid change in the average and the fluctuations of the electron number as function of the gate charge in the neighborhood of $Q_g = 0$ as well as the temperature dependence of these quantities. Moreover, transport properties also show a number of unique signatures that can be used to characterize the negative-U instability and the
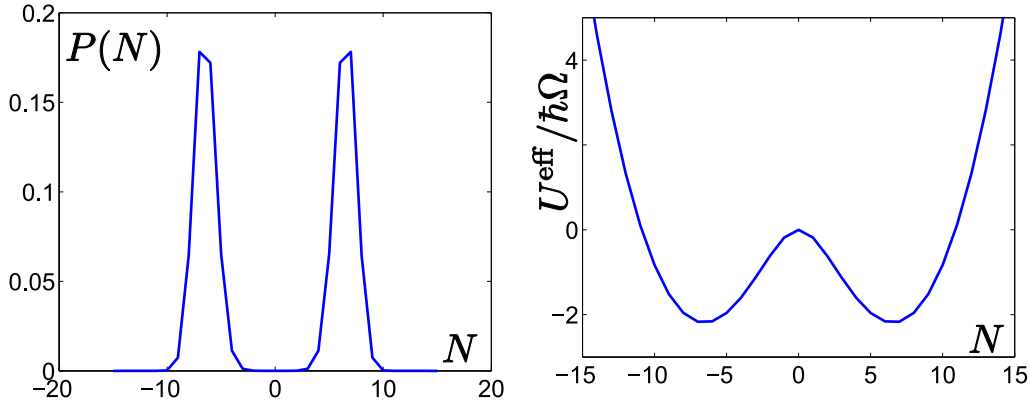
Figure 7.12: Left: Probability distribution of the dot population corresponding to parameters $E_{\text{ch}} = 0.2\,\hbar\Omega$, $\alpha = 0.05\,(\hbar\Omega)^{-1}$, $\lambda^2 = 0.5$ and $\mu_L = -\mu_R = 0.1\,\hbar\Omega/e$, $Q_g = 0$ at $T = 0.1\,\hbar\Omega$. Right: The effective potential corresponding to the same parameters.

nonlinear phonon effects.

It is interesting to check whether in addition to molecules, an effectively negative U could also be achieved in nanoelectromechanical systems. As shown by Eq. (7.22), this requires an electron-vibron coupling (as measured by $\lambda\hbar\omega$) which is of the same order of magnitude as the charging and the single-particle energies. It turns out that this condition rules out currently existing suspended electron beam lithography samples. At the same time, the situation is more favorable (though still marginal) for suspended carbon-nanotube devices, for which strong electron-vibron coupling has been observed in several recent experiments [93, 94, 95]. The most likely vibron mode to cause a negative U in this system is the radial breathing mode with frequency $\omega \sim c/L_\perp$. (Here, c denotes the velocity of propagation of acoustic phonons in graphene and $L_\perp$ is the circumference of the nanotube.) The charging energy and the single-particle level spacing are of the same order (assuming a "fine-structure constant" $e^2/\hbar v_F \sim 1$ as appropriate for graphene) so that in order to reach the negative U instability, the electron-vibron coupling λ must exceed $[(v_F/c)(L_\perp/L)]^{1/2}$ for a nanotube of length L. Using $v_F/c \sim 10^2$, $L_\perp \sim 1\text{nm}$, and $L \sim 1\mu\text{m}$, we find that the critical coupling strength is $\lambda_c \sim 0.1 - 1$. Unfortunately, this coupling constant is relatively poorly understood at present. However, both experiment [93] and theoretical estimates for one possible coupling mechanism [9] suggest that it is of the same order as λ_c[6]. While these estimates do not allow us to claim that the instability discussed here could be observed in carbon-nanotube devices, they do suggest that realizing a negative U in nanoelectromechanical systems is certainly conceivable.

According to results of Ref. [9], the breathing-mode frequency of a nanotube and the electron-vibron coupling with the typical material parameters can be estimated as

---

[6]According to Ref. [9], λ for the breathing mode scales as $L^{-\frac{1}{2}}$ which means that decreasing the critical coupling strength by increasing the length of the tube does not improve the possibility of reaching the negative-U regime.
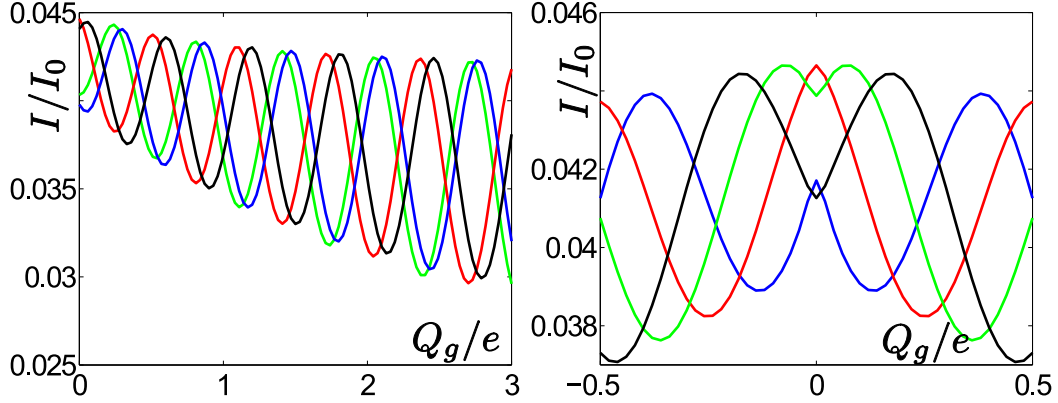
Figure 7.13: Current as a function of the gate charge at different phonon nonlinearity strengths. Left: The different curves illustrate cases $\alpha = 0.058\,(\hbar\Omega)^{-1}$ (green), $\alpha = 0.05\,(\hbar\Omega)^{-1}$ (red), $\alpha = 0.045\,(\hbar\Omega)^{-1}$ (blue) and $\alpha = 0.04\,(\hbar\Omega)^{-1}$ (black), other parameters being $E_{\mathrm{ch}} = 0.2\,\hbar\Omega$, $\lambda{=}0.5$, $T = 0.05\,\hbar\Omega$ and $\mu_L = -\mu_R = 0.05\,\hbar\Omega/e$. Right: Same quantities in the vicinity of $Q_g = 0$. The curves correspond to $\alpha = 0.056\,(\hbar\Omega)^{-1}$ (black), $\alpha = 0.053\,(\hbar\Omega)^{-1}$ (green), $\alpha = 0.05\,(\hbar\Omega)^{-1}$ (red) and $\alpha = 0.047\,(\hbar\Omega)^{-1}$ (blue), other parameters as in the left plot.

$\Omega^b \sim 200\,\mathrm{K/r[nm]}$ and $\lambda^b \sim 10^{-1}/\sqrt{L[\mu\mathrm{m}]}$ where r and L denote the radius and the length of the nanotube. For a nanotube with radius $\sim 1\,\mathrm{nm}$ and length $\sim 1\,\mu\mathrm{m}$ the charging and the single-particle energies are expected to be $10 - 50$ K, suggesting that the system is close to the instability $\lambda^b \sim \sqrt{(E_{\mathrm{ch}} + \Delta)/\hbar\Omega^b}$. The presented estimate for λ is based on idealized theoretical considerations and is of limited applicability in a real experimental setting [93] where details of the electron-vibron coupling are not well understood. The existence of the negative-U regime in these systems cannot be determined conclusively at present.

Chapter 8

Conclusions

In this thesis we have analyzed two distinct systems on nanometer scales which are driven out of equilibrium. This has been accomplished by adding an additional perturbation in the case of persistent currents in normal metal rings or by assuming that a perturbation which is inherently present becomes particularly strong in the case of quantum dots coupled to vibrational modes. Both systems have in common that they were studied theoretically and experimentally to some extent before, and that new effects of quantum mechanical origin arise from adding (or increasing) the respective perturbation. We have analyzed the emerging effects and discussed the accessibility to experiments as well as arising theoretical questions.

The first part of the thesis is dealing with normal metal rings developing persistent currents under breaking of their time reversal symmetry. We have shown that the experimental signal of these currents can be amplified by adding an additional microwave field which, in the considered case, stands perpendicular to the rings. Since the microwave field drives the electronic distribution out of its equilibrium form we have applied a formalism which is inherently able to treat out-of-equilibrium processes. We have analyzed and extended known methods of calculating correlation functions using this formalism to the case of rings pierced by a magnetic flux.

In summary we have been able to discriminate two distinct physical effects leading to an additional signal in the typical current and the current fluctuations. It has turned out that at the lower bound of field-frequencies lying within the borders of our perturbative approach the additional signal arising from the microwave-induced change in the density of states dominates the photovoltaic effect. We have shown that the microwave field can produce an additional signal which can become even larger than the equilibrium persistent current in the low-frequency regime. In the regime of high frequencies the photovoltaic effect becomes more pronounced compared to the effect arising from the change in the density of states, but both signals together will be small compared to the equilibrium persistent current and thus hardly accessible to experiments.

In the second part of the thesis we have considered quantum dots which are coupled to a vibrational mode. As we have discussed it is at least possible that carbon-nanotube quantum dots can exhibit an electron-vibron coupling which is so strong, that the renormalized charging energy becomes negative and its absolute value larger than the cost in charging energy for tunneling of additional electrons on the dot. In this case the commonly used

harmonic approximation of the vibronic energy would lead to an unphysical instability towards adding an infinite number of charge carriers to the quantum dot. We have corrected this instability by adding an anharmonic contribution to the phonon energy and analyzed the effect of this anharmonic term on thermal equilibrium and transport properties of the system.

We have shown that the anharmonic term leads to an effective potential which exhibits a double-well form as a function of the number of excess electrons on the dot. This effective potential leads to new equilibrium values of the number of excess electrons, which are degenerated at zero gate charge. Driving the system slightly out of equilibrium by varying the gate voltage leads to a characteristic rapid change in the average and the fluctuations of the number of excess electrons on the dot. Analyzing the transport properties of the system yields several modifications of Coulomb blockade effects. The Coulomb blockade regime is known to exhibit a strict periodicity under changing the gate charge by multiples of the electron charge. This periodicity is broken in the considered negative-U case. Instead we observe a slowly decreasing tendency of the current as well as a growth of the amplitudes of the Coulomb oscillations when the gate voltage is increased. Further we have shown that, in contrast to the Coulomb blockade regime, the current is not completely blocked around integer gate charges at low temperatures in the negative-U case. Finally we have discovered that the current will exhibit a cusp at zero gate voltage which arises due to the symmetry breaking of the double-well effective potential even at small gate charges.

In summary, we have discussed two known mesoscopic systems which exhibit new interesting and experimentally accessible features when exposed to additional perturbations. In deriving these new effects we have analyzed and expanded non-equilibrium techniques which are applicable to a variety of problems in theoretical condensed matter physics.

Appendix A

Additional calculations to persistent current under microwave irradiation

A.1 The diffuson in momentum and energy space

The Dyson equation for the diffuson shown in Figure 2.7 reads in momentum and energy space[1]

$$D(\boldsymbol{q},\omega) = \frac{\gamma_e}{V} + \frac{\gamma_e}{V} \sum_{\boldsymbol{k}'} G^R(\boldsymbol{k}',\Omega) \, G^A(\boldsymbol{k}' + \boldsymbol{q}, \Omega + \omega) \, D(\boldsymbol{q},\omega) \,. \tag{A.1}$$

Since we can expect the diffuson to be sharply peaked in space and time variables, we can expand the advanced Green function in Eq. (A.1) in $\boldsymbol{q}$ and ω,

$$G^A(\boldsymbol{k}' + \boldsymbol{q}, \Omega + \omega) \approx G^A(\boldsymbol{k}',\Omega) + (\boldsymbol{v}\cdot\boldsymbol{q} + \omega) \left(G^A(\boldsymbol{k}',\Omega)\right)^2 + (\boldsymbol{q}\cdot\boldsymbol{v})^2 \left(G^A(\boldsymbol{k}',\Omega)\right)^3 \,. \tag{A.2}$$

Inserting this into Eq. (A.1) and using ([2], chapter 3)

$$\frac{\gamma_e}{V} \sum_{\boldsymbol{k}} \left(G^R(\boldsymbol{k},\omega)\right)^n \left(G^A(\boldsymbol{k},\omega)\right)^m = \begin{cases} 1 & \text{for } m = 1 \text{ and } n = 1 \\ i\tau_e & \text{for } m = 1 \text{ and } n = 2 \\ -\tau_e^2 & \text{for } m = 1 \text{ and } n = 3 \,, \end{cases} \tag{A.3}$$

we get, noting that the term proportional to $\boldsymbol{q}$ vanishes after angular integration,

$$\begin{aligned} D(\boldsymbol{q},\omega) &= \frac{\gamma_e}{V} + \left(1 + i\tau_e\omega - \frac{\tau_e^2 v_F^2}{d}\, \boldsymbol{q}^2\right) D(\boldsymbol{q},\omega) \\ &= \frac{\gamma_e}{V\tau_e}\, \frac{1}{D\boldsymbol{q}^2 - i\omega} \,, \end{aligned} \tag{A.4}$$

where we introduced the diffusion constant $D = v_F^2 \tau_e / d$.

---

[1] We set $\hbar = 1$ in this section.

A.2 Integrals in section 4.2

We want to calculate the integral

$$\int dx\, e^{-2\pi i p x} \frac{x}{x^2 - i(\epsilon - \epsilon')} . \tag{A.5}$$

The integrand has poles at $x_{1/2} = \pm i^{3/2}\sqrt{\epsilon - \epsilon'}$, and we can close the integration contour in the lower half due to the exponential factor. We define the branch cut of the complex square root to lie on the negative real axis, leading to $\sqrt{i} = \frac{1+i}{\sqrt{2}}$. Calculation of the residue yields

$$\int dx\, e^{-2\pi i p x} \frac{x}{x^2 - i(\epsilon - \epsilon')} = -2\pi i \operatorname{Res}\left(\frac{x\, e^{-2\pi i p x}}{x^2 - i(\epsilon - \epsilon')}, -i^{3/2}\sqrt{\epsilon - \epsilon'} \right)$$

$$= -2\pi i\, e^{2\pi i^{3/2} p \sqrt{\epsilon - \epsilon'}} \frac{-i^{1/2}\sqrt{\epsilon - \epsilon'}}{-2 i^{1/2}\sqrt{\epsilon - \epsilon'}} = -\pi i\, e^{2\pi i^{3/2} p \sqrt{\epsilon - \epsilon'}} . \tag{A.6}$$

The other integral to solve is the integral over the energies at zero temperature

$$\int_{-\infty}^{0} d\epsilon \int_{-\infty}^{0} d\epsilon'\, e^{2\pi i^{3/2} p \sqrt{\epsilon - \epsilon'}} . \tag{A.7}$$

Introducing sum and difference variables $\sigma = \frac{1}{2}\left(\epsilon + \epsilon' \right)$, $\Delta = \epsilon - \epsilon'$, yields

$$\int_{-\infty}^{0} d\epsilon \int_{-\infty}^{0} d\epsilon'\, e^{2\pi i^{3/2} p \sqrt{\epsilon - \epsilon'}}$$

$$= \int_{-\infty}^{0} d\sigma \int_{-2|\sigma|}^{2|\sigma|} d\Delta\, e^{2\pi i^{3/2} p \sqrt{\Delta}}$$

$$= \int_{-\infty}^{0} d\sigma \int_{0}^{2|\sigma|} d\Delta \left[e^{2\pi i^{3/2} p \sqrt{\Delta}} + \text{c.c.} \right]$$

$$= 2\operatorname{Re} \int_{-\infty}^{0} d\sigma \int_{0}^{2|\sigma|} d\Delta\, e^{2\pi i^{3/2} p \sqrt{\Delta}}$$

$$\overset{x=\sqrt{\Delta}}{=} 2\operatorname{Re} \int_{-\infty}^{0} d\sigma \int_{0}^{\sqrt{2|\sigma|}} dx\, 2x\, e^{\alpha x} \Bigg|_{\alpha = 2\pi i^{3/2} p}$$

$$= 2\operatorname{Re} \int_{-\infty}^{0} d\sigma\, 2\partial_{\alpha} \int_{0}^{\sqrt{2|\sigma|}} dx\, e^{\alpha x} \Bigg|_{\alpha = 2\pi i^{3/2} p}$$

$$= 4\operatorname{Re} \int_{-\infty}^{0} d\sigma\, \partial_{\alpha} \frac{1}{\alpha}\left(e^{\alpha \sqrt{2|\sigma|}} - 1 \right) \Bigg|_{\alpha = 2\pi i^{3/2} p} , \tag{A.8}$$

and since $\partial_{\alpha}\frac{1}{\alpha}$ is purely imaginary

$$= 4\operatorname{Re} \int_{-\infty}^{0} d\sigma\, \partial_{\alpha} \frac{1}{\alpha}\, e^{\alpha \sqrt{2|\sigma|}} \Bigg|_{\alpha = 2\pi i^{3/2} p}$$

$$= 4\, \partial_{\alpha} \frac{1}{\alpha^3} \Bigg|_{\alpha = 2\pi i^{3/2} p} = \frac{3}{4} \frac{1}{(\pi p)^4} , \tag{A.9}$$

where we used $\operatorname{Re}\alpha < 0$ in the last line.
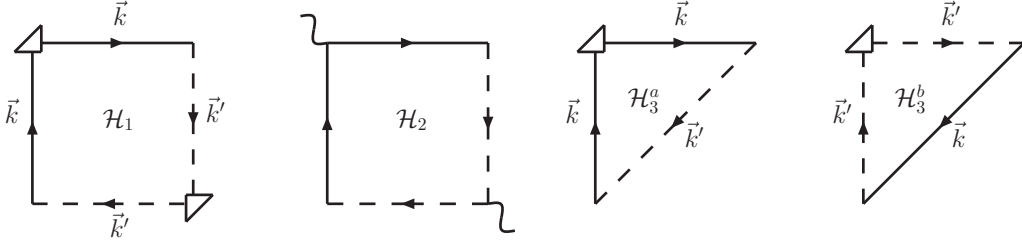
Figure A.1: Hikami boxes of the diffuson diagrams in Figures 4.6 and 4.7. In the diffuson Hikami boxes one can expand around $\boldsymbol{k} - \boldsymbol{k}' \approx 0$.

A.3   Hikami Boxes for RRR/AAA diagrams

The Hikami boxes for the Diffusons are shown in Figure A.1. Since the current vertices and the interactions with the field are linear in momentum, we can neglect additional impurity lines connecting two advanced or two retarded Green functions. Including the expression found for the current vertices in chapter 4.2

$$\vartheta_\alpha = -i \frac{e\hbar}{\pi} v_\alpha \,, \tag{A.10}$$

the first Hikami box reads

$$\mathcal{H}_1 = \left(i \frac{e\hbar}{\pi} \right)^2 \frac{1}{V} \sum_{\boldsymbol{k}} v_\alpha \, v_\beta \, G^R(\boldsymbol{k}, \epsilon)^2 \, G^A(\boldsymbol{k}', \epsilon')^2 \,. \tag{A.11}$$

Since the Green functions depend only on the absolute value of the momentum, we can calculate the angular integral first. With

$$\int \frac{d\Omega}{\Omega} \, v_\alpha \, v_\beta = \frac{v_F^2}{d} \, \delta_{\alpha,\beta} \,, \tag{A.12}$$

where we replaced the velocity by the Fermi velocity since the Green functions which are left to integrate are sharply peaked at $\boldsymbol{k} = \boldsymbol{k}_F$, we are left with

$$\mathcal{H}_1 = -\left(\frac{e\hbar}{\pi} \right)^2 \frac{v_F^2}{d} \, \delta_{\alpha,\beta} \frac{1}{V} \sum_{k} G^R(\boldsymbol{k}, \epsilon)^2 \, G^A(\boldsymbol{k}', \epsilon')^2 \,. \tag{A.13}$$

Sums of this type are performed in reference [2], Section 3, and we will accordingly call

$$f^{m,n} \equiv \frac{\gamma_e}{V} \sum_{k} G^R(\boldsymbol{k}, \epsilon)^m \, G^A(\boldsymbol{k}, \epsilon)^n \,, \tag{A.14}$$

as we did before. Thus $\mathcal{H}_1$ is to lowest order in $\boldsymbol{k} - \boldsymbol{k}'$ given by

$$\mathcal{H}_1 = -\left(\frac{e\hbar}{\pi} \right)^2 \frac{v_F^2}{d} \, \delta_{\alpha,\beta} \frac{1}{\gamma_e} f^{2,2} = -\left(\frac{e\hbar}{\pi} \right)^2 \frac{v_F^2}{d} \, \delta_{\alpha,\beta} \frac{2\tau_e^2}{\gamma_e} \,. \tag{A.15}$$
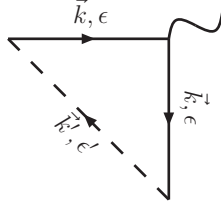
Figure A.2: Hikami boxes occuring in second-order diagrams and in diagrams in which the field interactions do not come in pairs.

The second Hikami box can be evaluated the same way replacing the current vertices by the field interactions

$$\boldsymbol{k} \cdot \boldsymbol{A} = k_z A_z = k_z \frac{E}{\hbar \nu} \, . \tag{A.16}$$

We get

$$\mathcal{H}_2 = - \left(\frac{e\hbar}{\pi} \right)^2 \left(\frac{E}{\hbar \nu} \right)^2 \frac{v_F^2}{d} \frac{2\tau_e^2}{\gamma_e} \, . \tag{A.17}$$

Since the third Hikami box contains just one current vertex, the angular integration vanishes in zeroth order in $\boldsymbol{k} - \boldsymbol{k}'$ and we have to expand to first order. Using

$$G^{R/A}(\boldsymbol{k} + \boldsymbol{q}, \epsilon') \approx G^{R/A}(\boldsymbol{k}, \epsilon) + \boldsymbol{v} \cdot \boldsymbol{q} \, G^{R/A}(\boldsymbol{k}, \epsilon)^2 \tag{A.18}$$

we get

$$
\begin{aligned}
\mathcal{H}_3^a &= -i \frac{e\hbar}{\pi} \frac{1}{V} \sum_{\boldsymbol{k}} k_\alpha \, G^R(\boldsymbol{k}, \epsilon)^2 \, G^A(\boldsymbol{k}', \epsilon') \\
&\approx -i \frac{e\hbar}{\pi} \frac{1}{V} \sum_{\boldsymbol{k}} k_\alpha \, G^R(\boldsymbol{k}, \epsilon)^2 \left(G^A(\boldsymbol{k}, \epsilon) - \boldsymbol{v} \cdot (\boldsymbol{k} - \boldsymbol{k}') G^A(\boldsymbol{k}, \epsilon)^2 \right) \\
&\approx i \frac{e\hbar}{\pi} \frac{v_F^2}{d} \frac{2\tau_e^2}{\gamma_e} \left(\boldsymbol{k} - \boldsymbol{k}' \right), \\
\mathcal{H}_3^b &= -i \frac{e\hbar}{\pi} \frac{1}{V} \sum_{\boldsymbol{k}'} k_\alpha' G^R(\boldsymbol{k}, \epsilon) \, G^A(\boldsymbol{k}', \epsilon')^2 \\
&\approx -i \frac{e\hbar}{\pi} \frac{v_F^2}{d} \frac{2\tau_e^2}{\gamma_e} \left(\boldsymbol{k} - \boldsymbol{k}' \right).
\end{aligned} \tag{A.19}
$$

At this point we can also deduce, that diagrams in which the field interactions do not come in pairs vanish as long as the microwave field stands perpendicular to ring. Those diagrams would contain Hikami boxes of the form shown in Figure A.2, which turn out to vanish after angular integration.

The Hikami boxes for the cooperon diagrams are shown in Figure A.3. Since the Green functions depend only on the absolute value of the momentum we can replace $\boldsymbol{k}' \to -\boldsymbol{k}'$
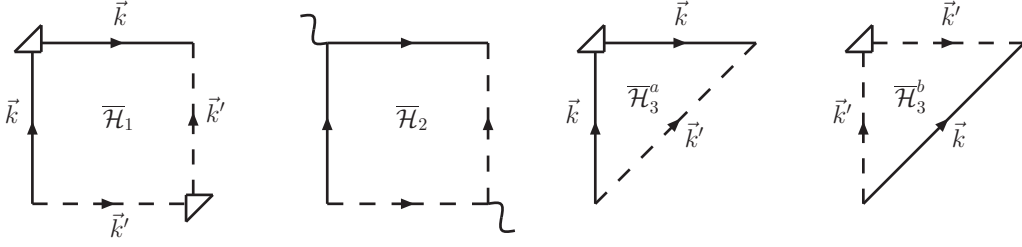
Figure A.3: Hikami boxes of the cooperon diagrams in Figure 4.6 and 4.7. The Green function can be expanded around $\boldsymbol{k} + \boldsymbol{k}' \approx 0$.

in the arguments. Following the same reasoning as for the diffuson Hikami boxes we get

$$\overline{\mathcal{H}}_1 = \left(\frac{e\hbar}{\pi} \right)^2 \frac{1}{V} \sum_{\boldsymbol{k}} v_\alpha \, v_\beta \, G^R(\boldsymbol{k}, \epsilon)^2 \, G^A(\boldsymbol{k}', \epsilon')^2 = \left(\frac{e\hbar}{\pi} \right)^2 \frac{v_F^2}{d} \, \delta_{\alpha,\beta} \, \frac{2\tau_e^2}{\gamma_e},$$

$$\overline{\mathcal{H}}_2 = \left(\frac{e\hbar}{\pi} \right)^2 \left(\frac{E}{\hbar\nu} \right)^2 \frac{v_F^2}{d} \frac{2\tau_e^2}{\gamma_e},$$

$$\overline{\mathcal{H}}_3^a = \overline{\mathcal{H}}_3^b = i \, \frac{e\hbar}{\pi} \frac{v_F^2}{d} \frac{2\tau_e^2}{\gamma_e} \, (\boldsymbol{k} + \boldsymbol{k}') . \tag{A.20}$$

A.4   Calculation of contributions two and three in Eq. (4.72)

A.4.1   Contribution 2

The second contribution takes the form

$$\langle II \rangle_{\text{Contr.2}} = \sum_{\nu,\nu'=\pm\nu} \int d\epsilon \int d\epsilon' \left[n(\epsilon \pm \nu) - n(\epsilon) \right] \left[n(\epsilon') - n(\epsilon \pm \nu') \right]$$

$$\times \int dx \, \text{Re} \left\{ \frac{x^2 \, e^{-2\pi ipx}}{(x^2 + \eta - i(\epsilon - \epsilon'))^2 (x^2 + \eta - i(\epsilon - \epsilon' + \nu - \nu'))^2} \right\} . \tag{A.21}$$

We will discriminate between the cases $\nu = \nu'$ and $\nu = -\nu'$, and start with the latter one.

$\nu = -\nu'$

We can see that the contributions in the cases $\nu - \nu' = 2\nu$ and $\nu - \nu' = -2\nu$ are the same by shifting $\epsilon \to \epsilon - \nu$ and $\epsilon' \to \epsilon' + \nu$. In the case $\nu - \nu' = 2\nu$ the x-integral turns into

$$\int dx \, \frac{x^2 \, e^{-2\pi ipx}}{(x^2 + \eta - i(\epsilon - \epsilon'))^2 (x^2 + \eta - i(\epsilon - \epsilon' 2\nu))^2} = \int dx \frac{x^2 \, e^{-2\pi ipx}}{(x^2 + a^2)^2 (x^2 + b^2)^2} , \tag{A.22}$$

where we defined $a = \sqrt{\eta - i(\epsilon - \epsilon')}$ and $b = \sqrt{\eta - i(\epsilon - \epsilon' + 2\nu)}$ again. As in Section 4.5.1 we can close the contour in the lower plane, encircling the poles $x = -ia$ and $x = -ib$.

117

Thus the x-integral turns into

$$
\int dx \, \frac{x^2 \, e^{-2\pi i p x}}{(x^2 + \eta - i(\epsilon - \epsilon'))^2 (x^2 + \eta - i(\epsilon - \epsilon' + \nu - \nu'))^2}
$$

$$
= -2\pi i \left(\mathrm{Res} \left[\frac{x^2 \, e^{-2\pi i p x}}{(x^2 + a^2)^2 (x^2 + b^2)^2}, x = -ia \right] + \mathrm{Res} \left[\frac{x^2 \, e^{-2\pi i p x}}{(x^2 + a^2)^2 (x^2 + b^2)^2}, x = -ib \right] \right)
$$

$$
= -\frac{\pi}{2} \left(\frac{e^{-2\pi p a}(a^2(3 + 2\pi p a) + b^2(1 - 2\pi p a))}{a(a^2 - b^2)^3} - \frac{e^{-2\pi p b}(a^2(1 - 2\pi p b) + b^2(3 + 2\pi p b))}{b(a^2 - b^2)^3} \right)
$$

$$
= \frac{\pi e^{-2\pi p \left(\sqrt{\eta - i(\epsilon - \epsilon')} + \sqrt{\eta - i(\epsilon - \epsilon' + 2\nu)} \right)}}{8 \sqrt{\eta - i(\epsilon - \epsilon')} \, \nu^3 \, \sqrt{\eta - i(\epsilon - \epsilon' + 2\nu)}}
$$

$$
\left[e^{2\pi p \sqrt{\eta - i(\epsilon - \epsilon' + 2\nu)}} \sqrt{\eta - i(\epsilon - \epsilon' + 2\nu)} \left(-2i\eta - 2(\epsilon - \epsilon') - \nu + 2\pi p \nu \sqrt{\eta - i(\epsilon - \epsilon')} \right) \right.
$$

$$
\left. + e^{2\pi p \sqrt{\eta - i(\epsilon - \epsilon')}} \sqrt{\eta - i(\epsilon - \epsilon')} \left(2i\eta + 2(\epsilon - \epsilon') + 3\nu + 2\pi p \nu \sqrt{\eta - i(\epsilon - \epsilon' + 2\nu)} \right) \right].
$$

$$
(A.23)
$$

Due to the exponential factors we can close the ϵ-integration contour in the upper, and the ϵ'-integration contour in the lower half, encircling only the Fermi poles, which lie this time at $\epsilon = \frac{2\pi}{\beta}(2l + 1)$ for $n(\epsilon)$ and $\epsilon = \frac{2\pi}{\beta}(2l + 1) - \nu$ for $n(\epsilon + \nu)$. Evaluating the function in Eq. (A.23) at the four different poles yields a quite lengthy expression which can be written as

$$
\langle II \rangle_{\mathrm{Contr.2}, \nu = -\nu'} = 2 \left(\frac{2\pi}{\beta} \right) \sum_{l,m=0}^{\infty} \left[f_{\nu - \nu' = 2\nu, \mathrm{Contr2}} \left(\frac{\pi i}{\beta}(2l + 1) - \nu, -\frac{\pi i}{\beta}(2m + 1), p, \nu, \eta \right) \right.
$$

$$
- f_{\nu - \nu' = 2\nu, \mathrm{Contr2}} \left(\frac{\pi i}{\beta}(2l + 1), -\frac{\pi i}{\beta}(2m + 1), p, \nu, \eta \right)
$$

$$
- f_{\nu - \nu' = 2\nu, \mathrm{Contr2}} \left(\frac{\pi i}{\beta}(2l + 1) - \nu, -\frac{\pi i}{\beta}(2m + 1) + \nu, p, \nu, \eta \right)
$$

$$
\left. + f_{\nu - \nu' = 2\nu, \mathrm{Contr2}} \left(\frac{\pi i}{\beta}(2l + 1), -\frac{\pi i}{\beta}(2m + 1) + \nu, p, \nu, \eta \right) \right], \qquad (A.24)
$$

where $f_{\nu + \nu' = 2\nu, \mathrm{Contr2}}(\epsilon, \epsilon', p, \nu, \eta)$ abbreviates the result of the x-integral in Eq. (A.23), and we included a factor of two accounting also for the case $\nu - \nu' = -\nu$.

$\nu - \nu' = 0$

The two possibilities $\nu = \nu' = \pm\nu$ leading to $\nu - \nu' = 0$ give the same contribution as one can see by shifting $\epsilon \to \epsilon - \nu$ and $\epsilon' \to \epsilon' - \nu$. Thus we concentrate on $\nu = \nu' = \nu$ and multiply the result by two. The x-integral reads

$$
\int dx \frac{x^2 e^{-2\pi i p x}}{(x^2 + \eta - i(\epsilon - \epsilon'))^4} = \int dx \frac{x^2 e^{-2\pi i p x}}{(x^2 + a^2)^4}, \qquad (A.25)
$$

where we introduced $a = \sqrt{\eta - i(\epsilon - \epsilon')}$. We can close the integration contour in the lower plane, encircling the pole at $x = -ia$, again, which leads to

$$\int dx \frac{x^2 e^{-2\pi i p x}}{(x^2 + a^2)^4} = -2\pi i \mathrm{Res}\left[\frac{x^2 e^{-2\pi i p x}}{(x^2 + a^2)^4}, x = -ia\right] = \frac{\pi e^{-2\pi p a}}{48 a^5}\left(3 + 6\pi p a - 8\pi^3 p^3 a^3\right)$$

$$= \frac{e^{-2\pi p \sqrt{\eta - i(\epsilon - \epsilon')}}}{48(\eta - i(\epsilon - \epsilon'))^{5/2}}\left(3 + 6\pi p\sqrt{\eta - i(\epsilon - \epsilon')} - 8\pi^3 p^3(\eta - i(\epsilon - \epsilon'))^{3/2}\right).$$
(A.26)

The integration contours for ϵ (ϵ') can again be closed in the upper (lower) half, and we get for the second contribution in the case $\nu = \nu'$

$$\langle II \rangle_{\mathrm{Contr.2}, \nu = \nu'} = \frac{\pi^3}{6\beta^2}\Bigg[-\frac{2e^{-2\pi p\sqrt{\frac{2\pi}{\beta}(l+m+1)+\eta}}}{\left(\frac{2\pi}{\beta}(l+m+1)+\eta\right)^{5/3}}$$

$$\left(3 + 6\pi p\sqrt{\frac{2\pi}{\beta}(l+m+1)+\eta} - 8\pi^3 p^3\left(\frac{2\pi}{\beta}(l+m+1)+\eta\right)^{3/2}\right)$$

$$+ \frac{e^{-2\pi p\sqrt{\frac{2\pi}{\beta}(l+m+1)+\eta - i\nu}}}{\left(\frac{2\pi}{\beta}(l+m+1)+\eta - i\nu\right)^{5/2}}$$

$$\left(3 + 6\pi p\sqrt{\frac{2\pi}{\beta}(l+m+1)+\eta - i\nu} - 8\pi^3 p^3\left(\frac{2\pi}{\beta}(l+m+1)+\eta - i\nu\right)^{3/2}\right)$$

$$+ \frac{e^{-2\pi p\sqrt{\frac{2\pi}{\beta}(l+m+1)+\eta + i\nu}}}{\left(\frac{2\pi}{\beta}(l+m+1)+\eta + i\nu\right)^{5/2}}$$

$$\left(3 + 6\pi p\sqrt{\frac{2\pi}{\beta}(l+m+1)+\eta + i\nu} - 8\pi^3 p^3\left(\frac{2\pi}{\beta}(l+m+1)+\eta + i\nu\right)^{3/2}\right)\Bigg].$$
(A.27)

Evaluation

As a first step we examine the convergence of the sums over the Fermi poles for different temperatures. The results can be seen in Figure A.4. We can see again as expected, that the sums converge faster if the temperature is higher and that summing over twenty Fermi poles is sufficient in the evaluated temperature range.

Temperature dependence We plot the temperature dependence of the second contribution for three different frequencies in Figure A.5. As expected also this contribution is damped exponentially for higher temperatures.

ν-dependence We plot the ν-dependence of $\langle II \rangle_{\mathrm{Contr2}}$ in Figure A.6. The function exhibits a relative maximum before aspiring to a saturation value. To examine this behavior, we plot the contribution of the $\nu = \nu'$ and $\nu = -\nu'$ cases separately in Figure A.7.
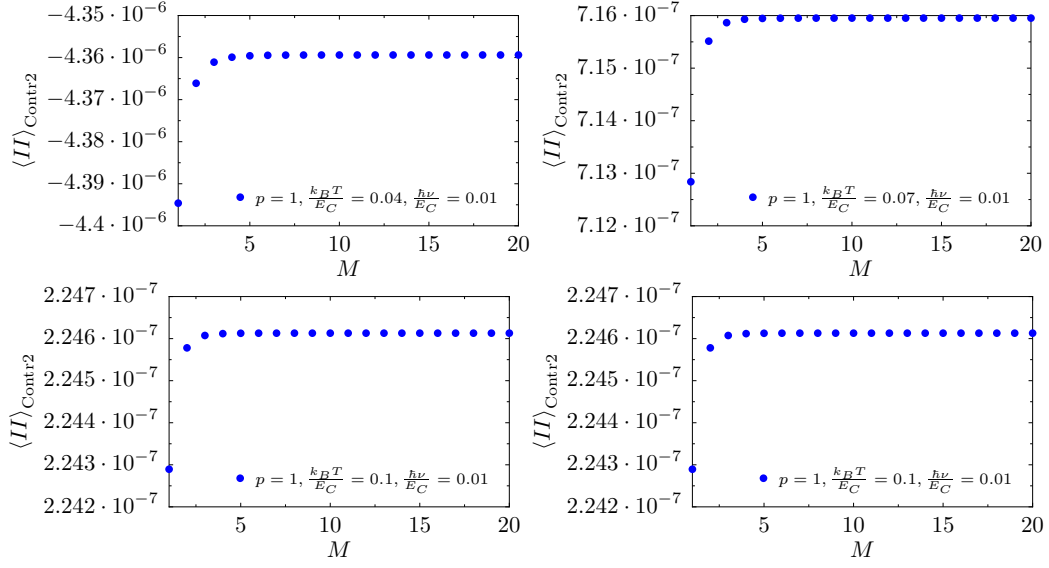
Figure A.4: Convergence of the second contribution for the sum over the Fermi poles for different temperatures in the case $\eta \to 0$.

A.4.2 Contribution 3

The third contribution takes the form

$$\langle II \rangle_{\text{Contr.3}} = \text{Re}\Bigg\{ \sum_{\nu,\nu'=\pm\nu} \int d\epsilon \int d\epsilon' \left(n(\epsilon) - n(\epsilon \pm \nu) \right) \left(n(\epsilon') - n(\epsilon' \pm \nu') \right)$$
$$\int dx \, \frac{2(x^2 + \eta)\, e^{-2\pi i p x}}{|x^2 + \eta - i(\epsilon - \epsilon')|^2 \, |x^2 + \eta - i(\epsilon - \epsilon' \pm \nu \mp \nu')|^2} \Bigg\} \qquad \text{(A.28)}$$

We will again discriminate the cases $\nu = \nu'$ and $\nu = -\nu'$ and start with the latter one.

$\nu = -\nu'$

As a first step we note, that the contributions of the cases $\nu - \nu' = \pm 2\nu$ are the same as one can see by shifting $\epsilon \to \epsilon - \nu$ and $\epsilon'- \to \epsilon' + \nu$. Thus we can concentrate on the case $\nu - \nu' = 2\nu$ and multiply the result by two. Introducing the abbreviations $a_1 = \sqrt{\eta - i(\epsilon - \epsilon')}$, $a_2 = \sqrt{\eta + i(\epsilon - \epsilon')}$, $a_3 = \sqrt{\eta - i(\epsilon - \epsilon' + \nu - \nu')}$ and $a_4 = \sqrt{\eta + i(\epsilon - \epsilon' + \nu - \nu')}$ turns the x-integral into

$$\int dx \frac{2(x^2 + \eta)\, e^{-2\pi i p x}}{|x^2 + \eta - i(\epsilon - \epsilon')|^2 \, |x^2 + \eta - i(\epsilon - \epsilon' + \nu - \nu')|^2} = \int dx \frac{2(x^2 + \eta)\, e^{-2\pi i p x}}{\prod_{j=1}^{4}(x + i a_j)(x - i a_j)} \, . \qquad \text{(A.29)}$$
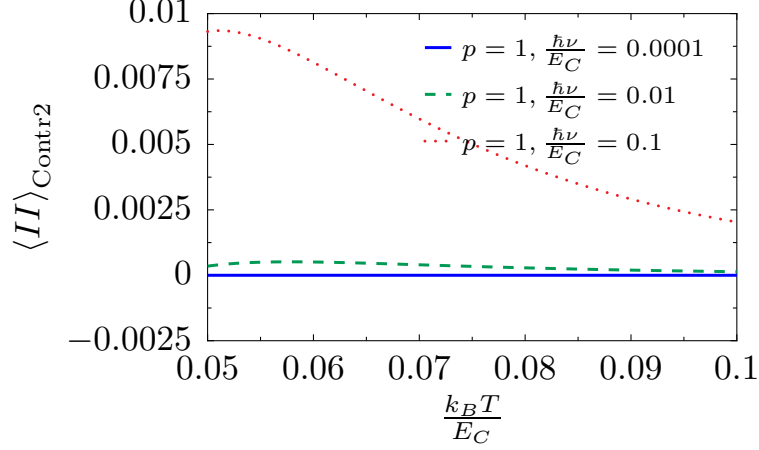
Figure A.5: Temperature dependence of contribution two for different values of the frequency in the case $\eta \to 0$.

We can close the integration contour in the lower plane again. Noting, that the poles at $-ia_j$ lie in the lower plane, we get

$$\int dx \frac{2(x^2 + \eta) e^{-2\pi i p x}}{\prod_{j=1}^{4}(x + ia_j)(x - ia_j)} = -2\pi i \sum_j \mathrm{Res}\left[\frac{2(x^2 + \eta) e^{-2\pi i p x}}{\prod_{j=1}^{4}(x + ia_j)(x - ia_j)}, x = -ia_j\right]$$

$$=$$

$$= \mathrm{Re}\left[\frac{\pi}{(\omega_1^2 - \omega_2^2)}\left[e^{-2\pi p\sqrt{\eta - i\omega_2}}(\eta - i\omega_2)^{-1/2} - e^{-2\pi p\sqrt{\eta - i\omega_1}}(\eta - i\omega_1)^{-1/2}\right]\right] \quad \text{(A.30)}$$

where we abbreviated $\omega_1 = \epsilon - \epsilon'$ and $\omega_2 = \epsilon - \epsilon' + 2\nu$. We see, that we can close the contour of the ϵ (ϵ')-integration in the upper (lower) plane again which yields

$$\langle II \rangle_{\text{Contr.3},\nu=-\nu'} = 2\left(\frac{2\pi}{\beta}\right)^2 \sum_{l,m=0}^{\infty}\left[f_{\nu-\nu'=2\nu,\text{Contr3}}\left(\frac{\pi i}{\beta}(2l+1), -\frac{\pi i}{\beta}(2m+1), p, \nu, \eta\right)\right.$$

$$- f_{\nu-\nu'=2\nu,\text{Contr3}}\left(\frac{\pi i}{\beta}(2l+1) - \nu, -\frac{\pi i}{\beta}(2m+1), p, \nu, \eta\right)$$

$$- f_{\nu-\nu'=2\nu,\text{Contr3}}\left(\frac{\pi i}{\beta}(2l+1), -\frac{\pi i}{\beta}(2m+1) + \nu, p, \nu, \eta\right)$$

$$\left. + f_{\nu-\nu'=2\nu,\text{Contr3}}\left(\frac{\pi i}{\beta}(2l+1) - \nu, -\frac{\pi i}{\beta}(2m+1) + \nu, p, \nu, \eta\right)\right] \quad \text{(A.31)}$$

where $f_{\nu+\nu'=2\nu,\text{Contr3}}(\epsilon, \epsilon', p, \nu, \eta)$ abbreviates the result of the x-integral in Eq. (A.30) and we introduced a factor of two accounting for the case $\nu - \nu' = -2\nu$, too.
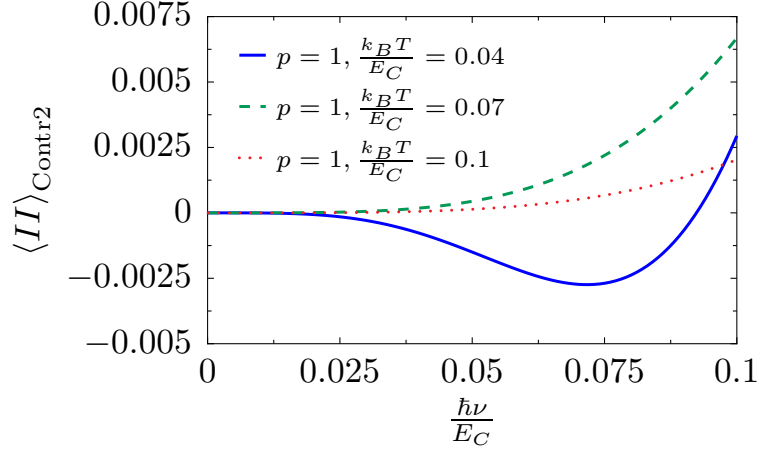
Figure A.6: Frequency dependence of $\langle II \rangle_{\text{Contr2}}$ for different temperatures in the case $\eta \to 0$. A plot over a wider range can be seen in Figure 4.13.

$$\nu = \nu'$$

Noting that the terms $\nu = \nu' = \pm \nu$ are equal, we start by performing the x-integration which goes along the lines of the previous cases and yields

$$\int dx \frac{2(x^2 + \eta) e^{-2\pi i p x}}{|x^2 + \eta - i(\epsilon - \epsilon')|^2 |x^2 + \eta - i(\epsilon - \epsilon' + \nu - \nu')|^2}$$
$$= \frac{i\pi}{(\epsilon - \epsilon')} \left[\frac{e^{-2\pi p \sqrt{\eta + i(\epsilon - \epsilon')}}}{(\eta + i(\epsilon - \epsilon'))^{3/2}} \left(1 + 2\pi p \sqrt{\eta + i(\epsilon - \epsilon')} \right) + \text{c.c.} \right] \tag{A.32}$$

We see, that we can close the contour of the ϵ (ϵ')-integration in the lower (upper) half this time. Defining

$$f_{\nu = \nu', \text{Contr3}}(\epsilon, \epsilon', p, \eta) = \frac{i\pi}{4(\epsilon - \epsilon')} \frac{e^{-2\pi p \sqrt{\eta + i(\epsilon - \epsilon')}}}{(\eta + i(\epsilon - \epsilon'))^{3/2}} \left(1 + 2\pi p \sqrt{\eta + i(\epsilon - \epsilon')} \right) \tag{A.33}$$

we get

$$\langle II \rangle_{\text{Contr.3}, \nu = \nu'} = 2 \operatorname{Re} \Bigg\{ \left(\frac{2\pi}{\beta} \right)^2 \sum_{m,l=0}^{\infty} \Bigg[f_{\nu = \nu', \text{Contr3}} \left(-\frac{\pi i}{\beta}(2l + 1), \frac{\pi i}{\beta}(2m + 1), p, , \eta \right)$$
$$- f_{\nu = \nu', \text{Contr3}} \left(-\frac{\pi i}{\beta}(2l + 1) - \nu, \frac{\pi i}{\beta}(2m + 1), p, \eta \right)$$
$$- f_{\nu = \nu'\nu, \text{Contr3}} \left(-\frac{\pi i}{\beta}(2l + 1), \frac{\pi i}{\beta}(2m + 1) - \nu, p, \eta \right)$$
$$+ f_{\nu = \nu, \text{Contr3}} \left(-\frac{\pi i}{\beta}(2l + 1) - \nu, \frac{\pi i}{\beta}(2m + 1) - \nu, p, \eta \right) \Bigg] \Bigg\}. \tag{A.34}$$
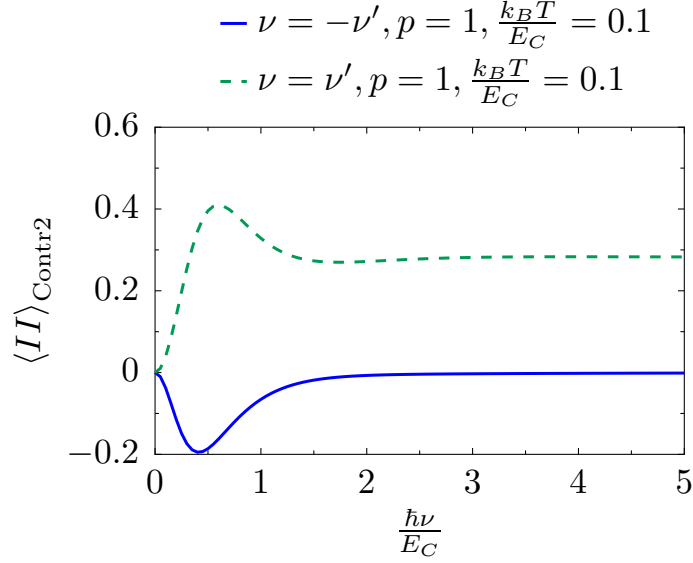
Figure A.7: Frequency dependence of $\langle II \rangle_{\text{Contr2}}$ splitted in the two cases $\nu = -\nu'$ and $\nu = \nu'$ for $\eta \to 0$.

$p = 0$-terms

In the third contribution also terms with $p = 0$ occur. Although the exponential factor is absent in this terms, the contour of the x-integration can still be closed in the lower half yielding the same result as in Eqs. (A.30) and (A.32) after setting $p = 0$. The exponential factors allowing to close the contours of the energy integrals are now absent. Instead we have to use the difference of the Fermi functions which take the form

$$n(\epsilon) - n(\epsilon + \nu) = \frac{1}{e^{\beta\epsilon} + 1} - \frac{1}{e^{\beta(\epsilon+\nu)} + 1} = \frac{e^{\beta\nu} + 1}{e^{\beta(\epsilon+\nu)} + 1 + e^{\beta\nu} + e^{-\beta\epsilon}}, \quad (A.35)$$

allowing us to close the contours in both planes. To avoid encircling other poles than the Fermi poles we close the contours in the same way as in the $p > 0$ case. The result of the calculation is the same as we would get from the $p > 0$ cases by taking the limit $p \to 0$.

Evaluation

We start evaluating contribution three by looking at the convergence of the sum over the Fermi poles both for the $p = 1$ term and the $p = 0$ term. The plots can be seen in Figure A.8 and A.9.

Temperature dependence The temperature dependence of the third contribution is plotted for different frequencies in Figure A.10. As expected the contribution is damped for high temperatures, too.

Frequency dependence The frequency dependence of the third contribution is plotted for different temperatures in Figure A.11.
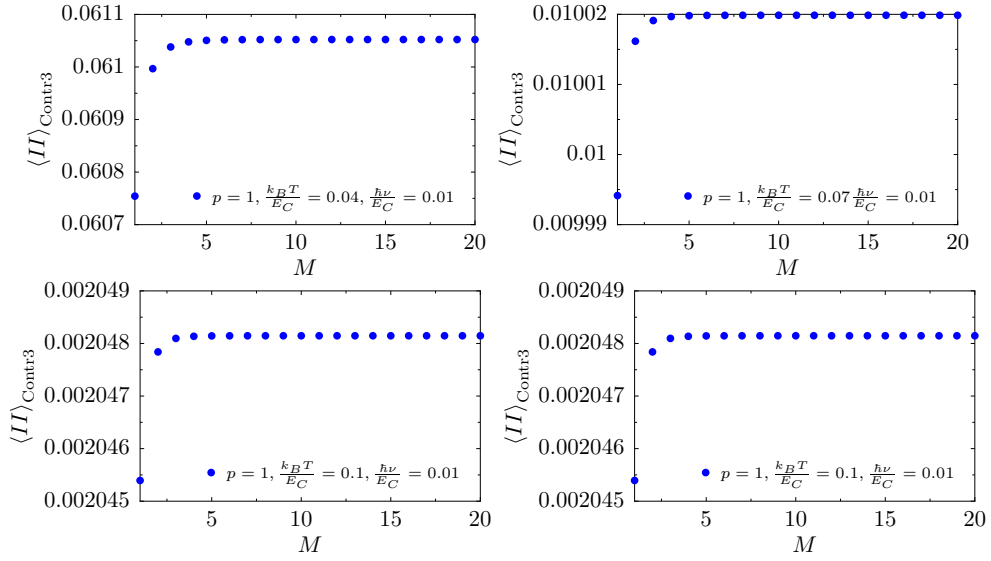
Figure A.8: Convergence of the third contribution for the sum over the Fermi poles for different temperatures in the case $\eta \to 0$.
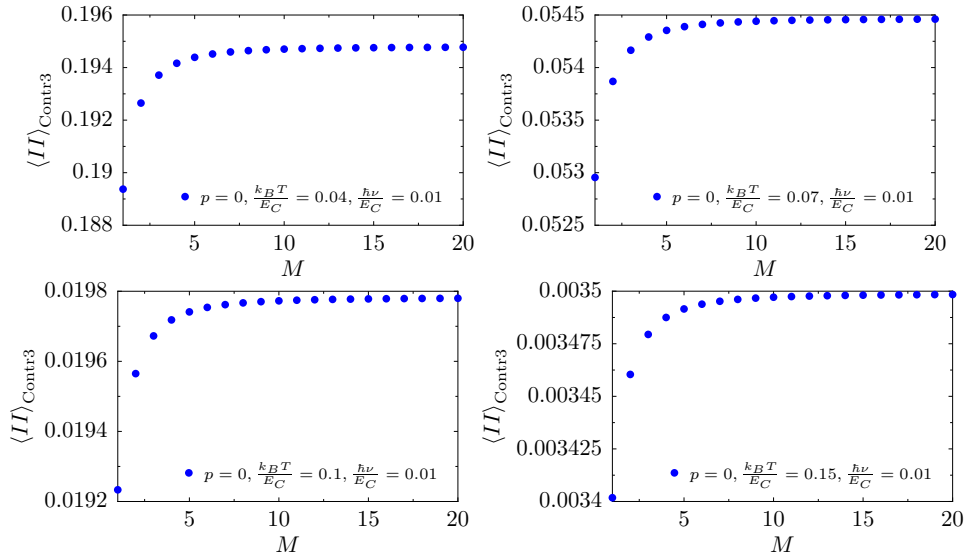
Figure A.9: Convergence of the $p = 0$ term of the third contribution for the sum over the Fermi poles for different temperatures in the case $\eta \to 0$.
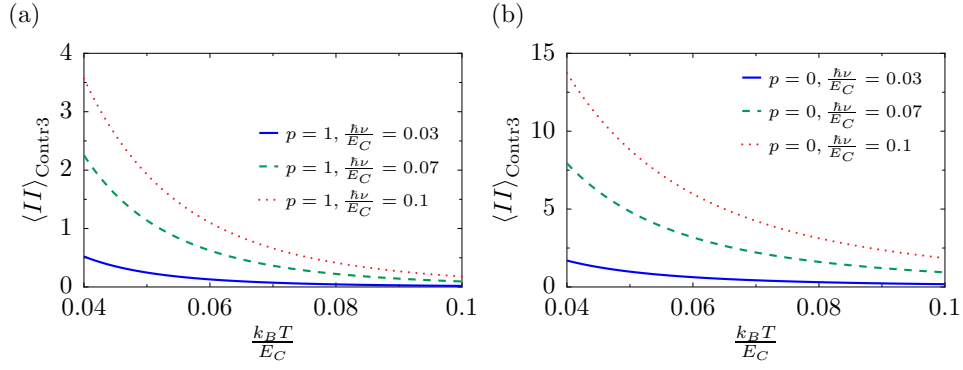
Figure A.10: Temperature dependence of contribution three for different values of the frequency in the case $\eta \to 0$ for $p = 1$ (a) and $p = 0$ (b).
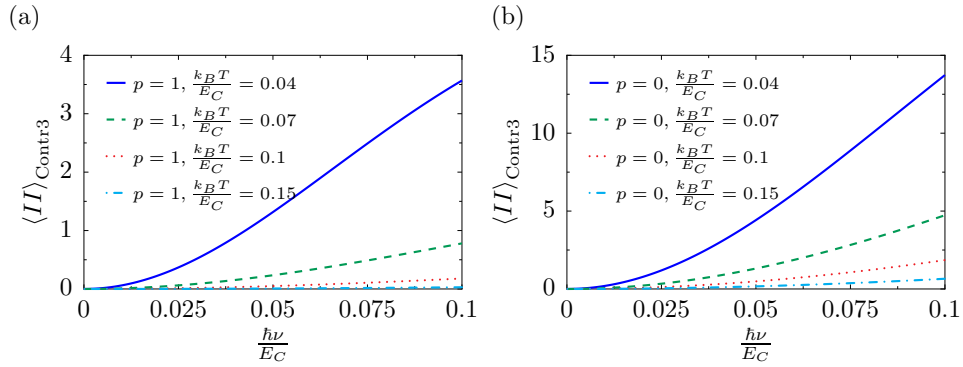
Figure A.11: Frequency dependence of contribution three for different values of the Temperature in the case $\eta \to 0$ for $p = 1$ (a) and $p = 0$ (b). A wider region is plotted for in Figure 4.13.

Appendix B

Additional calculations to the basic formalism of quantum dots

B.1 Charging energy of a SEB

The charging energy in a single electron box which can be seen in Figure 6.1 is $\frac{Q_J^2}{2C_J} + \frac{Q_G^2}{2C_G}$. To get the relevant free energy we have to perform a Legendre transformation from the charge variables to n and V_G and also have to add the work $-V_G Q_G$ done by the voltage source. So the starting point is

$$E_{\text{ch}} = \frac{Q_J^2}{2C_J} + \frac{Q_G^2}{2C_G} + V_G Q_G\,, \tag{B.1}$$

where $Q_{J/G}$ is the charge on the gate/tunnel junction. The number of excess electrons on the dot is given by the sum of the charges on the two capacitor plates,

$$-ne = Q_J + Q_G\,, \tag{B.2}$$

and the gate voltage V_G is equal to the voltage drop over the island,

$$V_G = \frac{Q_J}{C_J} - \frac{Q_G}{C_G}\,. \tag{B.3}$$

Combining the last two equations and solve for the charges gives

$$
\begin{aligned}
Q_J &= C_J \frac{C_G V_G - ne}{C_J + C_G}\,,\\
Q_G &= -C_G \frac{C_J V_G + ne}{C_J + C_G}\,.
\end{aligned}
\tag{B.4}
$$

Introducing the total capacitance $C = C_J + C_G$ and replacing the charges in Eq. (B.1) leads to the expression

$$E_{\text{ch}} = \frac{(n - C_G V_G)^2}{2C} + f(V_G)\,, \tag{B.5}$$

where $f(V_G)$ is a function of the gate voltage which is dropped in Eq. (6.1) since it does not depend on n.

B.2 Charging energy of a SET

Using the the nomenclature from Figure 6.3 we ca write the charging energy before performing the Legendre transformation as

$$E_{\text{ch}} = \frac{Q_L^2}{2C_L} + \frac{Q_R^2}{2C_R} + \frac{Q_G^2}{2C_G} + V_G Q_G + V_L Q_L + V_R Q_R \,. \tag{B.6}$$

According to Kirchhoffs' voltage law the directed sum of the voltage around any closed circuit has to be zero, which leads us to the three equations

$$V_L - \frac{Q_L}{C_L} + \frac{Q_R}{C_R} - V_R = 0 \,,$$
$$V_L - \frac{Q_L}{C_L} + \frac{Q_G}{C_G} - V_G = 0 \,,$$
$$V_G - \frac{Q_G}{C_G} + \frac{Q_R}{C_R} - V_R = 0 \,. \tag{B.7}$$

Solving this for potential differences gives

$$V_L - V_R = \frac{Q_L}{C_L} - \frac{Q_R}{C_R} \,,$$
$$V_L - V_G = \frac{Q_L}{C_L} - \frac{Q_G}{C_G} \,,$$
$$V_G - V_R = \frac{Q_G}{C_G} - \frac{Q_R}{C_R} \,. \tag{B.8}$$

Together with the condition, that the charge on the island is the sum of the charges on the capacitors, $-ne = Q_L + Q_R + Q_G$, we can solve this equation for $Q_{L/R/G}$, getting

$$Q_L = \frac{C_L}{C} \left[-ne + C_G(V_L - V_G) + C_R(V_L - V_R) \right] \,,$$
$$Q_G = \frac{C_G}{C} \left[-ne + C_L(V_G - V_L) - C_R(V_R - V_G) \right] \,,$$
$$Q_R = \frac{C_R}{C} \left[-ne - C_G(V_G - V_R) - C_L(V_L - V_R) \right] \,, \tag{B.9}$$

where we introduced the total capacitance $C = C_L + C_R + C_G$. Inserting this into Eq. (B.6), sorting by powers of n, and shortcutting a term $f(V_G, V_L, V_R)$ which does not depend on n again yields

$$E_{\text{ch}} = \frac{(ne - C_G V_G)^2}{2C} + f(V_G, V_L, V_R) \,. \tag{B.10}$$

Thus the charging energy on the SET has the same form as the one of the SEB, but includes an additional capacitance in the total capacitance C.

B.3   Lang-Firsov transformation

The Lang-firsov transformation is a canonical transformation of the form

$$H' = e^S H e^{-S} \, . \tag{B.11}$$

The generator S of the must be anti-self-adjoint, $S = -S^\dagger$ in order to keep H' hermitian,

$$H'^\dagger = \left(e^S H e^{-S}\right)^\dagger = e^{-S^\dagger} H^\dagger e^{S^\dagger} = e^S H e^{-S} = H' \, . \tag{B.12}$$

We choose S according to [81] to be

$$S = \lambda(b^\dagger - b)n_d \, . \tag{B.13}$$

For calculation of the new operators we have to use the Baker-Campbell-Hausdorff (BCH) formula. Since not all operators commute with the relevant commutators, we have to use the whole BCH series[1]

$$e^S \mathcal{O} e^{-s} = \sum_n = 0^\infty \frac{1}{n!} \left[S, \mathcal{O}\right]_n \, , \tag{B.14}$$

where $\mathcal{O}$ is an operator and $[S, \mathcal{O}]_n$ is the n-fold commutator

$$[S, \mathcal{O}]_n = \underbrace{\left[S, \left[S, \dots \left[S, \mathcal{O}\right]_- \dots\right]_-\right]_-}_{n \, \mathrm{times}} \, , \tag{B.15}$$

and $[S, \mathcal{O}]_0 = \mathcal{O}$. With the commutators $\left[b^\dagger - b, b\right]_- = -1$ and $[n_d, d_\sigma]_- = (-1)^n d_\sigma$ we get

$$\begin{aligned}
d_\sigma'^{(\dagger)} &= d_\sigma^{(\dagger)} \, e^{\lambda(b - b^\dagger)} \, , \\
b'^{(\dagger)} &= b^{(\dagger)} - \lambda n_d \, , \\
c_{\alpha \boldsymbol{p} \sigma}'^{(\dagger)} &= c_{\alpha \boldsymbol{p} \sigma}^{(\dagger)} \, , \quad \text{and} \\
n_d' &= n_d \, .
\end{aligned} \tag{B.16}$$

The transformed Hamiltonian turns into $H' = H'_{\mathrm{dot}} + H'_{\mathrm{leads}} + H'_{\mathrm{tun}}$ with

$$\begin{aligned}
H'_{\mathrm{dot}} &= (\epsilon_d - \lambda^2 \hbar \omega_0)n_d + (U - 2\lambda^2 \hbar \omega_0)n_{d\uparrow} n_{d\downarrow} + \hbar \omega_0 b^\dagger b \, , \\
H'_{\mathrm{leads}} &= \sum_{\alpha \boldsymbol{p} \sigma} \epsilon_{\alpha \boldsymbol{p}} c_{\alpha \boldsymbol{p} \sigma}^\dagger c_{\alpha \boldsymbol{p} \sigma} \, , \quad \text{and} \\
H'_{\mathrm{tun}} &= \sum_{\alpha \boldsymbol{p} \sigma} \left(t_{\alpha \boldsymbol{p}} \, e^{-\lambda(b^\dagger - b)} c_{\alpha \boldsymbol{p} \sigma}^\dagger d_\sigma + t_{\alpha \boldsymbol{p}}^* \, e^{\lambda(b^\dagger - b)} d_\sigma^\dagger c_{\alpha \boldsymbol{p} \sigma}\right) \, .
\end{aligned} \tag{B.17}$$

we see, that the energies transform in the way we expected from the argument in section 6.2.3, and the tunneling matrix elements are shifted as $t_{\alpha \boldsymbol{p}} \to t_{\alpha \boldsymbol{p}} \, e^{-\lambda(b^\dagger - b)}$.

---

[1]To be exact, Eq. (B.14) is called Hadamard-Lemma; the BCH formla reads $e^A e^B = e^B e^A e^{[A,B]_-}$ and is valid if the operators A and B commute with their commutator.

Bibliography

[1] S. Datta, *Electronic transport in mesoscopic systems (cambridge studies in semi-conductor physics and microelectronic engineering)*, Cambridge University Press, 5 1997.

[2] E. Akkermans and G. Montambaux, *Mesoscopic physics of electrons and photons*, reissue ed., Cambridge University Press, 7 2011.

[3] F. Hund, *Calculations concerning the magnetic behavior of small metallic particles at low temperatures*, Annalen der Physik **5** (1996), no. 1, 1–12 (English, Reprinted from the Annalen der Physik, vol 32, pg 102, 1938).

[4] M. Büttiker, Y. Imry, and R. Landauer, *Josephson behavior in small normal one-dimensional rings*, Physics Letters A **96** (1983), no. 7, 365 – 367.

[5] E. K. Riedel and F. von Oppen, *Mesoscopic persistent current in small rings*, Phys. Rev. B **47** (1993), 15449–15459.

[6] V. I. Fal'ko and D. E. Khmle'nitskii, *Mesoscopic photovoltaic effect in microjunctions*, Zh. Eksp. Teor. Fiz. **95** (1989), 328–337.

[7] I. A. Dmitriev, M. G. Vavilov, I. L. Aleiner, A. D. Mirlin, and D. G. Polyakov, *Theory of microwave-induced oscillations in the magnetoconductivity of a two-dimensional electron gas*, Phys. Rev. B **71** (2005), 115316.

[8] C. Joas, J. Dietel, and F. von Oppen, *Microwave photoconductivity of a modulated two-dimensional electron gas due to intra-landau-level transitions*, Phys. Rev. B **72** (2005), 165323.

[9] E. Mariani and F. von Oppen, *Electron-vibron coupling in suspended carbon nanotube quantum dots*, Phys. Rev. B **80** (2009), 155411.

[10] J. Koch, M. E. Raikh, and F. von Oppen, *Pair tunneling through single molecules*, Phys. Rev. Lett. **96** (2006), 056803.

[11] F. Bloch, *Off-diagonal long-range order and persistent currents in a hollow cylinder*, Phys. Rev. **137** (1965), A787–A795.

[12] I. O. Kulik, *Magnetic flux quantization in the normal state*, Sov. Phys. JETP **31** (1970), 1172.

[13] H. Bouchiat, *New clues in the mystery of persistent currents*, Physics **1** (2008), 7.

[14] A. C. Bleszynski-Jayich, W. E. Shanks, B. Peaudecerf, E. Ginossar, F. von Oppen, L. Glazman, and J. G. E. Harris, *Persistent currents in normal metal rings*, Science **326** (2009), no. 5950, 272–275.

[15] L. P. Lévy, G. Dolan, J. Dunsmuir, and H. Bouchiat, *Magnetization of mesoscopic copper rings: Evidence for persistent currents*, Phys. Rev. Lett. **64** (1990), 2074–2077.

[16] V. Chandrasekhar, R. A. Webb, M. J. Brady, M. B. Ketchen, W. J. Gallagher, and A. Kleinsasser, *Magnetic response of a single, isolated gold loop*, Phys. Rev. Lett. **67** (1991), 3578–3581.

[17] E. M. Q. Jariwala, P. Mohanty, M. B. Ketchen, and R. A. Webb, *Diamagnetic persistent current in diffusive normal-metal rings*, Phys. Rev. Lett. **86** (2001), 1594–1597.

[18] H. Bluhm, N. C. Koshnick, Julie A. Bert, M. E. Huber, and K. A. Moler, *Persistent currents in normal metal rings*, Phys. Rev. Lett. **102** (2009), 136802.

[19] J. Rammer and H. Smith, *Quantum field-theoretical methods in transport theory of metals*, Rev. Mod. Phys. **58** (1986), 323–359.

[20] L. V. Keldysh, *Diagram technique for nonequilibrium processes*, Sov. Phys. JETP **20** (1975), 1018.

[21] N. Byers and C. N. Yang, *Theoretical considerations concerning quantized magnetic flux in superconducting cylinders*, Phys. Rev. Lett. **7** (1961), 46–49.

[22] R. Landauer, *Irreversibility and heat generation in the computing process*, IBM Journal of Research and Development **5** (1961), no. 3, 183–191.

[23] E. Ginossar, L. I. Glazman, T. Ojanen, F. von Oppen, W. E. Shanks, A. C. Bleszynski-Jayich, and J. G. E. Harris, *Mesoscopic persistent currents in a strong magnetic field*, Phys. Rev. B **81** (2010), 155448.

[24] V. Ambegaokar and U. Eckern, *Coherence and persistent currents in mesoscopic rings*, Phys. Rev. Lett. **65** (1990), 381–384.

[25] N.W. Ashcroft and N. D. Mermin, *Solid state physics*, 1 ed., Brooks Cole, 1 1976.

[26] H. Bary-Soroker, O. Entin-Wohlman, and Y. Imry, *Effect of pair breaking on mesoscopic persistent currents well above the superconducting transition temperature*, Phys. Rev. Lett. **101** (2008), 057001.

[27] P. G. Björnsson, B. W. Gardner, J. R. Kirtley, and K. A. Moler, *Scanning superconducting quantum interference device microscope in a dilution refrigerator*, Review of Scientific Instruments **72** (2001), 4153.

[28] M. E. Huber, N. C. Koshnick, H. Bluhm, L. J. Archuleta, T. Azua, P. G. Björnsson, B. W. Gardner, S. T. Halloran, E. A. Lucero, and K. A. Moler, *Gradiometric microsquid susceptometer for scanning measurements of mesoscopic samples*, Review of Scientific Instruments **79** (2008), 053704.

[29] N. C. Koshnick, H. Bluhm, M. E. Huber, and K. A. Moler, *Fluctuation superconductivity in mesoscopic aluminum rings*, Science **318** (2007), no. 5855, 1440–1443.

[30] A. C. Bleszynski-Jayich, W. E. Shanks, B. Peaudecerf, E. Ginossar, F. von Oppen, L. Glazman, and J. G. E. Harris, *Supporting online material for persistent currents in normal metal rings*, Science **326**, no. 5950.

[31] D. Mailly, C. Chapelier, and A. Benoit, *Experimental observation of persistent currents in gaas-algaas single loop*, Phys. Rev. Lett. **70** (1993), 2020–2023.

[32] V. E. Kravtsov and B. L. Altshuler, *Relationship between the noise-induced persistent current and the dephasing rate*, Phys. Rev. Lett. **84** (2000), 3394–3397.

[33] A. I. Larkin and Yu. N. Ovchinnikov, *Nonlinear conductivity of superconductors in the mixed state*, Zh. Eksp. Teor. Fiz **68** (1975), 1915.

[34] G. C. Wick, *The evaluation of the collision matrix*, Phys. Rev. **80** (1950), 268–272.

[35] A. A. Abrikosov, *Methods of quantum field theory in statistical physics (dover books on physics)*, revised ed., Dover Publications, 10 1975.

[36] S. Hikami, *Anderson localization in a nonlinear-σ-model representation*, Phys. Rev. B **24** (1981), 2671–2679.

[37] B. L. Altshuler, A. G. Aronov, and D. E. Khmelnitsky, *Effects of electron-electron collisions with small energy transfers on quantum localisation*, Journal of Physics C: Solid State Physics **15** (1982), no. 36, 7367.

[38] P. A. M. Dirac, *The quantum theory of the emission and absorption of radiation*, Royal Society of London Proceedings Series A **114** (1927), 243–265.

[39] A. I. Larkin and D. E. Khmle'nitskii, *Mesoscopic fluctuations of current-voltage characteristics*, Zh. Eksp. Teor. Fiz. **91** (1986), 1815–1819.

[40] T. Ludwig, Ya. M. Blanter, and A. D. Mirlin, *Nonequilibrium mesoscopic conductance fluctuations*, Phys. Rev. B **70** (2004), 235315.

[41] M. A. Reed, J. N. Randall, R. J. Aggarwal, R. J. Matyi, T. M. Moore, and A. E. Wetsel, *Observation of discrete electronic states in a zero-dimensional semiconductor nanostructure*, Phys. Rev. Lett. **60** (1988), 535–537.

[42] P. A. Maksym and T. Chakraborty, *Quantum dots in a magnetic field: Role of electron-electron interactions*, Phys. Rev. Lett. **65** (1990), 108–111.

[43] M. A. Reed, *Quantum dots*, Scientific American **268** (1993), no. 1, 118–123 (English).

[44] G. E. Moore, *Cramming more components onto integrated circuits*, Electronics Magazine **38** (1965).

[45] R. E. Howard, P. F. Liao, W. J. Skocpol, L. D. Jackel, and H. G. Craighead, *Microfabrication as a scientific tool*, Science **221** (1983), no. 4606, 117–121.

[46] J. Alsmeier, E. Batke, and J. P. Kotthaus, *Voltage-tunable quantum dots on silicon*, Phys. Rev. B **41** (1990), 1699–1702.

[47] S. J. Allen, H. L. Störmer, and J. C. M. Hwang, *Dimensional resonance of the two-dimensional electron gas in selectively doped gaas/algaas heterostructures*, Phys. Rev. B **28** (1983), 4875–4877.

[48] J. J. Cuomo A. N. Broers, W. W. Molzen and N. D. Wittels, *Electron-beam fabrication of 80-a metal structures*, Appl. Phys. Lett. **29** (1976), 596.

[49] H. G. Craighead, *10-nm resolution electron-beam lithography*, J. Appl. Phys. **55** (1984), 4430.

[50] K. Bradshaw W. M. Duncan W. R. Frensley J. W. Lee M. A. Reed, R. T. Bate and H. D. Shih, *Spatial quantization in gaas-algaas multiple quantum dots*, J. Vac. Sci. Technol. B **4** (1986), 358.

[51] R. G. Wheeler, K. K. Choi, A. Goel, R. Wisnieff, and D. E. Prober, *Localization and electron-electron interaction effects in submicron-width inversion layers*, Phys. Rev. Lett. **49** (1982), 1674–1677.

[52] T. J. Thornton, M. Pepper, H. Ahmed, D. Andrews, and G. J. Davies, *One-dimensional conduction in the 2d electron gas of a gaas-algaas heterojunction*, Phys. Rev. Lett. **56** (1986), 1198–1201.

[53] K. S. Ralls, W. J. Skocpol, L. D. Jackel, R. E. Howard, L. A. Fetter, R. W. Epworth, and D. M. Tennant, *Discrete resistance switching in submicrometer silicon inversion layers: Individual interface traps and low-frequency ($\frac{1}{f}$) noise*, Phys. Rev. Lett. **52** (1984), 228–231.

[54] W. J. Skocpol, P. M. Mankiewich, R. E. Howard, L. D. Jackel, D. M. Tennant, and A. Douglas Stone, *Universal conductance fluctuations in silicon inversion-layer nanostructures*, Phys. Rev. Lett. **56** (1986), 2865–2868.

[55] R. C. Jaklevic and J. Lambe, *Molecular vibration spectra by electron tunneling*, Phys. Rev. Lett. **17** (1966), 1139–1140.

[56] L. I. Glazman and R. I. Shekhter, *Inelastic tunneling of electrons through a potential barrier*, Sov. Phys. JETP **67**, 163.

[57] N. S. Wingreen, K. W. Jacobsen, and J. W. Wilkins, *Resonant tunneling with electron-phonon interaction: An exactly solvable model*, Phys. Rev. Lett. **61** (1988), 1396–1399.

[58] M. A. Reed, C. Zhou, C. J. Muller, T. P. Burgin, and J. M. Tour, *Conductance of a molecular junction*, Science **278** (1997), no. 5336, 252–254.

[59] H. Park, J. Park, A. K. L. Lim, E. H. Anderson, A. P. Alivisatos, and P. L. McEuen, *Nanomechanical oscillations in a single-c-60 transistor*, Nature **407** (2000), no. 6800, 57–60 (English).

[60] R. Leturcq, C. Stampfer, K. Inderbitzin, L. Durrer, C. Hierold, E. Mariani, M. G. Schultz, F. von Oppen, and K. Ensslin, *Franck-condon blockade in suspended carbon nanotube quantum dots*, Nature Physics **5** (2009), no. 5, 327–331.

[61] J. Koch, E. Sela, Y. Oreg, and F. von Oppen, *Nonequilibrium charge-kondo transport through negative-u molecules*, Phys. Rev. B **75** (2007), 195402.

[62] T. Ojanen, F. C. Gethmann, and F. von Oppen, *Electromechanical instability in vibrating quantum dots with effectively negative charging energy*, Phys. Rev. B **80** (2009), 195103.

[63] R. A. Millikan, *A new modification of the cloud method of determining the elementary electrical charge and the most probable value of that charge*, Phys. Mag. **19**, 209.

[64] T. Dittrich, P. Hänggi, G.-L. Ingold, B. Kramer, G. Schön, and W. Zwerger, *Quantum transport and dissipation*, 1 ed., Wiley-VCH, 3 1998.

[65] M. H. Devoret, D. Esteve, and C. Urbina, *Single-electron transfer in metallic nanostructures*, Nature **360** (1992), no. 6404, 547–553 (English).

[66] H. Grabert and M. H. Devoret (eds.), *Single charge tunneling: Coulomb blockade phenomena in nanostructures (nato science series b: Physics)*, 1 ed., Springer, 6 1992.

[67] G. Cuniberti, G. Fagas, and K. Richter (eds.), *Introducing molecular electronics (lecture notes in physics)*, 1 ed., Springer, 12 2005.

[68] J. König, H. Schoeller, and G. Schön, *Zero-bias anomalies and boson-assisted tunneling through quantum dots*, Phys. Rev. Lett. **76** (1996), 1715–1718.

[69] J. König, J. Schmid, H. Schoeller, and G. Schön, *Resonant tunneling through ultrasmall quantum dots: Zero-bias anomalies, magnetic-field dependence, and boson-assisted transport*, Phys. Rev. B **54** (1996), 16820–16837.

[70] K. Mullen, E. Ben-Jacob, R. C. Jaklevic, and Z. Schuss, *I -V characteristics of coupled ultrasmall-capacitance normal tunnel junctions*, Phys. Rev. B **37** (1988), 98–105.

[71] A. Aviram and M. A. Ratner, *Molecular rectifiers*, Chemical Physics Letters **29** (1974), no. 2, 277 – 283.

[72] N. B. Zhitenev, H. Meng, and Z. Bao, *Conductance of small molecular junctions*, Phys. Rev. Lett. **88** (2002), 226801.

[73] X. H. Qiu, G. V. Nazin, and W. Ho, *Vibronic states in single molecule electron transport*, Phys. Rev. Lett. **92** (2004), 206102.

[74] D.-H. Chae, J. F. Berry, S. Jung, F. A. Cotton, C. A. Murillo, and Z. Yao, *Vibrational excitations in single trimetal-molecule transistors*, Nano Letters **6** (2006), no. 2, 165–168.

[75] J. Koch and F. von Oppen, *Franck-condon blockade and giant fano factors in transport through single molecules*, Phys. Rev. Lett. **94** (2005), 206804.

[76] J. Koch, M. E. Raikh, and F. von Oppen, *Full counting statistics of strongly non-ohmic transport through single molecules*, Phys. Rev. Lett. **95** (2005), 056801.

[77] J. Koch, F. von Oppen, and A. V. Andreev, *Theory of the franck-condon blockade regime*, Phys. Rev. B **74** (2006), 205438.

[78] A. Mitra, I. Aleiner, and A. J. Millis, *Phonon effects in molecular transistors: quantal and classical treatment*, Phys. Rev. B **69** (2004), 245302.

[79] S. Braig and K. Flensberg, *Vibrational sidebands and dissipative tunneling in molecular transistors*, Phys. Rev. B **68** (2003), 205324.

[80] M. R. Wegewijs and K. C. Nowack, *Nuclear wavefunction interference in single-molecule electron transport*, New Journal of Physics **7** (2005), no. 1, 239+.

[81] I. G. Lang and Y. A. Firsov, *Kinetic theory of semiconductors with low mobility*, Sov. Phys. JETP **16**, 1301.

[82] J. Koch, *Quantum transport through single-molecule devices*, 2006.

[83] P. W. Anderson, *Model for the electronic structure of amorphous semiconductors*, Phys. Rev. Lett. **34** (1975), 953–955.

[84] A. S. Alexandrov, A. M. Bratkovsky, and R. Stanley Williams, *Bistable tunneling current through a molecular quantum dot*, Phys. Rev. B **67** (2003), 075301.

[85] A. S. Alexandrov and A. M. Bratkovsky, *Memory effect in a molecular quantum dot with strong electron-vibron interaction*, Phys. Rev. B **67** (2003), 235312.

[86] P. S. Cornaglia, H. Ness, and D. R. Grempel, *Many-body effects on the transport properties of single-molecule devices*, Phys. Rev. Lett. **93** (2004), 147201.

[87] P. S. Cornaglia, D. R. Grempel, and H. Ness, *Quantum transport through a deformable molecular transistor*, Phys. Rev. B **71** (2005), 075320.

[88] P. S. Cornaglia and D. R. Grempel, *Magnetoconductance through a vibrating molecule in the kondo regime*, Phys. Rev. B **71** (2005), 245326.

[89] L. Arrachea and M. J. Rozenberg, *Quantum monte carlo method for models of molecular nanodevices*, Phys. Rev. B **72** (2005), 041301.

[90] J. Mravlje, A. Ramšak, and T. Rejec, *Conductance of deformable molecules with interaction*, Phys. Rev. B **72** (2005), 121403.

[91] K. Charoenkwan and D. H. Evans, *Investigation of potential inversion in the reduction of 9,10-dinitroanthracene and 3,6-dinitrodurene*, Journal of Electroanalytical Chemistry **565** (2004), no. 1, 29 – 35.

[92] S. Sapmaz, P. Jarillo-Herrero, Ya. M. Blanter, C. Dekker, and H. S. J. van der Zant, *Tunneling in suspended carbon nanotubes assisted by longitudinal phonons*, Phys. Rev. Lett. **96** (2006), 026801.

[93] B. J. LeRoy, S. G. Lemay, J. Kong, and C. Dekker, *Electrical generation and absorption of phonons in carbon nanotubes*, Nature **432** (2004), no. 7015, 371–374.

[94] F. Kuemmeth, S. Ilani, D. C. Ralph, and P. L. McEuen, *Coupling of spin and orbital motion of electrons in carbon nanotubes*, Nature **452** (2008), no. 7186, 448–452.

[95] A. K. Hüttel, M. Poot, B. Witkamp, and H. S. J. van der Zant, *Nanoelectromechanics of suspended carbon nanotubes*, New Journal of Physics **10** (2008), no. 9, 095003.

[96] V. Sazonova, Y. Yaish, H. Ustunel, D. Roundy, T. A. Arias, and P. L. McEuen, *A tunable carbon nanotube electromechanical oscillator*, Nature **431** (2004), no. 7006, 284–287.

[97] A. Naik, O. Buu, M. D. LaHaye, A. D. Armour, A. A. Clerk, M. P. Blencowe, and K. C. Schwab, *Cooling a nanomechanical resonator with quantum back-action*, Nature **443** (2006), no. 7108, 193–196.

[98] F. Pistolesi and S. Labarthe, *Current blockade in classical single-electron nanomechanical resonator*, Phys. Rev. B **76** (2007), 165317.

[99] J. R. Schrieffer and P. A. Wolff, *Relation between the anderson and kondo hamiltonians*, Phys. Rev. **149** (1966), 491–492.

[100] H.-B. Schüttler and A. J. Fedro, *Effective strong-coupling hamiltonians for bipolaron centers and magnetic impurities with on-site electron-phonon coupling*, Phys. Rev. B **38** (1988), 9063–9068.

[101] D. Pines, *Theory of quantum liquids, volume i: Normal fermi liquids (advanced books classics)*, Westview Press, 3 1994.

[102] C. W. J. Beenakker, *Theory of coulomb-blockade oscillations in the conductance of a quantum dot*, Phys. Rev. B **44** (1991), 1646–1656.

Acknowledgements

Summary

In this thesis we investigate two distinct mesoscopic systems which are driven out of equilibrium. This implies that we have to go beyond first order perturbation theory to describe the expected properties of their physical quantities.

In the first part of the thesis we consider mesoscopic non-superconducting metal rings which are known for exhibiting persistent currents, i.e. perpetual currents flowing in the rings without an applied voltage, in the absence of time reversal symmetry. We assume the electronic distribution in the system to be driven out of equilibrium by applying an additional microwave field and analyze the effect on the physical quantities accessible for experimental investigations. In order to avoid effects arising from the direct influence of the microwave field on the electronic motion in the rings, we hereby restrict ourselves to the situation where the microwave field stands perpendicular to the ring. In this case it turns out that the fourth order in the interaction of the electrons with the field is the lowest non-vanishing order correction to the relevant quantities, i.e. the typical current and the current-current correlation function.

We discriminate between two distinct physical processes, one arising from fluctuations of the density of states caused by the microwave field and the other from a photovoltaic effect conditioned by local symmetry breaking due to the random distribution of impurities in the rings. Our analysis shows that the effect of the former process on the considered physical quantities is orders of magnitudes larger than the effect of the latter contribution. Further it is possible to obtain an effect which is of the same order of magnitude – or even larger – than the equilibrium persistent current by choosing certain field amplitudes and frequencies that lie well within the region of the assumptions of our perturbative approach. We argue that it should thus be possible to observe the calculated effects experimentally and provide suitable experimental configurations.

The second part of the thesis deals with quantum dots in which the electronic degrees of freedom are assumed to be strongly coupled to a vibrational mode. This coupling causes a shift in the tunneling matrix elements, leading e.g. to the formation of vibrational sidebands in the I-V characteristics of the quantum dot. Furthermore the coupling to a vibrational mode causes a renormalization of the charging energy, which is the energy needed to add another electron to the dot. We analyze a situation where the coupling of the quantum dot to the vibrational mode is so strong that the renormalized charging energy becomes not only negative ("negative-U regime"), but also overcomes the cost in single-particle energy due to finite level spacing. This leads to an instability in the system which can be regularized by adding an anharmonic term to the vibron energy.

We find that the effective potential in this situation differs qualitatively from the case

with positive charging energy, leading to modifications of the low temperature properties in the Coulomb blockade regime. The system develops e.g. rapid changes in the average and the fluctuations of the number of excess electrons in the neighborhood of zero gate charge. We argue that the negative-U regime analyzed can be experimentally accessible using carbon nanotube quantum dots which are known for exhibiting strong electron-vibron coupling.

Kurzfassung

In dieser Arbeit werden zwei verschiedene mesoskopische Systeme im Nichtgleichgewicht untersucht. Nichtgleichgewicht bedeutet dabei, dass explizit höhere Ordnungen in der jeweiligen Störungstheorie berücksichtigt werden müssen um die charakteristischen physikalischen Größen der Systeme zu beschreiben.

Der erste Teil der Arbeit widmet sich mesoskopisch kleinen Ringen, welche im Gleichgewicht Dauerströme ausbilden, wenn die Zeitumkehrinvarianz in den Ringen gebrochen wird. Es wird angenommen, dass ein zusätzliches Mikrowellenfeld angelegt wird, welches das System aus dem Gleichgewicht auslenkt und die Auswirkung auf experimentell zugängliche physikalische Größen – den typischen Strom und die Strom-Strom Korrelationsfunktion – berechnet. Hierbei wird angenommen, dass das Mikrowellenfeld senkrecht zur Ebene der Ringe steht um Effekte zu vermeiden, die durch den direkten Einfluss des Feldes auf die Bahn der Elektronen in den Ringen entstehen. Da die Feld-induzierte Korrektur des Stromes in erster und die Korrektur der Korrelationsfunktion in zweiter und dritter Ordnung Störungstheorie verschwinden, ergibt es sich, dass typischer Strom und Korrelationsfunktion in der vierten Ordnung Störungstheorie berechnet werden müssen.

Zu der durch das Mikrowellenfeld induzierten Änderung von typischem Strom und Korrelationsfunktion tragen zwei grundlegend verschiedene Prozesse bei. Zum einen führt das Anlegen des Feldes zu Fluktuationen der Zustandsdichte, welche ihrerseits die Strom-Strom Korrelationsfunktion beeinflussen. Zum anderen trägt ein photovoltaischer Effekt, welcher durch die lokale Symmetriebrechung aufgrund der zufälligen Verteilung der Störstellen in den Ringen bedingt ist, zum Strom bei. Es ergibt sich, dass der erste Effekt um mehrere Größenordnungen größer als der zweite ist. Außerdem ist es möglich Feldamplituden und Frequenzen innerhalb der Grenzen der Störungtheorie zu wählen, bei welchen der mikrowellenfeldinduzierte Effekt so gross wie, wenn nicht sogar größer als, der Dauerstrom im Gleichgewicht ist. Abschließend wird festgestellt, dass der berechnete Effekt experimentell messbar ist. Es werden mögliche Messabläufe, welche den berechneten Effekt nachweisen können, vorgestellt und deren Ergebnisse berechnet.

Im zweiten Teil der Arbeit werden Quantenpunkte betrachtet, in welchen die elektronischen Freiheitsgrade stark an eine Vibrationsmode gekoppelt sind. Diese Kopplung bedingt eine Verschiebung der Elemente der Tunnelmatrix, welche sich z.B. in Vibrationsseitenbändern im Coulomb blockierten Regime manifestiert, sowie eine Renormierung der Ladungsenergie der Quantenpunkte. Es wird ein Spezialfall betrachtet, in welchem die Ladungsenergie effektiv nicht nur negativ, sondern betragsmäßig sogar größer wird als der Energieverlust, welcher durch den endlichen Energielevelabstand beim Tunneln eines Elektrons auf den Quantenpunkt entsteht. In diesem Fall weist das System eine Instabilität

auf, welche durch das Hinzufügen eines anharmonischen vibronischen Terms regularisiert wird.

Es ergibt sich, dass das effektive Potential des Systems grundlegende Unterschiede zum bekannten Fall positiver Ladungsenergie aufweist. Dies ändert die Eigenschaften im Coulomb blockierten Regime bei niedrigen Temperaturen. Zum Beispiel zeigen sich große Änderungsraten der durchschnittlichen Elektronenzahl sowie deren Fluktuationen bei geringer Gatespannung. Schließlich wird die Möglichkeit der experimentellen Realisierung des Systems in Kohlenstoffnanoröhren, welche starke Elektron-Vibrations Kopplungen aufweisen, diskutiert.

Publications

- *Electromechanical instability in vibrating quantum dots with effectively negative charging energy.*
  Phys. Rev. B **80**, 195103 (2009).
  T. Ojanen, F. C. Gethmann and F. von Oppen.

Selbstständigkeitserklärung

Hiermit versichere ich, dass ich alle verwendeten Hilfsmittel und Hilfen angegeben und die vorliegende Arbeit auf dieser Grundlage selbstständig verfasst habe. Diese Arbeit ist nicht schon einmal in einem früheren Promotionsverfahren eingereicht worden.

Friedrich Carl Gethmann